ScienceJet

EMCMRE-1
Marrakech-Morocco
November 21-25 2011

ISSN 2278 - 3393

Proceedings of

First Euro-Mediterranean Conference on Materials and Renewable Energies (EMCMRE-1)

"From Nanoscience to Renewable Energies and to Biology"

Co-Editors of the proceedings:

Prof. Hamid Oughaddou (University of Cergy-Pontoise and ISMO-CNRS)
Prof. Abdelkader Kara (University of Central Florida)

Cognizure

www.cognizure.com/sj

ScienceJet

ISSN 2278 - 3393

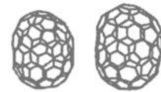

EMCMRE-1

Marrakech-Morocco

November 21-25 2011

A special issue of selected articles presented in
First Euro-Mediterranean Conference on Materials and Renewable Energies (EMCMRE-1)

Co-Editors of the proceedings

Prof. Hamid Oughaddou (University of Cergy-Pontoise and ISMO-CNRS)
Prof. Abdelkader Kara (University of Central Florida)

Cognizure

Table of Contents

Article ID	Article
1	**A competitive diffusion of titanium and palladium atoms in Ti/Pd/Si and Pd/Ti/Si annealed ternary systems** A. H. Hammoudi, C. Benazzouz, C. A. Pineda-Vargas, M. Nkosi (5 Pages)
2	**Theoretical investigations of structural and thermal properties of PbS and PbSe** M. Labidi, S. Labidi, F. El Haj Hassan (4 Pages)
3	**First principles calculations of the structural and thermal properties of $Pb_{1-x}Sr_xS$ ternary alloys** S. Labidi, M. Labidi, F. El Haj Hassan (5 Pages)
4	**Formation of deuterium molecules in the cold interstellar medium: An experimental view** Lisseth Gavilan, Jean Louis Lemaire, Gianfranco Vidali (3 Pages)
5	**Optimization of the parameters of elaboration of the quaternary chalcopyrite $CuInGaSe_2$ for photovoltaic applications** M. Mezghache, O. Benhalima, F. Chouia, B. Hadjoudja, B. Chouial, A. Chibani (3 Pages)
6	**Optimisation of p-type a-SiC:H for p-i-n solar cells** J. D. Santos, N. González, J. Cárabe, J. J. Gandía (6 Pages)
7	**Visible evidence for the formation of copper complexes in garlic extracts treated with copper sulfate and sodium nitrite mixture** Nicholas Sarpong Sarfo, Ibok Nsa Oduro, Kwabena Justice Sarfo (6 Pages)
8	**Compact charge model for ultra-thin nanoscale Double Gate MOSFETs** M. A. Abdi, F. Djeffal, T. Bendib, M. Chahdi , A. Benhaya (4 Pages)
9	**Femtosecond study of the interaction of intense femtosecond laser pulse with Kr clusters using Landau damping** N. Boucerredj, K. Beggas, A. Brichni (4 Pages)
10	**Mössbauer studies of the nanostructured Fe (Si, Cr) alloys** B. Bouzabata, Z. Bensebaa, A. Djekoun, J. M. Grenèche (4 Pages)

Article ID	Article
11	**Low-RF-power deposition of p-type microcrystalline silicon emitters** A. Casado, I. Torres, J. D. Santos, R. Barrio, J. J. Gandía, J. Cárabe, G. Bianco, M. Losurdo, G. Bruno (5 Pages)
12	**Effect of dual treatment based on porous silicon and sputter-deposited TiO_2 doped Cr film on the optoelectronic properties of monocrystalline Si** A. Hajjaji, M. Ben Rabha, N. Janene, W. Dimassi, B. Bessais, M. A. El Khakani, M. Gaidi (4 Pages)
13	**Effect of double treatment based on porous Si and TiO_2 passivation on the optoelectronic properties of multicrystalline silicon substrates** N. Janene, A. Hajjaji, M. Ben Rabha, B. Bessais, M. A. El Khakani, M. Gaidi (4 Pages)
14	**An alternative explanation for the effect of Ge content on the density of end-of-range defects found in ion implanted relaxed SiGe alloys** A. Belafhaili, L. Laânab, P. F. Fazzini, F. Cristiano, N. Cherkashin, G. Benassayag, A. Claverie (5 Pages)
15	**Electronic and optical properties of Cu_2XS_3 (X=Si, Ge, Sn): Prospects for photovoltaics** V. L. Shaposhnikov, A. V. Krivosheeva, V. E. Borisenko, J.-L. Lazzari (5 Pages)
16	**Structure, electronic and optical properties of tin sulfide** V. L. Shaposhnikov, A. V. Krivosheeva, V. E. Borisenko, J.-L. Lazzari (4 Pages)
21	**Influence of the CF_4+O_2 plasma treatment of ZnO:Al on a-Si p-i-n solar cell performance** J. D. Santos, S. Fernández, A. Casado, J. L. Baldonedo, O. De Abril, C. Maffiotte, J. Cárabe, J. J. Gandía (6 Pages)

A competitive diffusion of titanium and palladium atoms in Ti/Pd/Si and Pd/Ti/Si annealed ternary systems

A. H. Hammoudi[a,*], C. Benazzouz[a], C. A. Pineda-Vargas[b], M. Nkosi[b]

[a] Centre de Recherche Nucleaire d_Alger, CRNA, 2 Bd Frantz Fanon, 16000 Algiers, Algeria
[b] Materials Research Departement, iThemba LABS, P. O. Box 722, Somerset West, 7129, Cape town, South Africa

*Author for correspondence: A. H. Hammoudi, email: hammoudi.hakim@yahoo.fr
Received 4 Feb 2012; Accepted 27 Mar 2012; Available Online 19 Apr 2012

Abstract

Multilayered pure titanium and palladium films were evaporated alternatively on (1 0 0) monocristalline silicon substrates. Annealing, in a furnace vacuum, was carried out at temperatures ranging from 700 up to 950°C, for 30 min. The obtained samples were analyzed by means of Rutherford backscattering spectrometry, X-ray diffraction and scanning electron microscopy techniques. The interdiffusion of the different elements all with the enhanced transformations occurring at Pd/Ti and Ti/Si interfaces has been investigated.

Keywords: Titanium; Palladium; Silicon; Silicides; Morphology; Backscattering spectrometry; Scanning electron microscopy; X-ray diffraction

1. Introduction

Interconnection paths that possess low resistivity and the ability to withstand subsequent high temperature processes are critical to VLSI manufacturing [1,2]. The resistivity of Al is low enough for VLSI interconnection purposes, but its low melting and eutectic temperatures restrict subsequent processes to operating temperatures of less than 500° C. Therefore, such low-resistivity interconnections are usually fabricated using materials known as refractory metal silicides (MSix), which can handle much higher processing temperatures than Al. In addition, the high diffusivity of silicon through silicide layers can be a problem in silicon-silicide-metal systems since, with heat treatment, these can exhibit excessive interdiffusion between the metal and the silicon through the silicide layer [3]. This silicon-metal interdiffusion can result in loss of system integrity. Barrier layers are therefore used in preventing this interdiffusion problem, by interposing a film between the silicide layer (which is formed over the silicon substrate as an interconnection path or contact) and the metallization layer [4].

We report here, the results of the behavior of silicon and titanium diffusion in presence of palladium atoms as well as silicon and palladium diffusion in presence of titanium atoms, by interchanging the sequence of metal layers deposition [1,5]. It is very interesting to study the Ti/Pd/Si(100) system in comparison to the Pd/Ti/Si(100) systems in order to see the influence of the diffusion mechanisms on the interfacial reaction between Ti and Si as well as between Pd and Si. In the same way, the effect of palladium layer on the titanium silicides growth and formation is investigated as well as the effect of titanium layer on the palladium silicides growth and formation.

2. Experimental

Prior to loading in the vacuum chamber, the (100) monocristalline Si wafers are degreased in acetone, trichloethylene and methanol baths, and then etched in a diluted hydrofluoric acid solution to remove any native silicon oxide. Titanium and palladium 500 Å thick were alternatively and consecutively deposited by electron gun evaporation, without breaking the vacuum ($2*10^{-7}$ Torr). The obtained Ti/Pd/Si(100) and Pd/Ti/Si(100) samples are annealed in a vacuum furnace in a temperature range 700–950 °C during one time of 30 min (isochronal annealing) [6]. Furthermore, quantitative and qualitative analysis of samples was realized by mean of Rutherford backscattering spectrometry (2 MeV, $4He^{+}$), electronic microscopy and X-ray diffraction (Cu, Kα). The composition and thickness of formed layers were determined by the fitting the experimental RBS spectra with the help of those simulated from the RUMP program [7]. The morphology of the samples surface was examined by scanning electron microscopy (SEM) and their surface composition was given by means of an X-ray dispersive energy analyzer (EDAX) integrated into the electron microscope [8]. It allows local punctual analysis on the crystallites or global analysis on larger areas when the layer is continuous. The primary energy of the electron beam is chosen equal to 9 keV, in order to limit the excessive Si atoms bulk contribution. The XRD in the θ–2θ mode is used to identify the formed compounds.

3. Results and Discussion

3.1. RBS measurements

As it's well known, RBS technique allows the determination of the elemental constitution and their depth distribution within the target [5]. The obtained RBS spectra for both the considered specimens (Ti/Pd/Si(100) & Pd/Ti/Si(100)) are given separately, each on its proper diagram (Figure 1) to show better the enhanced

© Cognizure. All rights reserved.

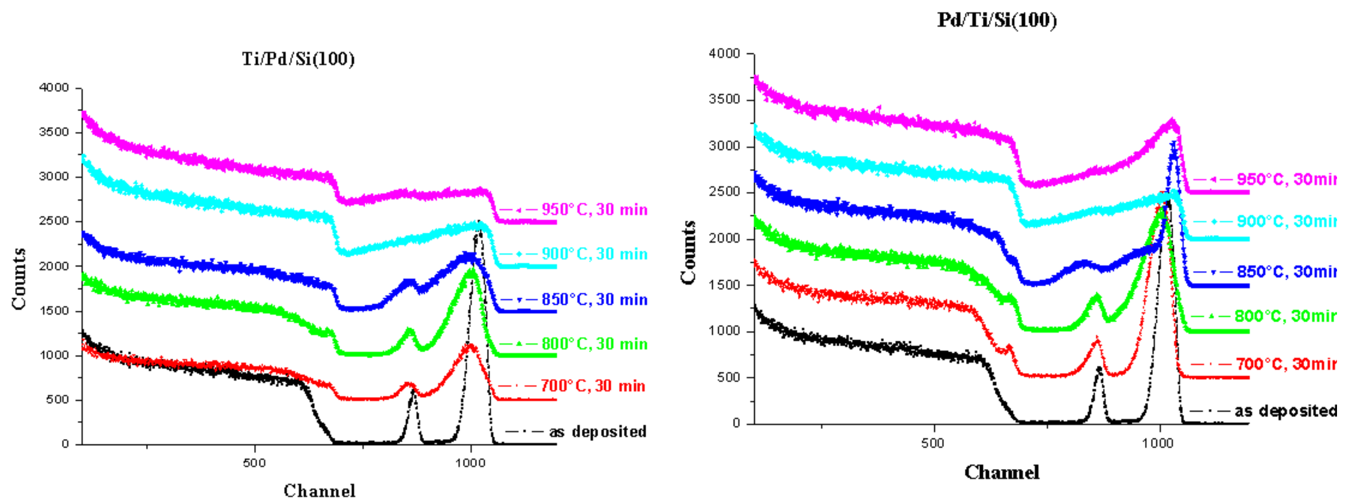

Figure 1. Superposed RBS experimental spectra as function of the annealing temperature (on the left for the ternary system Ti/Pd/Si(100), on the right for the ternary system Pd/Ti/Si(100)).

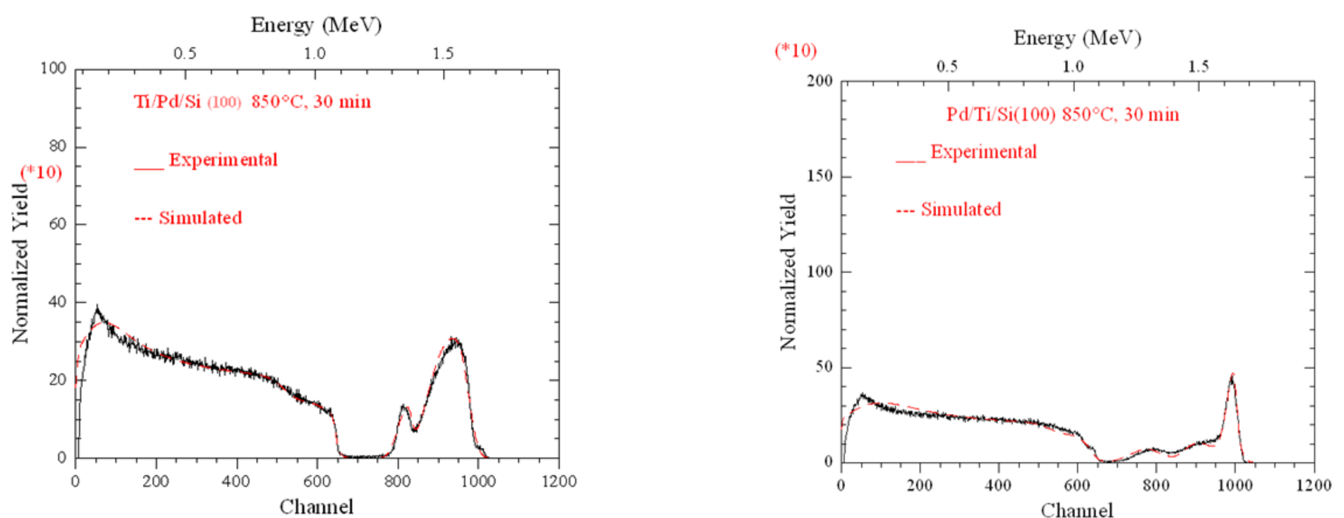

Figure 2. The superposed simulated over experimental spectrum (on the left for the ternary system Ti/Pd/Si(100), on the right for the ternary system Pd/Ti/Si(100)). The annealing temperature is 850°C.

transformations and interdiffusions, as function of the annealing temperature.

The following observations could easily be established:

For the un-annealed sample for both the considered systems, the characteristic peaks are well separated. However, as the annealing starts at only 700°C, the characteristic peaks of both metals extend at the interfaces toward lower energies, accompanied by a small proportion of Si atoms diffusion toward higher energies. This double diffusion in opposite directions could suggest beginning of new compounds formation at the interfaces. At higher temperatures (i.e. 800°C up to 850°C) the interdiffusion becomes more noticeable, which suggests a multiplication of new compounds formation at the interfaces or/and the previously-formed compounds become more and more thick. Ultimately, the characteristic peaks trend to an overlapping to reach at the end a nearly, complete fusion, which can assume a total consumption of the metals within the Si bulk [9,10].

It should be underlined that the interdiffusion seems to be more pronounced for the system Ti/Pd/Si(100) due to the diffusion barrier layer, which is assumed to become porous as the annealing temperature increases, in contrast to the second system where the diffusion barrier layer is formed by a refractory metal.

The experimental RBS spectra were simulated by the RUMP software (Figure 2) and some obtained results are summarized in the Table 1. The major remarks that come out are listed below:

- For the un-annealed specimens, the primary interdiffusion is more pronounced for the Pd/Ti system, probably due to the relatively high heat transfer during refractory metal deposition, in the first step. However, for the Ti/Pd system a somewhat thick silicone oxide is formed between Ti layer and Pd layer, probably due to the great ability of the Ti superficial layer to capture oxygen.

© Cognizure. All rights reserved.

Table 1. Summary of the simulation results.

Annealing temperature (°C)	Pd/Ti/Si(100)		Ti/Pd/Si(100)	
	Sub layer thickness (Å)	Sub layer Composition (%)	Sub layer thickness (Å)	Sub layer Composition (%)
As-deposited	140	Pd(73)+Si(27)	310	Ti(92)+Si(8)
	220	Pd(66)+Ti(12)+Si(22)	200	Si(35)+O(65)
	40	Pd(95)+Ti(5)	410	Pd(92)+Si(8)
	80	Ti(23)+Si(78)	30000	Si(100)
	30000	Si(100)		
850	50	Pd(66)+Ti(34)	1000	Ti(33)+Si(67)
	50	Pd(63)+Si(37)		
	250	Pd(65)+Si(35)	2650	Pd(18)+Si(82)
	1800	Ti(20)+Si(80)		
	380	Pd(35)+Ti(20)+Si(45)	30000	Si(100)
	30000	Si(100)		
900	1500	Ti(8.5)+Ti(6)+Si(85.5)	1700	Ti(8.5)+Ti(8.5)+Si(83)
	500	Ti(15)+Si(85)	550	Pd(20)+Si(80)
	500	Pd(15)+Si(85)	500	Ti(10)+Si(90)
	1000	Ti(20)+Si(80)	1000	Ti(20)+Si(80)
	350	Pd(35)+Si(65)	350	Pd(35)+Si(65)
	14100	Pd(1.5)+Ti(1.5)+Si(97)	13000	Ti(01)+Pd(01)+Si(98)
	30000	Si(100)	30000	Si(100)

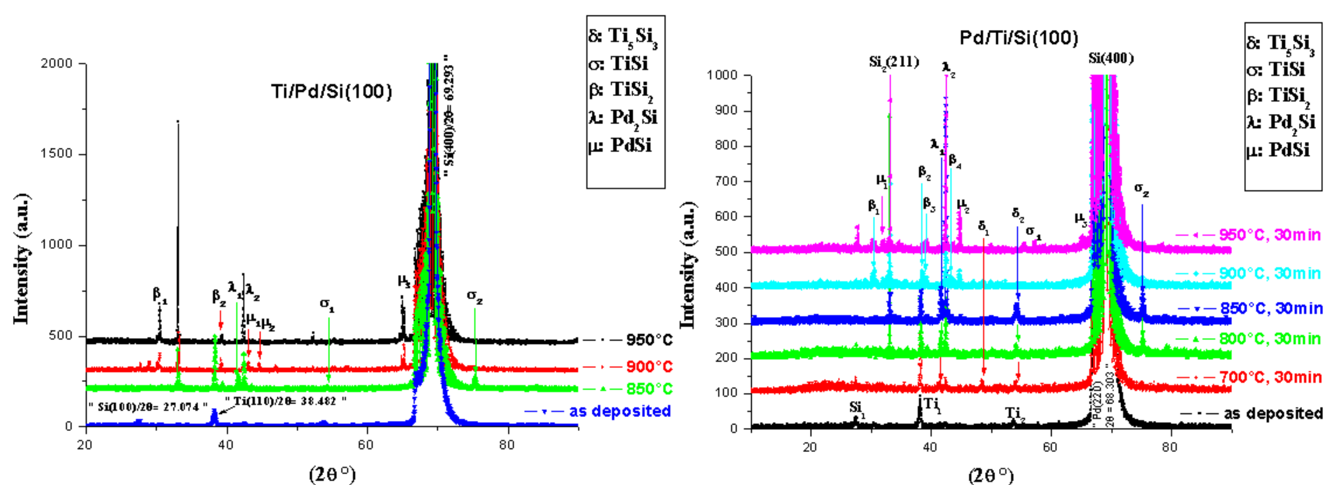

Figure 3. Superposed XRD experimental diffractograms as function of the annealing temperature (on the left for the ternary system Ti/Pd/Si(100), on the right for the ternary system Pd/Ti/Si(100)).

- Obviously, as the annealing temperature is raised new compounds are formed. For the Pd/Ti system, it was found out that the sample's composition (for the different compounds stochiometry as well as their thicknesses) strictly, depends upon the annealing temperature, probably because of the non-uniform repartition of the heat through the different thin films and the substrate which means that the superficial Pd layer is overheated and the Si substrate is under heated, due to the refractory metal barrier layer [11,12]. However, for the Ti/Pd system, it was found out that the sample's constitution remains the same independent of the annealing temperature; only the thickness of the formed compounds increased, roughly linearly.

3.2. XRD measurements

The obtained data are plotted as diffractograms, for easiness all the diffractograms are summarized on the same diagram as function of the annealing temperature (Figure 3) and the detailed data are summarized in Table 2.

The retained main observations are given herein:

The diffractograms of the un-annealed samples for both systems show the characteristic peaks of the sample's constituents. It should be mentioned that the palladium peak could not be distinguished because at that stage, it's totally enclosed within the silicon signal as the last is highly intense and relatively broad. At the beginning of annealing, it has been found out for both systems that some rich titanium-metal silicides start appearing. By increasing the annealing temperature the formerly obtained phases gradually convert to mono-silicide accompanied with the apparition of rich-palladium metal silicides. Furthermore, in the final stage of the annealing the mono titanium metal silicides convert to

© Cognizure. All rights reserved.

Table 2. XRD data.

Annealing temperature (°C)	Pd/Ti/Si(100) (2θ °)	Peak/phase	Ti/Pd/Si(100) (2θ °)	Peak/phase
As deposited	27.074	Si(100)	27.074	Si(100)
	38.482	Ti(110)	33.016	Si(220)
	53.008	Ti(102)	38.482	Ti(110)
	69.293	Si(400)	41.778	Si(210)
	68.585	Pd(220) Not visible, as yet	69.293	Si(400)
700	48.784	Ti_5Si_3(220)	41.783	Pd_2Si(201)
	54.144	Ti_5Si_3(311)	51.035	Ti_5Si_3(310)
	68.585	Pd(220) Not visible, as yet	54.298	Ti_5Si_3(311)
800	33.425	TiSi(111)	33.018	Si(211)
	38.556	TiSi(102)	41.783	Pd_2Si(201)
	41.240	TiSi(211)	40.119	Pd(111)
			42.609	Pd_2Si(210)
	42.609	Pd_2Si(210)	75.818	TiSi(015)
	41.240	TiSi(211)	42.609	Pd_2Si(210)
	42.609	Pd_2Si(210)	54.005	TiSi(210)
	54.144	Ti_5Si_3(311)	75.818	TiSi(015)
	68.585	Pd(220) Now visible		
	75.278	TiSi(004)		
900	30.155	$TiSi_2$(202)	30.155	$TiSi_2$(202)
	33.646	TiSi(111)	39.275	$TiSi_2$(311)
	38.429	$TiSi_2$(113)	42.609	Pd_2Si(210)
	39.275	$TiSi_2$(311)	43.662	PdSi(202)
	42.609	Pd_2Si(210)	44.426	PdSi(211)
	43.424	$TiSi_2$(022)		
	44.426	PdSi(211)		

silicides of lower metal content, in parallel, the previous rich palladium metal silicides convert to mono-silicide, which is in good agreement with the predictions in such a metallurgical reaction, as metal-rich silicides generally form first, and continue to grow until all the metal is consumed. When the metal has been consumed, silicides of lower metal content start appearing, which can continue to grow simply by consuming the metal-rich silicides [13-15]. To illustrate this with Ti as the metal, studies conducted by experts show that TiSi would be the first silicide to form on Si, typically appearing at a temperature above 500°C and peaking at 700°C. $TiSi_2$ only starts to appear at 600°C and peaks at 800°C. Beyond 800 °C, TiSi would be fully converted into $TiSi_2$, at which point the system attains stability [3,5,16].

In general, one can easily notice that firstly, the titanium silicides are obtained, followed by the formation of palladium silicides. That is independent of the bi-layered system sequence, which could assume that the titanium atoms could be the dominant moving specie.

3.3. SEM observations

The surface morphology was examined by a scanning electron microscopy and the recorded micrographs show the surface morphology evolution as function of the annealing temperature (Figure 4). By referring to these micrographs, we can remark continuity and uniformity in the surface morphology evolution process. In fact, the surface morphology of the un-annealed sample is a flat and homogeneous surface. As the annealing begins at 700°C, we can observe a high density of randomly dispatched very small crystallites, at higher annealing temperatures (800-850°C) greater crystallites form probably by assembly from the former, smaller ones, with lower density. At the final stage of the annealing we have a perfect elliptically shaped motivates of few µm² in dimension. Each of the obtained motivates is constituted by a dark nuclei, shielded by a surrounding clear wall. To determine their respective composition we performed EDAX via punctual analysis, and we can state that the central region is filled with low metal content of titanium-silicide compound meanwhile, the outer region is occupied with rich palladium-silicon compound, that is independent of the bi-layered sequence [8]. Therefore, we can assume that, in the first step, titanium silicides has formed in the centre then, the palladium silicide, occupying the surrounding region forms the last, which is in good agreement with the results of the previous paragraph.

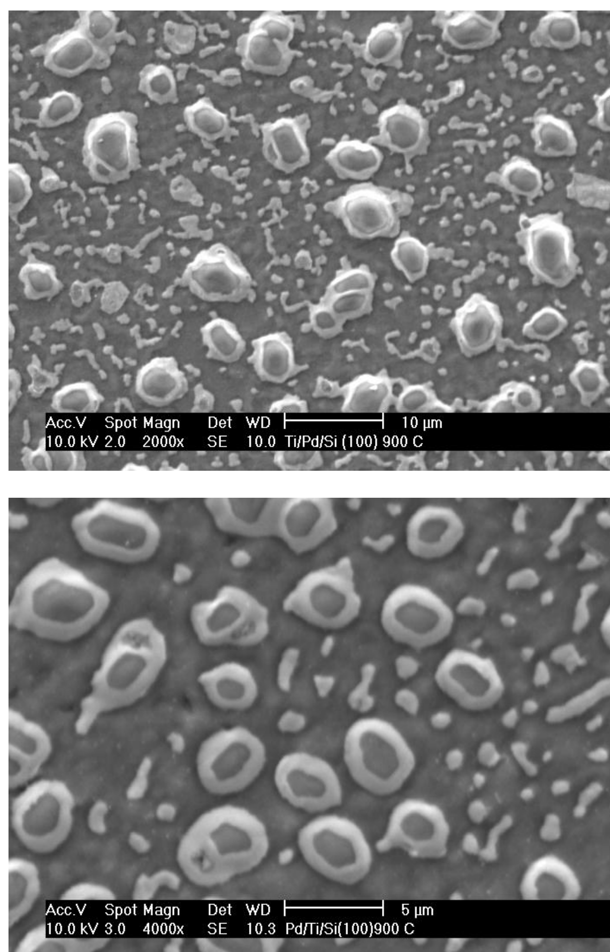

Figure 4. SEM micrographs showing the surface morphology for the annealed specimens at 900°C (on the left Ti/Pd/Si(100), on the right for Pd/Ti/Si(100)).

© Cognizure. All rights reserved.

4. Conclusions

A study on the competitive diffusion of bilayers Ti/Pd and Pd/Ti on (100) monocristalline silicon was carried out as function of the annealing temperature. The occurred interdiffusion was evidenced and investigated by mean of the powerful analysis techniques. The most meaningful concluded results could be summarized as follows:

- The interdiffusion seems to be more pronounced for the system Ti/Pd/Si(100).
- Titanium silicides are firstly obtained, followed by the formation of palladium silicides.
- Titanium silicide has formed in the centre then the palladium silicide occupying the surrounding region on the sites of phases.
- The collected data from all the used analysis techniques are in good agreement.
- The use of a diffusion barrier considerably delays the on-surface diffusion before reaching the ultimate stable phases formation.
- Determination of the dominant moving specie.
- Improvement of the thermal stability.
- Prevention of the titanium silicides from oxidation.

References

1. M.A. Nicolet, S.S. Lau, VLSI Electronics Microstructure Science, In: J. Einspruch, G.B. Larrabee (Eds.), Materials and Process Characterization, Academic Press, Vol. 6 (1983).
2. S.P. Murarka, Silicides for VLSI Applications, Academic Press, London (1983).
3. J.O. Mc Caldin, H. Sankur, Appl. Phys. Lett. 20 (1972) 171.
4. A.Hammoudi, C.Benazzouz, S.Tobbeche, N.Benouattas and N.Boukhalfa, Mater. Sci. Forum (2009) 161.
5. S.S. Lau, W.F. Van Der Weg, In: J.M. Poate, K.N. Tu, J.W. Mayer (Eds.), Thin Films Interdiffusion and Reactions (Chapter 12), Princeton, New Jersy (1978).
6. C. Benazzouz, N. Benouattas, A. Bouabellou, Nucl. Instrum. Meth. B. 213 (2004) 519.
7. R.L. Doolittle, Nucl. Instrum. Meth. B. 15 (1996) 227.
8. A.H.Hammoudi, A.H.Benyagoub, C. Benazzouz, C.A. Pineda-Vargas and M. Nkosi, Adv. Mater. Res. 324 (2011) 306.
9. C.-A. Chang, H.L. Yeh, Appl. Phys. Lett. 49 (1986) 1233.
10. L. Soltz, F.M. D_Heurle, Thin Solid Films 189 (1990) 269.
11. Risa Suryana, Osamu Nakatsuka, and Shigeaki Zaima, Jpn J. Appl. Phys. 49 (2010) 05FA09.
12. Risa Suryana, Osamu Nakatsuka, and Shigeaki Zaima, Jpn J. Appl. Phys. 50 (2011) 05EA09.
13. S.-Q. Wang, Mater. Res. Soc. Bull. XIX (1994) 30.
14. C.-A. Chang, J. Vac. Sci. Technol. A. 9 (1991) 98.
15. A.S. Bereshnai, In: Silicon and its binary systems, Library of congress catalogue card no. 60, New York (1960) p. 53.
16. H. Okamoto, T.B. Massalski, In: V. Raghavan (Ed.), Phase Diagrams of Ternary Iron Alloys, Indian Institute of Materials, Calcutta (1992) p. 429.

Cite this article as:

A. H. Hammoudi *et al.*: **A competitive diffusion of titanium and palladium atoms in Ti/Pd/Si and Pd/Ti/Si annealed ternary systems.** ScienceJet 2012, **1**: 1

© Cognizure. All rights reserved.

Theoretical investigations of structural and thermal properties of PbS and PbSe

M. Labidi[a,*], S. Labidi[a], F. El Haj Hassan[b]

[a] *Département de Physique, Faculté des Sciences, Université de Annaba, Algeria*
[b] *Université Libanaise, Faculté des Sciences (1), Laboratoire de Physique des Matériaux, Elhadath, Beirut, Lebanon*

[*] *Author for correspondence: M. Labidi, email: labidimalika4@yahoo.fr*
Received 4 Feb 2012; Accepted 27 Mar 2012; Available Online 19 Apr 2012

Abstract

First-principles calculations are performed to investigate the structural, elastic and thermal properties of PbS and PbSe in rocksalt structure using the full-potential linearized augmented plane wave method. In this approach, the generalized gradient approximation (GGA) of Perdew et al. was used for exchange correlation potentials. Results for lattice constant, bulk modulus and elastic constants are in agreement with experimental and theoretical data. The quasi-harmonic Debye model, using a set of total energy versus volume calculations obtained with the FP-LAPW method, is applied to study the thermal properties. Temperature effects on the structural parameters, thermal expansions, heat capacities and Debye temperatures are determined from the non-equilibrium Gibbs functions.

Keywords: DFT; FP-LAPW; GGA; Debye temperatures

1. Introduction

The lead salts semiconductors PbS, PbSe and PbTe have been subject of many experimental and theoretical works. They have been largely used in infrared detectors, as infrared lasers in fiber optics, as thermoelectric materials, in solar energy panels, and in window coatings [1, 2]. One of their interesting properties is their narrow fundamental energy band gap [3,4]; that is why, these IV–VI semiconductors are useful in optoelectronic devices such as lasers and detectors [5–7]. They are used in medical diagnostic and atmospheric pollution control [8]. The small energy gap of lead chalcogenides semiconductors is one of the most important properties leading to the experimental interest in these materials. Experimental researches have been performed on their structural and band properties [9, 10], electronic structure [11,12], and optical properties [13, 14]. Many theoretical studies of electronic structures of these semiconductors are carried out using different methods of calculations. We can cite: the FP-LMTO method [15], FP-LAPW method [16–18], pseudopotential method [19, 20] and orthogonalized-plane-wave method [21]. All of the theoretical calculations founded a direct band gap at the L point of the Brillouin zone for all three compounds. These materials crystallize in the rocksalt structure at ambient temperature and pressure.

This article gives a systematic theoretical analysis of the structural, elastic and thermodynamic properties of PbS and PbSe compounds by using the full-potential-linearized-augmented plane wave (FP-LAPW) method in the framework of density functional theory (DFT), with the generalized gradient approximation (GGA).

The rest of the paper has been divided into three parts. In Section 2, we briefly describe the computational techniques used in this study. The most relevant results obtained for the structural, elastic and thermodynamic properties of PbS and PbSe compounds are presented and discussed in Section 3. Finally, in Section 4 we summarize the main conclusions of our work.

2. Calculation method

The calculations were performed using the full potential linear augmented plane wave (FP-LAPW) method [22] within the frame-work of the density functional theory (DFT) [23, 24] as implemented in the Wien2k code [25]. For the exchange-correlation potentials, we have used the generalized gradient approximation (GGA) [26].

The self-consistent calculations are considered to be converged only when the calculated total energy of the crystal converged to less than 1 mRyd. In the FP-LAPW method, the wave function and potential are expanded in spherical harmonic functions inside non-overlapping spheres surrounding the atomic sites (muffin-tin spheres) and a plane wave basis set in the remaining space of the unit cell (interstitial region) is used. The muffin-tin radius R_{MT} were assumed to be 2.5, 2.1 and 2.3 a.u. for Pb, S and Se, respectively. The maximum l value for the wave functions expansion inside spheres was confined to $l_{max} = 10$. The plane wave cut off of $K_{max} = 8.0/R_{MT}$ (R_{MT} is the smallest muffin-tin radius) is chosen for the expansion of the wave functions in the interstitial region while the charge density was Fourier expanded up to $G_{MAX} = 14$. The k integration Meshes of 45 special k-points were chosen in the irreducible wedge of the Brillouin zone for the compound. All these values have been chosen in a way to ensure the convergence of the results.

3. Results and Discussion

3.1. Structural properties

In order to calculate the ground state properties of PbS and PbSe, the total energies are calculated in rocksalt structure. The calculated total energies are fitted to the Murnaghan's equation of state [27] to determine the ground state properties such as the equilibrium lattice constant a and the bulk modulus B. The calculated equilibrium parameters (a and B) in NaCl structure are given in Table 1 which also contains results of the previous first principle calculations as

© Cognizure. All rights reserved.

Table 1. Structural and elastic parameters of PbS and PbSe. The calculated results GGA are compared with the experimental data. The bulk modulus B and elastic constant C_{ij} are in the unit of GPa. Note that the DFT results correspond to T = 0 K.

	Lattice constant a (Å)	Bulk modulus B(GPa)	Elastic constant parameters		
			C_{11}	C_{12}	C_{44}
PbS					
This work	6.011	51.9	130.81	22.21	20.60
Experiment	5.940[a]	52.9[a]	124.0[c]	33.0[c]	23.0[c]
Other calculations	6.012[b]	52.1[b]	135.1[d]	16.9[d]	20.4[d]
PbSe					
This work	6.224	47.8	122.16	10.31	17.91
Experiment	6.130[c]	54.1[c]	123.7[c]	19.3[c]	15.9[c]
Other calculations	6.222[b]	47.5[b]	123.6[d]	12.2[d]	17.6[d]

[a] Ref [28], [b] Ref [29] , [c] Ref [30], [d] Ref [31]

well as the experimental data. Our calculated lattice constants and (bulks) are slightly larger (less) than the experimental works. This is essentially due to the GGA. These results are also in good agreement with previous first-principles calculations [29].

We also calculate the elastic constants (C_{11}, C_{12} and C_{44}) for the two compounds using a numerical first-principles method. Results of elastic constants are presented in Table 1. The traditional mechanical stability conditions on the elastic constants in cubic crystals are known to be $C_{11} - C_{12} > 0$, $C_{11} + 2C_{12} > 0$, $C_{11} > 0$ and $C_{44} > 0$. Our results for elastic constants in Table 1 obey these stability conditions. Our values are relatively close to those of Ref. [31].

3.2. Thermal effects: Quasi-harmonic Debye model

To investigate the thermodynamic properties of PbS and PbSe compounds under high temperature, we apply the quasi-harmonic Debye model [32], in which the non-equilibrium Gibbs function *G*(V; P, T)* can be written in the form of

$$G^*(V;P,T) = E(V) + P(V) + A_{vib}[\theta(V);T] \tag{1}$$

where *E(V)* is the total energy per unit cell, *PV* corresponds to the constant hydrostatic pressure condition, *θ(V)* is the Debye temperature, and A_{Vib} is the vibrational term, which can be written using the Debye model of the phonon density of states as [33, 34]

$$A_{vib}(\theta,T) = nkT\left[\frac{9\theta}{8T} + 3\ln\left(1 - e^{-\theta/T}\right) - D\left(\frac{\theta}{T}\right)\right] \tag{2}$$

where n is the number of atoms per formula unit, $D(\theta/T)$ represents the Debye integral, and for an isotropic solid, θ is expressed as [33]

$$\theta_D = \frac{\hbar}{k}\left[6\pi^2 V^{1/2} n\right]^{1/3} f\left(\sigma\sqrt{\frac{B_S}{M}}\right) \tag{3}$$

M being the molecular mass per unit cell and B_S the adiabatic bulk modulus, approximated by the static compressibility [32]

$$B_S \cong B(V) = V\frac{d^2E(V)}{dV^2} \tag{4}$$

$f(\sigma)$ is given by Refs [35, 36]; the Poisson σ is taken as 0.25 [37].

Therefore, the non-equilibrium Gibbs function *G*(V; P, T)* as a function of *(V; P, T)* can be minimized with respect to volume *V*.

$$\left[\frac{\partial G^*(V,P,T)}{\partial V}\right]_{P,T} \tag{5}$$

By solving Eq. (5), one can obtain the thermal equation of state (EOS) *V (P, T)*. The heat capacity C_V and the thermal expansion coefficient α are given by [35]

$$C_V = 3nk\left[4D\left(\frac{\theta}{T}\right) - \frac{3\theta/T}{e^{\theta/T} - 1}\right] \tag{6}$$

$$S = nk\left[4D\left(\frac{\theta}{T}\right) - 3\ln\left(1 - e^{-\vartheta/T}\right)\right] \tag{7}$$

$$\alpha = \frac{\gamma C_V}{B_T V} \tag{8}$$

Where γ is the Grüneisen parameter, which is defined as

$$\gamma = -\frac{d\ \ln\ \theta(V)}{d\ \ln\ V} \tag{9}$$

Through the quasi-harmonic Debye model, one could calculate the thermodynamic quantities of any temperatures and pressures of compounds from the calculated *E-V* data at *T* = 0 and *P* = 0.

The temperature effects on the lattice constant and bulk modulus are illustrated in Figure 1(a) and (b), respectively. The lattice constant for the two compounds rises with increasing temperature but the rate of increase is greately reduced for PbSe. The bulk modulus of both compounds decreases with temperature. One can notice that from 150 K the bulk modulus for PbSe becomes higher than for PbS. This explains why PbSe is a hard material at high temperature when compared to PbS.

The variations of the thermal expansion coefficient $\alpha(T)$ as a function of the temperature are plotted in Figure 2(a). However, at low temperatures the thermal expansion coefficient increases for the two materials but for the high temperature shows a parabolic behavior for PbS and gradually tends to a linear increase at higher temperatures for PbSe. Figure 2(b) illustrates the heat capacity $C_V(T)$ as a function of temperatures. It is found that when T_o 300 K, the heat

© Cognizure. All rights reserved.

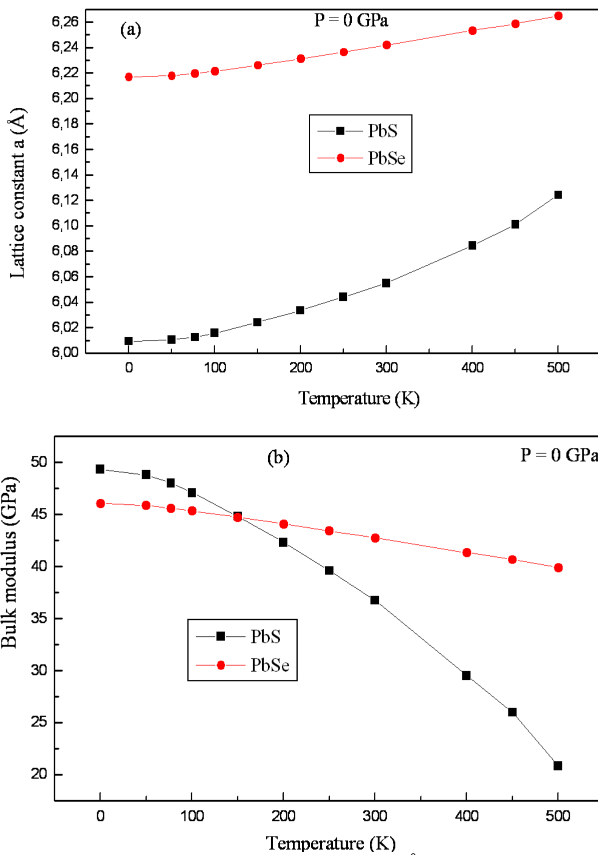

Figure 1. Variation of (a) lattice constant a (Å) and (b) bulk modulus B (GPa) with temperature for PbS and PbSe at pressure 0 GPa.

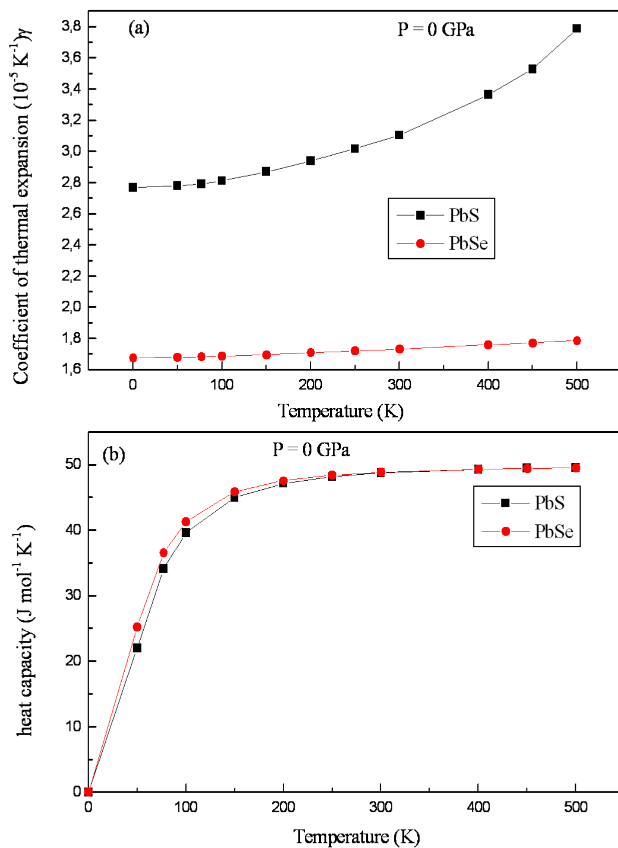

Figure 2. Variation of (a) coefficient of thermal expansion (10^{-5} K^{-1}) and (b) heat capacity (J mol^{-1} K^{-1}) with temperature for PbS and PbSe at pressure 0 GPa.

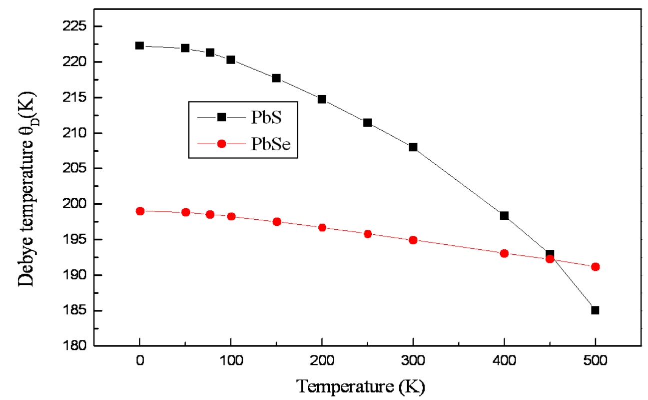

Figure 3. Variation of Debye temperature (K) with temperature for PbS and PbSe at pressure 0 GPa.

capacity $C_V(T)$ is dependent on the temperature T. This is due to the approximations of the Debye model used here. However, the harmonic effect on heat capacity $C_V(T)$ is suppressed at high temperatures, and $C_V(T)$ is close to the Dulong–Petit limit. The specific heat capacity of the two materials at high temperature does not depend much on temperature and tends to approach 50 $Jmol^{-1}$ K^{-1}. At T = 0 K.

Figure 3 displays the dependence of the Debye temperature θ_D on temperature. It can be seen that θ_D is nearly constant from 0 to 100 K and decreases linearly with increasing temperature from T > 100 K for PbSe. Our calculated θ_D at zero pressure and zero temperature is equal to 222.29 K, 199.10 K for PbS and PbSe, respectively.

4. Conclusions

In this study, we have presented a complete theoretical analysis of the structural and thermel properties of PbS and PbSe compounds by using the FP–LAPW method. The use of the GGA for the exchange-correlation potential permitted us to obtain good structural parameters.

The thermal properties of PbS are different from PbSe. The dependency of the lattice constant, bulk modulus, thermal expansion, heat capacities and Debye temperatures on temperature is predicted. We conclude that the heat capacity of the two materials at high temperature is given by the law of Dulong and Petit.

References

1. E.G. See, G.P. Agrawal, N.K. Dutta, Semiconductors Lasers, Van Nostrand Reinhold, New York (1993) 547.
2. K. Nair, M. Ocampo, A. Fernandez, M.T.S. Nair, Sol. Energy Mater. 20 (1990) 235; P.K. Nair, A. Fernandez, M.T.S. Nair, Proc. SPIE Int. Soc. Opt. Eng. 1149 (1989) 88.
3. R. Dalven, H. Ehrenreich, F. Seitz, D. Turnbull (Eds.), Solid State Physics, Academic Press, New York, Vol. 28 (1973) 179.
4. R.A. Cowley, Philos. Mag. 11 (1965) 673; K. Murase, J. Phys. Soc. Jpn. 49 (Suppl.) (1980) 725.
5. G. Springholz, V. Holy, M. Pinczolits, G. Bauer, Science 282 (1998) 734.
6. E. Khoklov (Ed.), Lead Chalcogenides: Physics and Applications, Taylor and Francis, New York (2003).
7. M. Tacke, Infrared Phys. Technol. 36 (1995) 447.
8. Z. Feit, M. Mc Donald, R.J. Woods, V. Archambauld, P. Mak, Appl. Phys. Lett. 66 (1996) 738.

© Cognizure. All rights reserved.

9. G. Nimtz, B. Schlicht, B. Dornhaus, Narrow Gap Semi-Conductors: Springer Tracts in Modern Physics, Springer, New York (1983) and references therein.
10. A. Miller, G. Saunders, Y. Yogurtcu, J. Phys. C 14 (1981) 1569.
11. M.L. Cohen, J.R. Chelikowsky, Electronic Structure and Optical Properties of Semiconductors (2nd ed.), Springer Series in Solids States Sciences, Springer-Verlag, Berlin vol. 75 (1989).
12. V. Hinkel, H. Hoak, C. Mariana, L. Sorba, K. Horn, N.E. Christensen, Phys. Rev. B 40 (1989) 5549.
13. M. Cardona, D.L. Greenaway, Phys. Rev. 133 (1964) 1685.
14. D. Korn, R. Braunstein, Phys. Rev. B 5 (1972) 4837.
15. A. Delin, P. Ravindran, O. Eriksson, J.M.Wills, Int. J. Quantum Chem. 69 (1998) 349.
16. M. Lach-hab, A.D. Papaconstantopoulos, J.M. Mehl, J. Phys. Chem. Solids 63 (2002) 833.
17. E.A. Albanesi, C.M.I. Okoye, C.O. Rodriguez, E.L. Peltzer y Blanca, A.D. Petukhov, Phys. Rev. B 61 (2000) 16589.
18. E.A. Albanesi, E.L. Peltzer y Blanca, A.G. Petukhov, Comput. Mater. Sci. 32 (2005) 85.
19. M. Schl¨uter, G. Martinez, M.L. Cohen, Phys. Rev. B 11 (1975) 3808.
20. G. Martinez, M. Schluter, M.L. Cohen, Phys. Rev. B 11 (1975) 651.
21. F. Herman, R.L. Kortum, I.B. Ortenburger, J.P. Van Dyke, J. Phys. (Paris) 29 (1968) 4–c62.
22. O. K. Andersen, Phys. Rev. B 42 (1975) 3060.
23. P. Hohenberg and W. Kohn , Phys. Rev. B 136 (1964) 864.
24. W. Kohn and L.J. Sham, Phys. Rev. 140 (1965) 1133.
25. P. Blaha, K. Schwarz, G.K.H. Madsen, D. Kvasnicka and J. Luitz, WIEN2k, An Augmented Plane Wave Plus Local Orbitals Program for calculating Crystal Properties, Vienna University of Technology, Vienna, Austria (2001).
26. J. P. Perdew, S. Burke and M. Ernzerhof, Phys. Rev. Lett. 77 (1996) 386.
27. F. D. Murnaghan, Proc. Natl. Acad. Sci. U.S.A. 30 (1944) 5390.
28. A. Delin, P. Ravindran, O. Eriksson, J.M. Wills, Int. J. Quantum Chem. 69 (1998) 349.
29. S. Kacimi, A. Zaoui, B. Abbar, B. Bouhafs, J. Alloys Compd. 462 (2008) 135.
30. O. Madelung, M. Schulz, H. Weiss (Eds.), Numerical Data and Functional Relationships in Science and Technology, Landolt-Bornstei, New Series, Springer, Berlin, Vol. 17 (1983) p. 173.
31. Yi Zhang, Xuezhi Ke, Changfeng Chen, J. Yang, and P. R. C. Kent, Phys. Rev. B 80 (2009) 024304.
32. M.A. Blanco, E. Francisco, V. Luaña, Comput. Phys. Commun. 158 (2004) 57.
33. M.A. Blanco, A. Martín Pendás, E. Francisco, J.M. Recio, R. Franco, J. Mol. Struct. (Theochem) 368 (1996) 245.
34. M. Flórez, J.M. Recio, E. Francisco, M.A. Blanco, A. Martín Pendás, Phys. Rev. B 66 (2002) 144112.
35. E. Francisco, J. M. Recio, J. M., Blanco, M. A., Martín Pendás, A., J. Phys. Chem. 102 (1998) 1595.
36. E. Francisco, M.A. Blanco, G. Sanjurjo, Phys. Rev. B 63 (2001) 094107.
37. J. P. Poirier, Introduction to the Physics of the Earth's Interior, Cambridge University Press, Oxford (2000) p. 39.

Cite this article as:

M. Labidi *et al.*: **Theoretical investigations of structural and thermal properties of PbS and PbSe.** ScienceJet 2012, **1**: 2

© Cognizure. All rights reserved.

First principles calculations of the structural and thermal properties of $Pb_{1-x}Sr_xS$ ternary alloys

S. Labidi[a,*], M. Labidi[a], F. El Haj Hassan[b]

[a] *Département de Physique, Faculté des Sciences, Université de Annaba, Algeria*
[b] *Université Libanaise, Faculté des Sciences (1), Laboratoire de Physique des Matériaux, Elhadath, Beirut, Lebanon*

Author for correspondence: S. Labidi, email: labidisalima@yahoo.fr
Received 4 Feb 2012; Accepted 26 Mar 2012; Available Online 19 Apr 2012

Abstract

We have performed first-principles calculations using full potential linearized augmented plane wave (FP-LAPW) method within density functional theory (DFT) framework to investigate the fundamental properties of the PbS, SrS and their alloys. The ground state properties such as lattice constant, bulk modulus and elastic constants are in good agreement with numerous experimental and theoretical data. The thermal effect on some macroscopic properties was investigated using the quasi-harmonic Debye model. There is a good agreement between our results and the available experimental data for the binary compounds which may be a support for the results of the ternary alloys reported here for the first time.

Keywords: PbS; SrS; FP-LAPW; GGA; Debye temperatures

1. Introduction

PbS and SrS semiconductors have been in focus in experiments [1–8] and theory [9–18] due to their possible applications in electronic and opto-electronic devices. These materials crystallize in the rocksalt structure at ambient temperature and pressure.

$Pb_{1-x}Sr_xS$ is a non-isoelectronic semiconductor alloy with very strong alloy scattering. It can be grown in thin films of good crystalline quality. The alloying of Pb–SrS to make $Pb_{1-x}Sr_xS$ can increase the band gap energy from 0.4 eV for PbS to 4.6 eV for SrS [19]. A mixture of PbS (direct band-gap) and SrS (indirect band-gap) is interesting for the optical properties and can cover the infrared (IR) to the visible spectrum.

This alloy may be an easily described system in which the effects of disorder in semiconductors can be studied. Some initial experimental work has been done on the preparation of this alloy. Holloway *et al.* [19] showed that $Pb_{1-x}Sr_xS$ alloy exists with the rocksalt structure at all values of $0 < x < 1$ by X-ray diffraction. Tamor *et al.* [20] presented experimental results for the electronic structure of $Pb_{1-x}Sr_xS$ in the rocksalt structure. Tamor [21] described results of two types of measurement on $Pb_{1-x}Sr_xS$: 1) sub-gap absorption spectra measured using photothermal deflection spectroscopy (PDS), and 2) transient photoconductivity (TP).

However, Davis [22] calculated the electronic structure of the rocksalt $Pb_{1-x}Sr_xS$ alloy using recursion method. Recently, Labidi *et al.* [23] have calculated the structural, electronic and thermodynamic properties of $Pb_{1-x}Sr_xS$ alloy using the full potential linearized augmented plane wave method (FP-LAPW). Therefore, the purpose of this work is to study the structural, elastic and thermal properties by using the full-potential-linearized-augmented plane wave (FP-LAPW) method in the framework of density functional theory (DFT), with the generalized gradient approximation (GGA). The remaining of the paper is organized as follows. We describe the computational method in Section 2. The numerically obtained results are presented and discussed in Section 3. Section 4 sets out the conclusion.

2. Calculation method

The difficulty with structural theories of alloys arises from the fact that even in the simplest case of binary system with N sites, there are 2N possible atomic configurations whose total energy needs to be structurally relaxed. Describing random alloys by periodic structures will clearly introduce spurious correlations beyond certain distance. Preventing this problem needs large supercell. However, many physical properties of solids are characterized by microscopic length scales and local randomness of alloys, and modifying the large-scale randomness of alloys does not affect them. Recently, Zunger and co-workers [24] implemented this fact to construct ‘‘special quasirandom structures’’ (SQS) approach by the principle of closer production of the perfectly random network for the first few shells around a given site. They argued that this approach, which we have adopted in our calculation, effectively reduces the size of the supercell for studying many properties of random alloys.

The calculations are performed using the scalar relativistic FP-LAPW approach as implemented in WIEN2K [25] code within the framework of density functional theory (DFT) [26, 27]. The exchange-correlation energy of electrons is described in the generalized gradient approximation (GGA) [28] to calculate the total energy. In the FP-LAPW method, the wave function, charge density and potential are expanded by spherical harmonic functions inside non-overlapping spheres surrounding the atomic sites (muffin-tin spheres) and by a plane waves basis set in the remaining space of the unit cell (interstitial region). The sphere radii used in the calculations are 2.5, 2.2, and 2.1 a.u. for Pb, Sr and S, respectively. A mesh of 47 special k-points for the binary compounds and 125 special k-points for the alloy were taken

© Cognizure. All rights reserved.

Table 1. Calculated lattice parameter (*a*) and bulk modulus (*B*) for PbS, SrS and their alloys at equilibrium volume.

	x	Lattice constant *a* (Å)			Bulk modulus *B* (GPa)		
		This work	Experiment	Other calculations	This work	Experiment	Other calculations
$Pb_{1-x}Sr_xS$	1	6.065	6.024[a]	6.076[b]	46.3	58[a]	47[b], 51.9[c]
	0.75	6.049			46.6		
	0.5	6.036			47.2		
	0.25	6.023			49.0		
	0	6.011	5.94[d]	6.012[e]	51.6	52.9[d]	52.1[e]

[a] Ref [9], [b] Ref [14] , [c] Ref [16] , [d] Ref [2], [e] Ref [8],

Table 2. The computed elastic constants (GPa) for $Pb_{1-x}Sr_xS$ at equilibrium and for various Sr concentrations.

Material	C_{11}			C_{12}			C_{44}		
	This work	Exp	Other calculations	This work	Exp	Other calculations	This work	Exp	Other calculations
PbS	130.81	124.0[a]	135.1[b]	22.21	33.0[a]	16.9[b]	20.60	23.0[a]	20.4[b]
$Pb_{0.75}Sr_{0.25}S$	132.34			18.22			24.25		
$Pb_{0.5}Sr_{0.5}S$	133.273			18.18			28.32		
$Pb_{0.25}Sr_{0.75}S$	136.353			17.97			30.39		
SrS	140.46		141[c]	17.12		17.2[c]	60		62.5[c]

[a] Ref [30], [b] Ref [31] , [c] Ref [14]

Table 3. Calculated shear modulus G, Young's modulus E, Poissons's ratio σ, shear wave modulus C_s, Kleinman parameter ξ, the ratio B/G and (C_{12}–C_{44}) for $Pb_{1-x}Sr_xS$ at zero pressure.

	x	G	E	σ	C_s	ξ	B/G	C_{12}-C_{44}
$Pb_{1-x}Sr_xS$	0	30,741	76,944	0,069	54,300	0,321	1,514	1,61
	0.25	34,434	83,696	0,060	57,060	0,289	1,311	-6,03
	0.5	37,775	89,460	0,054	57,547	0,288	1,180	-10,14
	0.75	39,822	92,981	0,050	59,192	0,283	1,112	-12,42
	1	60,663	126,667	0,028	61,670	0,273	0,763	-42,88

in the irreducible wedge of the Brillouin zone. To ensure proper convergence of the self-consistency calculation, the calculated total energy of the crystal converged to less than 0.1mRy.

3. Results and Discussion

3.1. Structural properties

In order to calculate the ground state properties of PbS, SrS and their ternary alloy, the total energies are calculated in rocksalt structure. The calculated total energies are fitted to the Murnaghan's equation of state [29] to determine the ground state properties such as the equilibrium lattice constant a and the bulk modulus B. Our calculated values for the equilibrium lattice constant *a* and bulk modulus *B* for the binary compounds and their alloys are summarized in the Table 1 together with available theoretical [8, 14, 16] and experimental [2, 9] data. The values for the lattice parameters *a* and the bulk modulus *B* for the binary compounds are in very good agreement with the measured ones.

We also calculate the elastic constants (C_{11}, C_{12} and C_{44}) at different compositions of $Pb_{1-x}Sr_xS$ alloys using the numerical first-principles method. Results of elastic constants are presented in Table 2. The traditional mechanical stability conditions on the elastic constants in cubic crystals are known to be $C_{11}-C_{12}>0$, $C_{11}+2C_{12}>0$, $C_{11}>0$ and $C_{44}>0$. Our results for elastic constants in Table 2 obey these stability conditions. It is clearly seen that the values of the elastic constants obtained from FP-LAPW calculations for the end-point compounds (i.e. PbS and SrS) are in better agreement with available experimental and theoretical results. Unfortunately, no comparison has been made for the elastic constants of the alloys of interest in the 0 < x < 1 composition range.

The knowledge of elastic constants allows the calculation of the shear constant C_s. It is also known as the rigidity modulus and defined as the ratio of shear stress to shear strain and it describes the material's response to shearing strains. For cubic crystal, the shear constant Cs is given by

$$C_s = \frac{1}{2}(C_{11} - C_{12}) \quad (1)$$

The calculated values of C_s are listed in Table 3. The C_s value increases from PbS to SrS. This implies that the lattice stability in $Pb_{1-x}Sr_xS$ decreases with increasing Sr concentration.

The Kleinman parameter, ξ, describes the relative positions of the cation and anion sublattices under volume-conserving strain distortions for which positions are not fixed by symmetry. It is known that a low value of ξ implies there is a large resistance against bond bending or bond-angle distortion and vice versa [32, 33]. The ξ value was calculated by the following relation [34]:

$$\xi = \frac{C_{11} + 8C_{12}}{7C_{11} + 2C_{12}} \quad (2)$$

The calculated ξ values are reported in Table 3. It is noted that the ξ value decreases from PbS to SrS. This indicates that the resistance to changes in bond length in $Pb_{1-x}Sr_xS$ increases with increasing Sr concentration.

© Cognizure. All rights reserved.

Young's modulus E and Poisson's ratios are frequently measured for polycrystalline materials when investigating their hardness. Young's modulus is a measure of the stiffness of a given material, whereas Poisson's ratio, is the ratio, when a sample is stretched, of the contraction or transverse strain (perpendicular to the applied load), to the extension or axial strain (in the direction of the applied load). These quantities are related to the bulk modulus and the shear modulus by the following equations [35]:

$$\begin{cases} E = \dfrac{9BG}{3B+G} \\ \sigma = \dfrac{3B-E}{6B} \end{cases} \quad (3)$$

Where

$$\begin{cases} G = \dfrac{G_R + G_V}{2} \\ G_r = \dfrac{5C_{44}(C_{11}-C_{12})}{4C_{44}+3(C_{11}-C_{12})} \\ G_V = \dfrac{C_{11}-C_{12}+3C_{44}}{5} \end{cases} \quad (4)$$

Our results concerning E and s are given in Table 3. We note that E increases from PbS to SrS. This implies that the stiffness of $Pb_{1-x}Sr_xS$ decreases with increasing Sr concentration. The values of s obtained for material of interest are ranging between 0 and 1. However, one should observe that σ decreases from PbS to SrS, thus under a given compression, the lateral expansion increases with increasing Sr concentration. Due to the lack of both experimental and theoretical data regarding ξ, G, E, σ and Cs for $Pb_{1-x}Sr_xS$, our results are predictions and may serve for a reference for future works.

The ductile-brittle nature of materials is often discussed in terms of elastic constants of the relevant material. The Cauchy's pressure, defined as the difference between the two particular elastic constants $C_{11} - C_{44}$ is considered to serve as an indication of ductility. If the pressure is positive (negative), the material is expected to be ductile (brittle). According to the empirical formula of Pugh [36], one can estimate the brittle and ductile behaviors of polycrystalline materials by considering the bulk modulus B as the resistance to fracture and the shear modulus G as the resistance to plastic deformation. This formula states that the critical value of the $\frac{B}{G}$ ratio separating the ductile and brittle behavior of materials is around 1.75; i.e., if $\frac{B}{G} > 1.75$ the material behaves in a ductile manner; otherwise the material behaves in a brittle manner. The obtained $\frac{B}{G}$ ratios for $Pb_{1-x}Sr_xS$ are less than 1.75 (brittle material). The consequence of brittle is the more sensitivity for thermal shocks, as the material cannot efficiently dissipate thermal stress via plastic deformations. Thus, a brittle solid cannot support large thermal shocks.

3.2. Thermal effects: Quasi-harmonic Debye model

To investigate the thermodynamic properties of PbS and SrS compoundsand their alloy under high temperature and pressure, we apply the quasi-harmonic Debye model [37], in which the non-equilibrium Gibbs function *G*(V; P, T)* can be written in the form of

$$G^*(V;P,T) = E(V) + P(V) + A_{vib}\left[\theta(V);T\right] \quad (5)$$

where *E(V)* is the total energy per unit cell, *PV* corresponds to the constant hydrostatic pressure condition, *θ(V)* is the Debye temperature, and A_{Vib} is the vibrational term, which can be written using the Debye model of the phonon density of states as [38, 39]

$$A_{vib}(\theta,T) = nkT\left[\frac{9\theta}{8T} + 3\ln\left(1-e^{-\theta/T}\right) - D\left(\frac{\theta}{T}\right)\right] \quad (6)$$

where *n* is the number of atoms per formula unit, *D(θ /T)* represents the Debye integral, and for an isotropic solid, *θ* is expressed as [38]

$$\theta_D = \frac{\hbar}{k}\left[6\pi^2 V^{1/2} n\right]^{1/3} f\left(\sigma\sqrt{\frac{B_S}{M}}\right) \quad (7)$$

M being the molecular mass per unit cell and B_S the adiabatic bulk modulus, approximated by the static compressibility [37]

$$B_S \cong B(V) = V\frac{d^2E(V)}{dV^2} \quad (8)$$

f (σ) is given by Refs [40, 41]; the Poisson σ is taken as 0.25 [42].

Therefore, the non-equilibrium Gibbs function *G*(V; P, T)* as a function of *(V; P, T)* can be minimized with respect to volume *V*.

$$\left[\frac{\partial G^*(V,P,T)}{\partial V}\right]_{P,T} \quad (9)$$

By solving Eq. (9), one can obtain the thermal equation of state (EOS) *V (P, T)*. The heat capacity C_V and the thermal expansion coefficient α are given by [43].

$$C_V = 3nk\left[4D\left(\frac{\theta}{T}\right) - \frac{3\theta/T}{e^{\theta/T}-1}\right] \quad (10)$$

$$S = nk\left[4D\left(\frac{\theta}{T}\right) - 3\ln\left(1-e^{-\theta/T}\right)\right] \quad (11)$$

$$\alpha = \frac{\gamma C_V}{B_T V} \quad (12)$$

Where γ is the Grüneisen parameter, which is defined as

$$\gamma = -\frac{d\ \ln\theta(V)}{d\ \ln V} \quad (13)$$

Through the quasi-harmonic Debye model, one could calculate the thermodynamic quantities of any temperatures and pressures of compounds from the calculated *E-V* data at *T* = 0 and *P* = 0.

© Cognizure. All rights reserved.

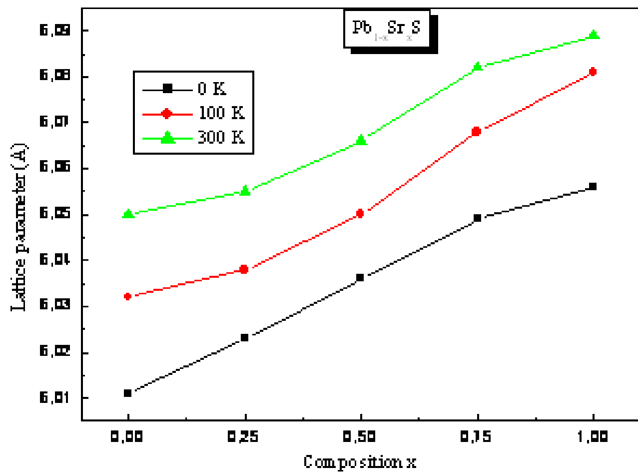

Figure 1. The relationships between lattice parameters and composition x at temperature 0, 100, 300 K respectively.

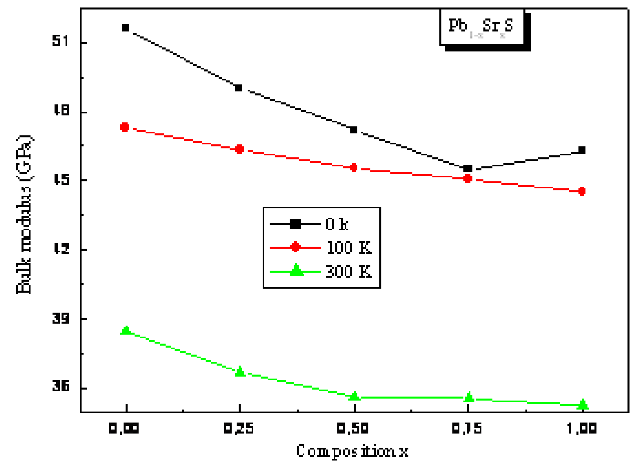

Figure 2. The relationships between bulk modulus and composition x at temperature 0, 100, 300 K respectively.

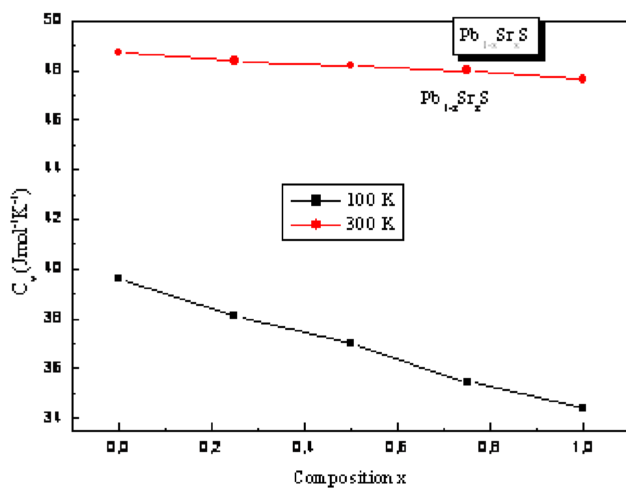

Figure 3. The heat capacity versus composition x at temperature 100 and 300 K, respectively.

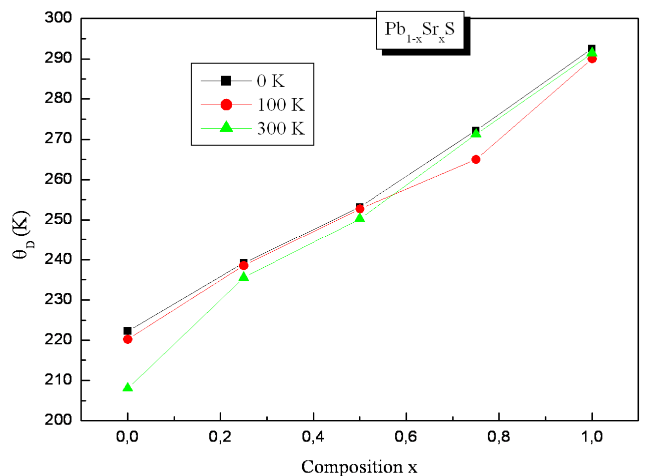

Figure 4. The relationships between Debye temperature and composition x at temperature 0, 100, 300 K respectively.

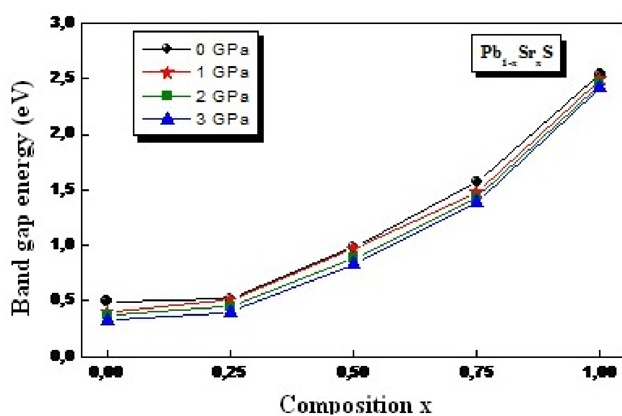

Figure 5. Calculated pressure dependence of energy band gap for $Pb_{1-x}Sr_xS$.

The thermal properties are determined in the temperature range from 0 to 300 K and at zero pressure, where the quasi-harmonic model remains fully valid.

The temperature effects on the lattice parameters of $Pb_{1-x}Sr_xS$ alloy at composition x are shown in Figure 1. The lattice parameter increases with increasing temperature and composition x. Figure 2 shows, as example, the composition dependence of the calculated bulk modulus at 0, 100 and 300 K. We remark that the bulk modulus decreases non-linearly with increasing of Sr content and temperature.

The variation of the heat capacity versus composition x at temperature 100 and 300 K at zero pressure is shown in Figure 3. With increasing temperature, C_V values decrease rapidly at a lower temperature, then decrease slowly in the high temperature.

The temperature dependence of Debye temperature versus composition x is illustrated in Figure 4. It is well shown that there is a strong non-linear increase.

In order to investigate the effect of the pressure on the size of the energy gaps of this alloy in the rocksalt structure, we have calculated the band gaps at different sets of pressures. Figure 5 shows the plots of the pressure variation of band gaps of $Pb_{1-x}Sr_xS$ alloy at composition x. It is clearly seen that the

© Cognizure. All rights reserved.

energy gaps exhibit the same type of response increasing with the pressure.

4. Conclusions

In conclusion, using a first-principle full potential linearized augmented plane wave (FP-LAPW) method based on the density-functional theory with the GGA for the exchange-correlation functional, the structural properties and elastic constants of $Pb_{1-x}Sr_xS$ in rocksalt structure have been calculated. The numerically calculated values showed generally reasonable agreement with the available experimental data. Through the quasi-harmonic Debye model, the dependences of lattice constant, bulk modulus, specific heat capacities and Debye temperature on temperature have been investigated. The pressure dependence of band gap quantities has been investigated.

References

1. A. Lipovskii, E. Kolovkova, V. Petricov, I. Kang, A. Olkhovets, T. Krauss, M. Thomas, J. Silcox, F. Wise, Q. Shen, S. Kycla, Appl. Phys. Lett. 71 (1997) 3406.
2. A. Delin, P. Ravindran, O. Eriksson, J.M. Wills, Int. J. Quantum Chem. 69 (1998) 349.
3. K. Nair, M. Ocampo, A. Fernandez, M.T.S. Nair, Sol. Energy Mater. 20 (1990) 235; P.K. Nair, A. Fernandez, M.T.S. Nair, Proc. SPIE Int. Soc. Opt. Eng. 1149 (1989) 88.
4. M.L. Cohen, J.R. Chelikowsky, Electronic Structure and Optical Properties of Semiconductors (2nd ed.), Springer Series in Solids States Sciences, Springer-Verlag, Berlin vol. 75 (1989).
5. G. Nimtz, B. Schlicht, B. Dornhaus, Narrow Gap Semi-Conductors: Springer Tracts in Modern Physics, Springer, New York (1983) and references therein.
6. Sushil Kumar, Zishan H. Khan, M.A. Majeed Khan, M. Husain, Curr. Appl Phys. 5 (2005) 561.
7. M.Lach-hab, A.D. Papaconstantopoulos, J.M. Mehl, J. Phys. Chem. Solids 63 (2002) 833.
8. S. Kacimi, A. Zaoui, B. Abbar, B. Bouhafs, J. Alloys Compd. 462 (2008) 135.
9. H. Luo, R. G. Greene, and A. L. Ruoff, Phys. Rev. B 49 (1994) 15341.
10. K. Syassen, Phys. Stat. Sol. A 91 (1985) 11.
11. Y. Kaneko and T.Koda., J. Cryst. Growth 86 (1988) 72.
12. D. Rached, M. Rabah, N. Benkhettou, B. Soudini, and H. Abid, Phys. Stat. Sol. B 241 (2004) 2529.
13. M. Dadsetani and A. Pourghazi, Phys. Rev. B 73 (2006) 195102.
14. R. Khenata, H. Baltache, M. Rerat, M. Driz, M. Sahnoun, B. Bouhafs, and B. Abbar, Physica B 339 (2003) 208.
15. D. Varshney, N. Kaurav, R. Kinge, R.K. Singh, Comp. Mater. Sci. 41 (2008) 529.
16. P. Bhardwaj, S. Singh, N.K. Gaur, J. Mol. Struct. (Theochem) 897 (2009) 95.
17. Yan Cheng, Lai-Yu Lu, Ou-He Jia, Qing-Quan Gou, Commun. Theor. Phys. 49 (2008) 1611.
18. Xiao-Cui Yang, Ai-Min Hao, Jie Yang, Yong-Hao Han, Gang Peng, Chun-Xiao Gao, Guang-Tian Zou, Chin. Phys. Lett. 25 (2008) 807.
19. H. Holloway and G. Jesion, Phys. Rev. B 26 (1982) 5617.
20. M. A. Tamor, L. C. Davis and H. Holloway, Phys. Rev. Lett. 52 (1984) 946.
21. M. A. Tamor, Solid State Commun. 58 (1986) 101.
22. L. C. Davis, Phys. Rev. B 28 (1983) 6961.
23. S. Labidi, M.Labidi, H.Meradji, S.Ghemid, F.ElHajHassan, Comp. Mater. Sci. 50 (2011) 1077.
24. [a] G.P. Srivastava, J.L. Martins, A. Zunger, Phys. Rev. B 31 (1985) 2561; [b] J.E. Bernard, A. Zunger, Phys. Rev. B 34 (1986) 5992; [c] A. Zunger, S.H. Wei, L.G. Ferreira, J.E. Bernard, Phys. Rev. Lett. 65 (1990) 353; [d] S.H. Wei, L.G. Ferreira, J.E. Bernard, A. Zunger, Phys. Rev. B 42 (1990) 9622.
25. P. Blaha, K. Schwarz, G.K.H. Madsen, D. Kvasnicka, J. Luitz, WIEN2k, An Augmented Plane Wave Plus Local Orbitals Program for Calculating Crystal Properties, Vienna University of Technology, Vienna, Austria (2001).
26. P. Hohenberg, W. Kohn, Phys. Rev. B 136 (1964) 864.
27. W. Kohn, L.J. Sham, Phys. Rev. A. 140 (1965) 1133.
28. J.P. Perdew, S. Burke, M. Ernzerhof, Phys. Rev. Lett. 77 (1996) 3865.
29. F.D. Murnaghan, Proc. Natl. Acad. Sci. U.S.A. 30 (1944) 5390.
30. O. Madelung, M. Schulz, and H. Weiss (eds.), Numerical Data and Functional Relationships in Science and Technology, Landolt-Bornstein, New Series, Springer, Berlin, Vol. 17 (1983).
31. Yi Zhang, Xuezhi Ke, Changfeng Chen, J. Yang, and P. R. C. Kent, Phys. Rev. B 80 (2009) 024304.
32. K. Kim, W.R.L. Lambrecht, B. Segall, Phys. Rev. B 50 (1994) 1502.
33. L. Kleinman, Phys. Rev. B 12 (1962) 2614.
34. W.A. Harrison, Electronic Structure and Properties of Solids, Dover, New York (1989).
35. M.W. Barsoum, T. El-Raghi, W.D. Porter, H. Wang, S. Chakraborty, J. Appl. Phys. 88 (2000) 6313.
36. S.F. Pugh, Philos. Mag. 45 (1954) 823.
37. M.A. Blanco, E. Francisco, V. Luaña, Comput. Phys. Commun. 158 (2004) 57.
38. M.A. Blanco, A. Martín Pendás, E. Francisco, J.M. Recio, R. Franco, J. Mol. Struct. (Theochem) 368 (1996) 245.
39. M. Flórez, J.M. Recio, E. Francisco, M.A. Blanco, A. Martín Pendás, Phys. Rev. B 66 (2002) 144112.
40. E. Francisco, J. M. Recio, J. M., Blanco, M. A., Martín Pendás, A., J. Phys. Chem. 102 (1998) 1595.
41. E. Francisco, M.A. Blanco, G. Sanjurjo, Phys. Rev. B 63 (2001) 094107.
42. J. P. Poirier, Introduction to the Physics of the Earth's Interior, Cambridge University Press, Oxford (2000) p. 39.
43. R. Hill, Proc. Phys. Soc. Lond. A 65 (1952) 349.

Cite this article as:

S. Labidi *et al.*: **First principles calculations of the structural and thermal properties of $Pb_{1-x}Sr_xS$ ternary alloys.** ScienceJet 2012, **1**: 3

© Cognizure. All rights reserved.

Formation of deuterium molecules in the cold interstellar medium: An experimental view

Lisseth Gavilan[a,*], Jean Louis Lemaire[a], Gianfranco Vidali[a,b]

[a] *LERMA/LAMAp, UMR 8112 du CNRS, de l'Observatoire de Paris et de l'Université de Cergy Pontoise, 5 mail Gay Lussac, 95000 Cergy Pontoise, France*
[b] *Current address: Physics Department, Syracuse University, Syracuse, NY, 13244, USA*

[*] *Author for correspondence: Lisseth Gavilan, email: lisseth.gavilan@obspm.fr*
Received 4 Feb 2012; Accepted 9 Apr 2012; Available Online 19 Apr 2012

Abstract

Our goal is to understand the formation of molecular hydrogen in the interstellar medium (ISM). To this end we use an experimental setup to investigate the roles played by the cosmic dust (modeled by an amorphous silicate surface) and the surrounding ISM gas (modeled as a beam of deuterium atoms) on D_2 formation. These experiments are performed in ultra-high vacuum conditions. We use a QMS (Quadrupole Mass Spectrometer) to monitor the dynamical coverage and sticking of D atoms and D_2 molecules on dust, while a REMPI-TOF (Resonantly Enhanced Multi-photon Ionization – Time of Flight) spectrometer monitors the newly formed D_2 molecules, assuming a formation rovibrational distribution peaking at v" = 4, J" = 2. These experiments confirm that a silicate pre-covered with D_2 molecules enhances the formation of new D_2 molecules.

Keywords: Astrochemistry; ISM atoms; ISM molecules; Molecular processes

1. Introduction

In recent years, the fields of surface science and astrophysics have merged to probe the relevant microphysics that has become crucial in astrophysical processes eventually leading to star formation. Our experimental study aims to understand a widespread gas-grain surface interaction occurring in the interstellar medium (ISM). We employ the FORMOLISM setup [1, 2] and use a multidisciplinary approach to study the reaction D(ads)+D(ads)→ D_2, where D(ads) is a gas-phase atom that has landed on the surface of a dust grain. With this apparatus we can detect if a D_2 molecule leaving the surface is in a rovibrational excited state. In a previous experiment [3] we showed that a good fraction of D_2 molecules leaves the surface of a silicate in the temperature range of 6 to 70 K.

2. Experimental setup

The gaseous environment in the interstellar medium is simulated via the application of several techniques ranging from atomic and molecular physics to non-linear optics. We employ an atomic source of H or D atoms produced by a microwave discharge at 2.45 GHz. We use a time of flight detector based on REMPI (resonantly enhanced multi-photon ionization) to select the newly formed molecules in an excited quantum state. We also employ surface science techniques that require the use of a quadrupole mass spectrometer (QMS).

The growing use of a QMS to monitor the gas species inside UHV chambers, in addition to the use of laser techniques, is key in experiments of this kind. A QMS allows us to apply techniques like the King and Wells method [4], which measures the residual gas pressure while irradiating a surface, or thermally programmed desorption (TPD), which allows us to understand the properties of particles released in the gas phase that had condensed on the surface of interest.

Furthermore, dust grains, whose surfaces catalyze the formation of molecules in the interstellar medium, can be also be synthesized in the laboratory. A variety of techniques simulate the formation conditions and the further processing acting on newly formed dust [5]. Dust surfaces can be prepared via laser pyrolysis [6], reactive thermal evaporation [7], laser ablation [8], ion sputtering [9] and sol-gel synthesis [10]. Our original sample was prepared via electron-beam evaporation of SanCarlos olivine (found on earth's surface) but the exact chemical composition of the coating cannot be determined from only IR spectroscopy because of the broadness of the bands and the uncertainties in the band position [11].

Additional dust samples have been prepared via laser ablation, in collaboration with the Jena Astrophysical Laboratory in Germany. The laser ablation/condensation setup is followed by the particle beam extraction. The laser ablation is done in a quenching gas atmosphere within a vacuum chamber. The amorphous grains from the hot condensation zone are then condensed on a substrate of choice. In our case, these substrates are optically polished silicon disks (300 µm) and KBr windows. The dust grain layer is about 160 nm. This thickness is chosen so that it is thermally conductive for cooling down to very low temperatures, and so that it causes no interference in IR diagnostics. To investigate the size and morphology of these grains, we apply IR spectroscopy and HRTEM techniques. Silicate grains are directly collected from a TEM grid from the extracted particle beam right after laser ablation. Crystalline dust can also be produced in the laboratory either by thermal annealing and electron beam heating.

The structure of the dust surface may play a role in the formation and internal excitation of new molecules.

© Cognizure. All rights reserved.

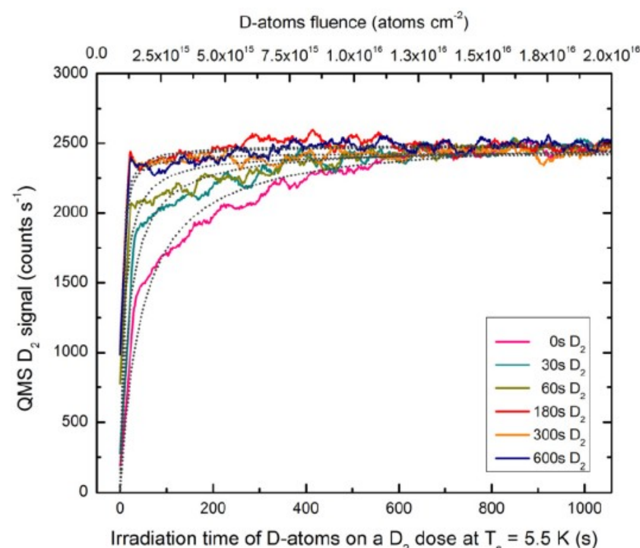

Figure 1. QMS signal of D_2 after a D_2 dose for x seconds (see inset) on the silicate surface, during irradiation with D atoms. This signal is the net result of i) the undissociated part of the deuterium beam, ii) the ejection of pre-coverage dose and iii) thenewly-formed D_2 molecules. Hyperbolic fits are overlaid. Deuterium formation is enhanced for greater D_2 pre-coverage doses.

Atomic diffusion on the surface is affected not only by the depth but also the height of the barrier. Previous experiments on amorphous silicates with different roughness and a single crystal silicate have shown effects on the formation of H_2 [12, 13]. In fact, larger binding energies for atoms were found on an amorphous silicate compared to a crystalline silicate [14]. Surface defects such as kinks, ledges and corners, increase the residence time of an atom on the surface and may increase the formation rate. We expect that the preparation of silicates with structural (amorphous or crystalline) and chemical extremes (Fe vs. Mg) will further enlighten the effect of these properties on the formation rate and rovibrational distribution of H_2.

3. Experiments and Results

In these experiments, we study the physisorption of deuterium atoms and their recombination by simulating ISM conditions such as dust at T = 5.5 K and 10 K and gas at T= 90 K. Our aim is to quantify the effect of D_2 formation enhancement and non-thermal desorption due to recombination on an amorphous silicate surface previously covered with D_2 molecules.

The internal excitation of a newly formed D_2 molecule is used in its detection via REMPI, effectively discerning nascent D_2 from the residual D_2 in the not entirely dissociated beam. The rovibrational distribution elucidates how much of the energy released in formation goes into internal energy and how much of the remaining energy goes into grain heating and translation of the desorbing molecule. Understanding this energy balance is important in the overall thermal balance of a cloud in the ISM, as the gained internal energy is reradiated in the infrared.

During irradiation with deuterium atoms, we note that the QMS curves reach the steady-state level more rapidly for larger D_2 pre-coverage doses (Figure 1). Since the D fluxes are the same for each experiment, corrected over minimal dissociation rate fluctuations, we expect the same contribution of the undissociated part of the beam for all QMS curves. Thus, the rise in the QMS signal is only due to the newly-formed D_2 and the ejected pre-coverage. The ejection of the pre-coverage is a consequence of the exothermic release of D_2 recombination (~4.5 eV). We see a convergence of the QMS curves for all initial doses at 1000s of D-atom irradiation. This steady state corresponds to the attainment of a steady D_2 production due to a maximum recombination rate. Thus, the presence of more pre-adsorbed D_2 molecules on the silicate surface enhances the recombination of D_2.

The recombination of D_2 on a dust grain surface (g) happens in the following steps,

$$D + g{:}D \rightarrow D{:}g{:}D \rightarrow D\text{-}D{:}g \rightarrow D_2^* + g \quad (1)$$

The first step is the sticking of an atom on the grain surface, followed by its diffusion on the grain. Atoms explore the surface and find each other. The newly formed molecule leaves the grain in an excited rovibrational state. We show that the enhancement of the formation rate on molecule-covered surfaces is due to enhanced diffusion. TPD profiles of each molecular dose show that the more energetic physisorption sites are first populated. The remaining sites have lower diffusion barriers, favoring thermal hopping. The difference in physisorption energies is also reduced, favoring quantum mechanical tunneling.

4. Conclusions and Outlook

We confirm the positive correlation between D_2 sub-monolayer pre-coverage doses on an amorphous silicate surface and D_2 formation [15, 16], which can lead to a formation enhancement of D_2 up to 65 ±10% on dust at T = 5.5 K. Furthermore, our results reveal that the non-thermal desorption due to D_2 recombination can lead to gas-phase feedback of up to a D_2 monolayer.

The enhancement of D_2 recombination is constrained by the inability of molecular deuterium to stack into multilayers. This constrains the amount of D_2 that the recombination process can eject back into the gas phase. Considering the extent of cold ISM environments, the coupled effect of an enhanced formation rate and pre-adsorbed molecular ejection will result in larger molecular gas phase abundances, constraining the regions where the atom/molecule transition begins. This could also have the consequence of retarding or further preventing molecular freeze-out on dust grains, an important condition in pre-protostellar core collapse [17]. Finally, the original dust grains we used are amorphous in nature. Future work will explore the structural and chemical variations of dust surfaces on molecular formation. We hypothesize that more binding surfaces will lead to a less energetic rovibrational distribution. Conversely, formation on crystalline surfaces is expected to lead to higher energy rovibrational energies, but may involve diminished sticking and an overall decrease of the formation rate.

Acknowledgments

Funding was provided by ANR (AgenceNationale De la Recherche; Contract 07-BLAN-0129).

G.V. is supported by NSF Astronomy & Astrophysics Division, Grant no. 0908108. L.G. is supported by LASSIE

© Cognizure. All rights reserved.

(European Community FP7 ITN Marie Curie Programme, Grant Agreement no. 238258.)

References

1. Saoud, B., Ph.D Thesis, Université de Cergy-Pontoise, http://www3.u-cergy.fr/LERMA-LAMAP/theses/Saoud_BAOUCHE_2004.pdf (2004).
2. Amiaud, L., Ph.D Thesis, Université de Cergy-Pontoise, http://tel.archives-ouvertes.fr/tel-00124797/en/ (2006).
3. J. L. Lemaire, G. Vidali, S. Baouche, M. Chehrouri, H. Chaabouni, H. Mokrane, ApJ 725 (2010) 156L.
4. D. King, M. G. Wells, Surf. Sci. 29 (1972) 454.
5. L. Colangeli, Th. Henning, J. R.Brucato, D. Clément, D. Fabian, O. Guillois, F. Huisken, C. Jäger, E. K. Jessberger, A. Jones, G. Ledoux, G. Manicó, V. Mennella, F. J. Molster, H. Mutschke, V. Pirronello, C. Reynaud, J. Roser, G. Vidali, L. B. F. M. Waters, A&AR 11 (2003) 97.
6. N. Herlin, I. Bohn, C. Reynaud, M. Cauchetier, A. Galvez, and J. N. Rouzaud, A&A 330 (1998) 1127.
7. F. J. M. Rietmeijer, J. A. Nuth, J. M. Karner, ApJ 527 (1999) 395.
8. J. R. Brucato, L. Colangeli, V.Mennella, P. Palumbo, E. Bussoletti, A&A 348 (1999) 1012.
9. L. Hanley,S. B. Sinnott, Surf. Sci. 500 (2002) 500.
10. C. Jäger, J.Dorschner, H.Mutschke, Th. Posch, Th. Henning, A&A 408 (2003) 193.
11. Z. Djouadi, L. d'Hendecourt, H. Leroux, A. P. Jones, J. Borg, D. Deboffle, N. Chauvin, A&A 440 (2005) 179.
12. G. Vidali, L. Li, J.Roser, R. Badman, Adv. Space Res. 43 (2009) 1291.
13. J. He, P. Frank, G. Vidali, Phys. Chem. Chem. Phys. 13 (2011) 1580.
14. H. B. Perets, A. Lederhendler, O. Biham, G. Vidali, L. Li, S. Swords, E. Congiu, J. Roser, G. Manico, J. R. Brucato, V. Pirronello, ApJ 661 (2007) L163.
15. T. R. Govers, L.Mattera, G. Scoles, J. Chem. Phys. 72 (1980) 5446.
16. E. Congiu, E. Matar, L. E. Kristensen, F. Dulieu, J. L. Lemaire, MNRAS 397 (2009) L96.
17. D. R. Flower, G. Pineau Des Forêts, C. M. Walmsley, A&A 436 (2005) 933.

Cite this article as:

Lisseth Gavilan *et al.*: **Formation of deuterium molecules in the cold interstellar medium: An experimental view.**
ScienceJet 2012, **1**: 4

© Cognizure. All rights reserved.

Optimization of the parameters of elaboration of the quaternary chalcopyrite $CuInGaSe_2$ for photovoltaic applications

M. Mezghache*, O. Benhalima, F. Chouia, B. Hadjoudja, B. Chouial, A. Chibani

Laboratoire des semi-conducteurs, Département de physique, Université Badji Mokhtar, Annaba, Algéria

Authors for correspondence: M. Mezghache, email: m_mezghache@hotmail.com

Received 4 Feb 2012; Accepted 14 May 2012; Available Online 14 May 2012

Abstract

Researches on solar cells based on chalcopyrite structure materials have shown a major interest in photovoltaic conversion. They are carried out at low cost with the efficiency of more than 20%. These materials have the power of absorption much more than that of silicon. The result is a less quantity of useful material, and a significant reduction in manufacturing costs. This work is entered in the framework of the elaboration and the study of the quaternary $CuInGaSe_2$ compound for the purpose of its deposit as an absorbent layer in the preparation of the solar cells. The elaboration parameters have been optimized; these parameters consist essentially of temperature and steps duration of heating, melting, crystallization and cooling. A scanning electron microscopy (SEM) associated to an energy dispersive spectrometry (EDS) was used to execute a quantitative study of the chemical elements of the $CuInGaSe_2$ compound obtained after optimization of the elaboration parameters. This study has shown that this compound presents a good stoichiometry. The analyses by X-ray diffraction have enabled us to study the crystalline structure of the elaborated quaternary compound and determine the different planes of crystallization. The preferred orientation following the plane (112) has been obtained. From the X-rays spectrum, we have calculated the lattice parameters a and c, the ratio c/a has been found close to 2. These analyses have shown that the obtained $CuInGaSe_2$ compound is polycrystalline and has a chalcopyrite structure.

Keywords: $CuInGaSe_2$; Chalcopyrite structure; Crystal growth; Parameters optimization; Solar cells

1. Introduction

The quaternary compound $CuInGaSe_2$ with chalcopyrite structure is an extremely promising material for the preparation of thin film-based solar cells [1-3]. This compound is distinguished by a high absorption coefficient and a gap of about 1.5 eV. The use of the $CuInGaSe_2$ compound as an absorbent for the preparation of the solar cells requires the improvement and the mastery of the properties of this type of material [4-7]. An efficiency of 20.3% was obtained [8]. The success of this compound depends strongly on its production in thin film [9,10] at low cost, since the deposit of these films is a significant part in the over all cost of the photovoltaic module. The purpose of this work is the elaboration and study of the quaternary compound $CuInGaSe_2$ for the purpose of its deposit as thin film by the close-spaced vapor transport (CSVT) method. The obtained $CuInGaSe_2$ ingots are then ground, sieved and the resulting fine powder was introduced in the CSVT reactor in order to be deposited as thin films.

2. Experimental

It is desired to obtain a compound with the following proportions: 25% of copper, 12.5% of indium, 12.5% of gallium and 50% of selenium. The elements Cu, In, Ga, and Se used were in the form of small grains with a consistent purity of 5N for copper and indium, and 6N for gallium and selenium. This ensures that the properties of the compound are not altered by the parasitic phases. We kept the same proportions for the mixture and the elements have been weighed with the ratio of their molar mass. The chosen reference material for the weighing procedure was gallium which is the least manageable element because of its low melting point. Once the mass of gallium is fixed, the quantities of the other three elements are obtained according to:

- M (Cu) = [M (Ga) × 2× molar mass of the Cu]/ molar mass of the Ga
- M (In) = [M (Ga) × molar mass of the In]/ molar mass of the Ga
- M (Se) = [M (Ga) × 4× molar mass of the Se]/ molar mass of the Ga

The prepared quantities were placed in a quartz tube in proportions targeting the researched compound. Then the tube was sealed under a vacuum of 10^{-5} torr and introduced in a furnace which can reach 1600 °C (Figure 1). The furnace temperature is measured by a thermocouple combined with a regulation program which describes the cycle of temperature that must undergo the Cu, In, Ga and Se mixture. Before introducing the mixture in the furnace, a test is done to ensure that the furnace will describe well the cycle. The dimensions of the furnace are: width: 60 cm, height: 80 cm, the diameter of the furnace tube containing the quartz tube: 5 cm. An X-rays diffractometer with copper Kα radiation (λ= 1.54051 Å) was used to analyze the crystalline structure and to determine the various planes of crystallization, and the different phases. The quantitative analysis of the chemical elements of $CuInGaSe_2$ ingot was made using an energy dispersive spectrometer (EDS).

© Cognizure. All rights reserved.

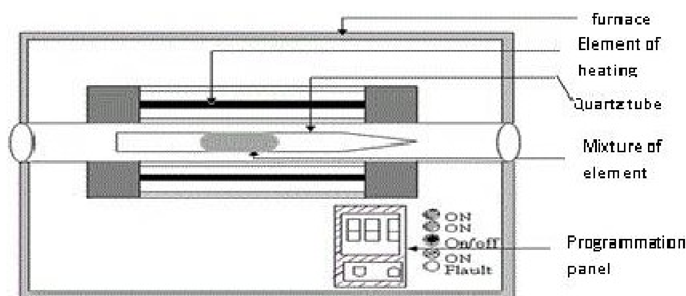

Figure 1. Schematic representation of the elaboration furnace with the quartz tube loaded by the mixture of the four elements.

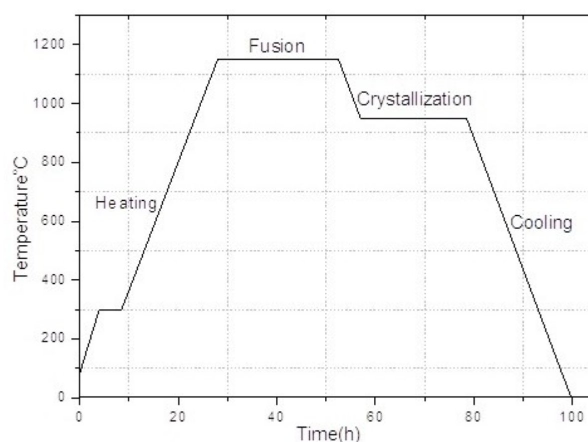

Figure 2. Thermal Cycle for $CuInGaSe_2$ elaboration.

Figure 3. Obtained $CuInGaSe_2$ ingot.

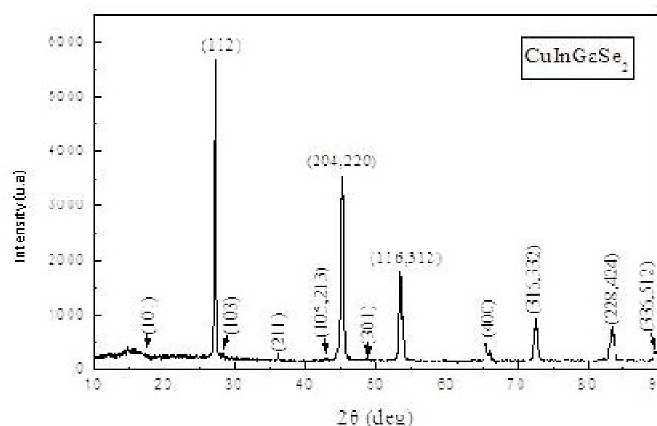

Figure 4. X-ray diffraction Spectrum of the elaborated $CuInGaSe_2$.

3. Results and Discussion

After many elaboration trails of the $CuInGaSe_2$ ingot, an optimized thermal cycle made up of seven steps was established (Figure 2):

Step 1: Progressive heating from the ambient temperature up to 300 °C in 5 hours.

Step 2: Fixed temperature at 300 °C for 5 hours; this allows the reduction of the selenium instability and the reactions influence of binaries formation during the temperature rise.

Step 3: Continuation of the progressive heating up to 1150 °C in 20 hours.

Step 4: Fixed temperature at 1150 °C for 25 hours, to allow the complete fusion of the four elements.

Step 5: Progressive cooling until 950 °C in 5 hours, to enable the transition to the crystallization phase.

Step 6: Fixed temperature at 950 °C for 20 hours, this allows the continuation of the crystallization and the formation of the chalcopyrite phase.

Step 7: Continuation of the progressive cooling until room temperature in 20 hours.

At the end of the thermal cycle which lasts 100 hours, the quartz tube is taken out of the furnace and the formed product is retrieved (Figure 3).

The ingot of CuInGaSe2 was characterized by EDS. The chemical composition of the compound is obtained after analysis of five different locations in the studied sample. The results obtained (25.82% for copper, 12.00% for indium, 12.92% for gallium and 49.26% for the selenium) show that our sample presents a good stoichiometry. The X-rays spectrum of the obtained ingot revealed the presence of several preferential orientations according to the planes (112), (220), (204), (116) and (312) (Figure 4). The plane (112) presents itself as a preferential orientation, the more intense is located at $2\theta = 27°$. Similar results have been reported by other authors [11-13]. Furthermore, Kanan *et al.* [14] have indicated that the planes of orientation (112) are desirable for the photovoltaic conversion. In addition to the orientation planes (112), (103), (105), (213), (204), (220), (116), (312), (400), (316), (332), (228), (424), (336) and (512) of the quaternary compound $CuInGaSe_2$, most of the characteristics peaks of the chalcopyrite structure (101), (211) and (301) are shown in our sample spectra.

From the X-rays spectrum, we calculated the lattice parameters *a* and *c*. The values obtained (*a*= 5.72, *c*=11.39) are in good agreement with those found in the literature [15]. The ratio c/a is close to 2 and the presence of the peaks (101), (211) and (301) (characteristics peaks of the chalcopyrite structure) shows that the obtained ingots of $CuInGaSe_2$ has a chalcopyrite structure.

© Cognizure. All rights reserved.

4. Conclusions

In the context of this work, we have optimized the elaboration parameters of $CuInGaSe_2$ ingots. The rate of heating, crystallization and cooling must be slow, at approximately 1°C/min. In addition to the fusion temperature at 1150°C, a first level at 300 °C and a second at 950 °C must be established in order to reduce the selenium instability during the heating for the first, and to allow the formation of the chalcopyrite phase during the crystallization for the second. The obtained ingots after optimization of the elaboration parameters have a good morphology. Analyses by X-rays diffraction have shown that the obtained $CuInGaSe_2$ crystallizes in a chalcopyrite structure with a preferential orientation (112) and with lattice parameters: a=5.72 Å and c=11.39 Å.

References

1. S. Ishizuka, K. Sakurai, A. Yamada, K. Matsubara, P. Fons, K. Iwata, S. Nakamura, Y. Kumura, T. Baba, H. Nakamishi, T. Kojima and S. Niki, Sol. Energy Mater. Sol. Cells 87 (2005) 541.
2. C. Grasso, M. Nanu, A. Goossens and M. Burgelman, Thin Solid Films 480-481 (2005) 87.
3. S. Marsillac, S. Dorn, R. Rocheleau and E. Miller, Sol. Energy Mater. Sol. Cells 82 (2004) 45.
4. G. P. Gorgut, A. O. Fedorchuk, I. V. Kityk, V. P. Sachanyuk, I. D. Olekseyuk and O. V. Parasyuk, J. Cryst. Growth 324 (2011) 212.
5. B. Dejene, Sol. Energy Mater. Sol. Cells 93 (2009) 577.
6. A. Drici, M. Mekhnache, A. Bouraoui, A. Kachouane, J. C. Bernede, A. Amara and M. Guerioune, Mater. Chem. Phys. 110 (2008) 76.
7. L. Zhang, Q. He, W. L. Jiang, F. F. Liu and C. J. Li, Y. Sun, Sol. Energy Mater. Sol. Cells 93 (2009) 114.
8. G. P. Gorgut, A. O. Fedorchuk, I. V. Kityk, V. P. Sachanyuk, I. D. Olekseyuk, O. V. Parasyuk, J. Cryst. Growth 324 (2011) 212.
9. M. V. Yakushev, A. V. Mudryi, V. F. Gremenok, E. P. Zaretskaya, V. B. Zelesski, Y. Feofanov and R. W. Martin, Thin Solid Films 451-452 (2004) 133.
10. R. Caballero and C. Guillen, Appl. Surf. Sci. 238 (2004) 180.
11. A. M. Andriesh, V. I. Verlan and L. A. Malahova, Thin Solid Films 451-452 (2004) 237.
12. H. Du, C. H. Champness, I. Shih and T. Cheung, Thin Solid Films 480-481 (2005) 42.
13. T. Yamaguchi, M. Naka, S. Niiyama and T. Imanishi, J. Phys. Chem. Solids 66 (2005) 2000.
14. M. D. Kannan, R. Balasundaraprabhu, S. Jayakumar and P. Ramanathaswamy, Sol. Energy Mater. Sol. Cells 81 (2004) 379.
15. G. W. El Haj Moussa, Ariswan, A. Khoury, F. Guastavino and C. Llinarès, Solid State Commun. 122 (2002) 195.

Cite this article as:

M. Mezghache *et al.*: **Optimization of the parameters of elaboration of the quaternary chalcopyrite $CuInGaSe_2$ for photovoltaic applications.** ScienceJet 2012, **1**: 5

© Cognizure. All rights reserved.

Optimisation of p-type a-SiC:H for p-i-n solar cells

J. D. Santos*, N. González, J. Cárabe, J. J. Gandía

CIEMAT, Av. Complutense, 22, 28040, Madrid, Spain

Authors for correspondence: JD. Santos, email: josedomingo.santos@ciemat.es

Received 4 Feb 2012; Accepted 25 Apr 2012; Available Online 28 Apr 2012

Abstract

P-a-SiC:H is suitable material for the development of optoelectronic devices. However, its chemical structure is complex, and its optoelectronic properties depend strongly on plasma stochiometry. In that sense, optimisation of the alloy characteristics is a fundamental step previous to the preparation of a-Si:H solar cells, since a high optical transmittance and electrical conductivity are required. In this work, a detailed study of the effect of deposition conditions on the properties of p-a-SiC:H was carried out. Diborane molecule presented a better doping efficiency, but the improvement on the p-a-SiC:H electrical properties saturated for concentrations $R_{DB}=[B_2H_6]/[SiH_4]\geq 0.01$. On the contrary, trimethylboron allowed obtaining a higher optical transmittance and gap energy. A clear correlation between carbon content and alloy structural disorder was found. This fact explained the deterioration of its electrical characteristics with a high methane concentration, $X_{CH4\text{-}GAS}$. The strong influence of the $X_{CH4\text{-}GAS}$ value on the p-a-SiC:H structure quality was used to improve its optoelectronic properties at low deposition temperatures (T<150ºC) without hydrogen dilution.

Keywords: Silicon-carbon; Amorphous; Diborane; Trimethylboron; PECVD; Optoelectronic properties

1. Introduction

P-doped amorphous silicon-carbide (a-SiC:H) is widely used in the fabrication of optoelectronic devices. Its low deposition temperature, large-area homogeneity, and tuneable optoelectronic properties are suitable for the development of front emitters in amorphous silicon p-i-n solar cells.

In this particular application, photons have to pass through the front emitter to be captured in the device absorber, and hence a p-a-SiC:H material with a high optical transmitance is necessary. On the other hand, since the p-layer should assure the correct collection of the photogenerated carriers, a high electrical conductivity is also required. Therefore, the improvement of the optoelectronic properties of the p-type a-SiC:H is an essential step for the development of this kind of solar cells.

In this process, it is necessary to find the concentration of methane (CH_4) and doping gas that allow obtaining a high gap energy ($E_{GAP}\geq 2eV$), and at the same time, a low activation energy ($E_A\leq 0.5eV$) [1]. Unfortunately, optical and electrical characteristics of the alloy compete with each other. For example, an excess of methane in the plasma could lead to a high density of voids within the structure and to the subsequent deterioration of the electrical conductivity [2,3]. On the other hand, a dopant excess could produce a high density of defects within the bandgap, leading to an increase of the optical absorption [4]. These effects show the complexity of the chemical structure of the p-type a-SiC:H, and the difficulties to develop a suitable material. Furthermore, such problems become accentuated when a very low deposition temperature is required, such as in the case of low-cost flexible substrates, since the reduced mobility of the plasma species favours a more disordered p-a-SiC:H structure.

Nowadays, it is still necessary to study these alloys in order to better understand how to improve their quality. Proof of this are the many existing studies, some of them very recent [5,6]. In this sense, this work tries to give additional information on the influence of deposition conditions on optoelectronic and structural characteristics. In particular, the effect of methane (CH_4) and doping-gas concentration in the plasma was studied in detail. Diborane (B_2H_6) and trimethylboron ($B(CH_3)_3$) were used as doping gases in order to compare how each of them affects the alloy characteristics. Finally, considering the growing interest in flexible and cheaper device development, the influence of the deposition temperature was analysed. Furthermore, a re-optimisation of the optoelectronic properties for the lowest temperature p-a-SiC:H is proposed on the basis of the re-adjustment of the plasma stoichiometry, without hydrogen dilution.

2. Experimental

Different p-type amorphous silicon-carbide film sets were prepared in a PECVD reactor at 13.56 MHz. The a-SiC:H layers were deposited onto Corning 7059 glass for UV-VIS transmittance-reflectance measurements. From these data, film thickness (around 200 nm in most studied cases), refraction index (n), and absorption coefficient (α) were obtained by using an in-house developed software [7] that follows previously reported calculation procedures [8,9]. By means of the Tauc plot of the absorption coefficient, the gap energy (E_{GAP}) and the Tauc slope parameter (B_{TAUC}) were extracted. Aluminium contacts were subsequently evaporated on each sample in order to determine their electrical conductivity (σ) and extended-state-conductivity activation energy (E_A). A thermostatic bath was used to vary the sample temperature. E_A was extracted from the temperature dependence of σ in the interval between 5-85ºC. Simultaneously, a-SiC:H layers were prepared onto <100> c-Si for Fourier transform infrared (FTIR) measurements. Thus, the different hydrogen, carbon

© Cognizure. All rights reserved.

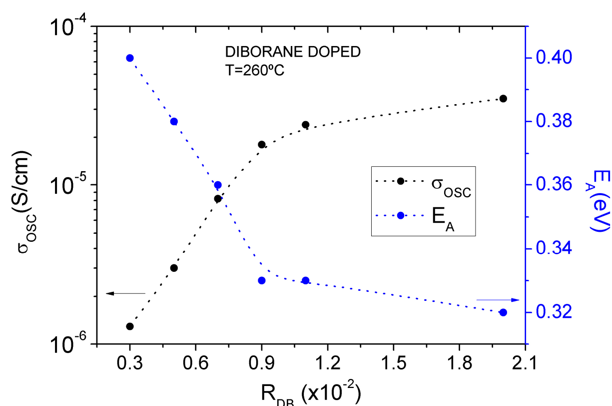

Figure 1. Effect of diborane concentration on the p-a-SiC:H electrical properties. Methane concentration was fixed at $X_{CH4\text{-}GAS}=0.78$. The activation energy was clearly reduced, showing a linear dependence on R_{DB} up to $1\cdot10^{-2}$. For further increasing R_{DB}, E_A and conductivity seemed to saturate.

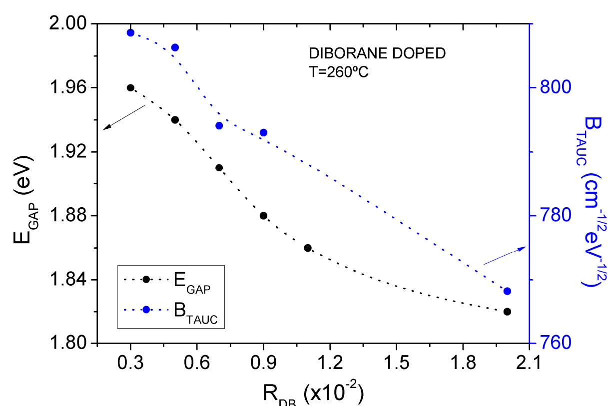

Figure 2. Effect of diborane concentration on the p-a-SiC:H optical properties. Methane concentration was fixed at $X_{CH4\text{-}GAS}=0.78$. The alloy transmittance presented a clear degradation as diborane concentration was increased. B_{TAUC} decreased for rising R_{DB} values, corroborating the transition to a more defective silicon-carbide alloy.

and silicon bond configurations were analysed in each sample. Finally, XPS spectroscopy was used to determine the carbon concentration in the p-a-SiC:H, defined as $X_{CARBON\text{-}SOLID}=[C]/([Si]+[C])$. The sample surface was previously etched in order to remove surface contaminants.

Plasma conditions were fixed to a gas pressure of 550 mTorr, an RF power of 1.3W, and a total flow of feedstock gases $[CH_4]+[SiH_4]=45$ sccm. Thus, the power per silane/methane molecule remained constant, and low enough to consider that p-type a-SiC:H layers were prepared in the so-called low-power regime [10]. Under such conditions, the influence of methane and doping-gas concentration on the a-SiC:H properties were analysed at a fixed substrate temperature of 260ºC.

In particular, the effect of boron-incorporation was studied in detail for the diborane (DB) doping case. The doping level, defined by the ratio of diborane flow to silane flow $R_{DB}=[B_2H_6]/[SiH_4]$, was varied from 3×10^{-3} to 2×10^{-2} while methane concentration remained constant $X_{CH4\text{-}GAS}=0.78$. On the other hand, the effect of carbon-incorporation was analysed for the diborane and trimethylboron (TMB) doping cases, since the alloy properties showed more important changes in these film sets. In order to study their optoelectronic properties evolution, the methane concentration, defined as $X_{CH4\text{-}GAS}=[CH_4]/([SiH_4]+[CH_4])$, was varied from 0.5 to 0.78, while dopant concentration remained constant at $R_{DB}=3\times10^{-3}$ and $R_{TMB}=6\times10^{-3}$ respectively (please note that the diborane molecule contributes with two boron atoms). Concerning structural properties, $X_{CH4\text{-}GAS}$ interval was extended to 0.3-0.78 in order to better understand possible changes in the nucleation process.

Finally, the effect of substrate-temperature on the p-a-SiC:H characteristics was studied for the TMB doping case. Deposition temperature was varied from 260 to 140ºC, just below the upper temperature limit for the most common plastic substrates such as PET. In this section, a re-optimisation of the material properties at 140ºC was obtained based on a $X_{CH4\text{-}GAS}$ re-adjustment.

3. Results and Discussion

3.1. Effect of doping-gas concentration

As expected, a progressive increase in the diborane gas concentration led to better p-a-SiC:H electrical properties. The activation energy was clearly reduced, showing a linear dependence on R_{DB} up to 1×10^{-2} (see Figure 1). However, for further increasing R_{DB}, E_A and conductivity seemed to saturate, and did not improve significantly afterwards.

On the contrary, optical characteristics presented a clear degradation as diborane concentration was increased. The gap energy decreased in the entire R_{DB} range (see Figure 2). This effect imposes an important restriction on the electrical properties, since photovoltaic devices need a high optical transmittance, and E_{GAP} values around 2 eV [1].

It is commonly accepted that boron incorporation causes a structural disorder increase, band-tail broadening, and the subsequent energy-gap reduction [11,12]. This phenomenon could also explain the E_A behaviour, since a less ordered a-SiC:H structure implies more traps and defects, which limit the tetrahedral coordination of boron and therefore its contribution to the injection of free holes in the valence band. Since the Tauc-slope has demonstrated a good correlation with the Urbach energy [6] (which defines the width of the bandtails states associated with variations of the bond angle and bond), its analysis allowed verifying this hypothesis (see Figure 2). Indeed, in the samples studied, B_{TAUC} decreased for rising R_{DB} values, corroborating the transition to a more defective silicon-carbide alloy.

As will be shown in future works, this structural distortion negatively affected the solar cell performance. Similar results have been obtained by others [13]. High performance p-i-n devices were developed by using the p-a-SiC:H material with a $R_{DB}=3\times10^{-3}$ value.

Subsequently, the effect of the doping gas concentration was studied for the TMB case. Surprisingly, the electrical properties did not improve too much. As an example, for $R_{TMB}=4\times10^{-2}$ (please remember that the DB molecule contributes with two boron atoms) the best σ was around 1×10^{-7} S/cm, a value one order of magnitude lower than suitable for device application [2]. This result indicated that the $B(CH_3)_3$ molecule has a lower doping effectiveness, and on

© Cognizure. All rights reserved.

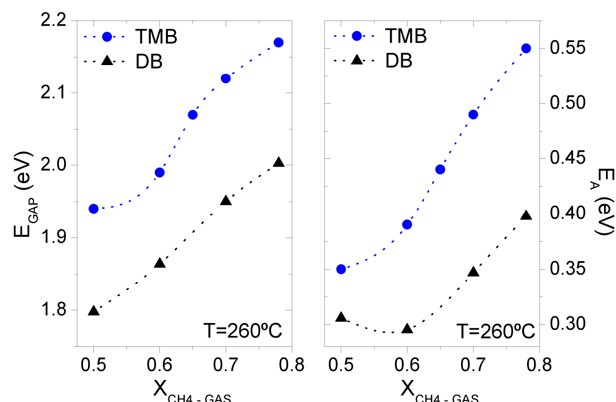

Figure 3. Effect of methane concentration on the p-a-SiC:H optoelectronic properties for DB and TMB doping. Diborane and trimethylboron concentrations were fixed at R_{DB}=3×10^{-3} and R_{TMB}=6×10^{-3} respectively. A greater $X_{CH4\text{-}GAS}$ value led to a noticeable energy-gap increase. Higher E_{GAP} values were obtained in the TMB doping case, suggesting an additional carbon contribution. Unfortunately, a greater CH_4 concentration caused an important degradation of the electrical properties, much more acuted in the TMB-doping case, as a consequence of its lower doping efficiency.

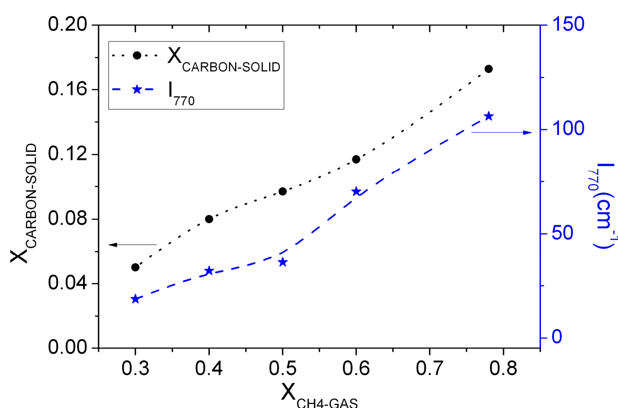

Figure 4. Effect of the methane concentration on the carbon content and Si-CH_3 integrated absorption for DB doping. Diborane concentration was fixed at R_{DB}=3×10^{-3}. As was expected, the carbon content obtained by means of XPS increased for higher $X_{CH4\text{-}GAS}$ values. Obtained values were lower than 20% for all the cases. There was a close relationship between carbon content and the concentration of methyl groups incorporated in the alloy.

the other hand, that the optimum methane concentration could not be directly translated from processes based on one doping gas to those based on the other.

3.2. Effect of gas methane concentration. DB vs. TMB doping

Optical properties were improved by increasing the methane concentration in the plasma. A greater $X_{CH4\text{-}GAS}$ value led to the substitution of weaker Si-Si bonds by stronger Si-C bonds, causing a noticeable energy-gap increase both for DB and TMB doping (see Figure 3-left). Nevertheless, E_{GAP} values were clearly higher in the TMB doping case. This result suggested an additional carbon contribution from the $B(CH_3)_3$ molecule, as others have previously observed [14].

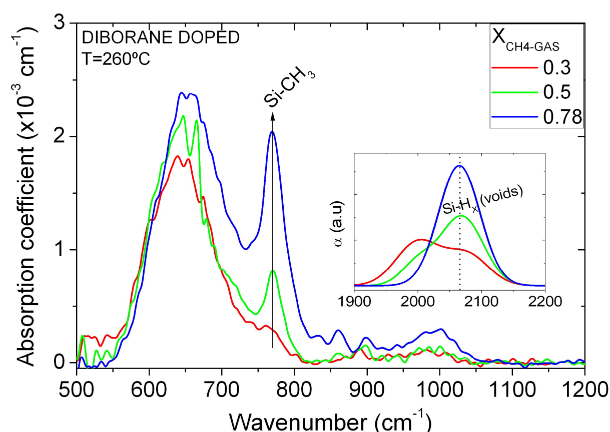

Figure 5. Effect of methane concentration on the p-a-SiC:H IR absorption for DB doping case. Diborane concentration was fixed at R_{DB}=3×10^{-3}. The FTIR analysis showed a clear increase of the Si-CH_3 absorption peak at 770 cm^{-1} with the $X_{CH4\text{-}GAS}$ value. On the other hand, absorption band at 1900-2200 cm^{-1} clearly shifted to higher energies, which indicated the formation of dihydride or clustered monohydride Si-H bonds as carbon content increased.

Unfortunately, a greater CH_4 concentration caused an important degradation of the electrical properties, much more accused in the TMB-doping case, as a consequence of its lower doping efficiency. Yet, in this last case the E_A reduction obtained by decreasing $X_{CH4\text{-}GAS}$ was greater than in the diborane-doping case, which saturated for $X_{CH4\text{-}GAS}$<0.6 (see Figure 3-right). Thus, for a $X_{CH4\text{-}GAS}\approx$0.6, the TMB doped alloy presented the same optoelectronic quality that the diborane doped material used in the solar cells fabrication (see section 3.1). Amorphous silicon p-i-n devices were also developed with this trimethylboron doped p-a-SiC:H.

Such a deterioration of the electrical properties has been related to the way in which carbon is introduced in the alloy structure in the so-called low-power regime. In these conditions, the RF power applied to plasma remains below the threshold necessary to decompose the CH_4 molecule in a direct way. Solomon et al. proposed that in this low-power regime the CH_4 decomposition takes place through reactions with other chemical species resulting from the SiH_4 decomposition (SiH, SiH_2, SiH_3) [10]. This fact favours the incorporation in the alloy of Si-CH_3 groups, which induce a greater perturbation during the nucleation process and lead to a more disordered structure.

Indeed, the compositional and structural analysis of DB-doping p-a-SiC:H films seemed to confirm these results. The XPS results revealed a surprisingly low carbon content, below 20% for all the studied samples, which was in agreement with the unlikely direct decomposition of CH_4 (see Figure 4).

On the other hand, the FTIR spectra showed a noticeable increase of the absorption peak at 770 cm^{-1} for higher $X_{CH4\text{-}GAS}$ values, which suggested a greater Si-CH_3 bond density in the alloy (see Figure 5). In order to better study this phenomenon, the absorption band at 500- 850 cm^{-1} was deconvoluted in its different vibrational modes, the Si-H_x (x=1,2,3) peak at 640 cm^{-1}, the Si-C peak at 720 cm^{-1}, and finally the Si-CH_3 peak at 770 cm^{-1}. Thus, the integrated absorption (defined as $I=\int\alpha(\omega)/\omega{\cdot}d\omega$) was calculated for the Si-CH_3 mode. The comparative analysis of methane concentration dependence of I_{770} and $X_{CARBON\text{-}SOLID}$ presented

© Cognizure. All rights reserved.

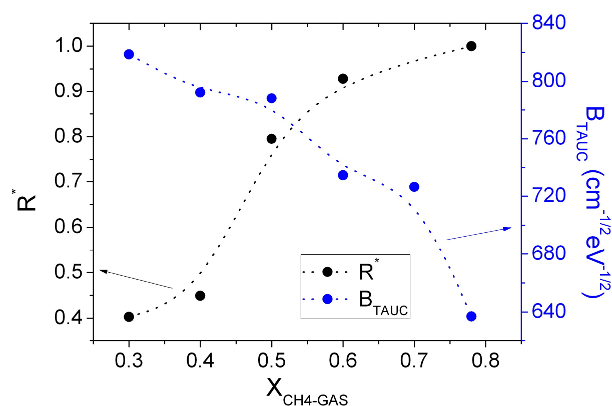

Figure 6. Effect of methane concentration on the microstructure parameter and Tauc-slope for DB doping case. Diborane concentration was fixed at R_{DB}=3×10^{-3}. R^* presented a noticeable rise as the methane concentration increased, which indicated that carbon incorporation favoured the bonding of hydrogen to silicon as dyhidride or clustered bonds. As a consequence the structural disorder increased, as it could be extracted from B_{TAUC} decreased with the gas methane concentration.

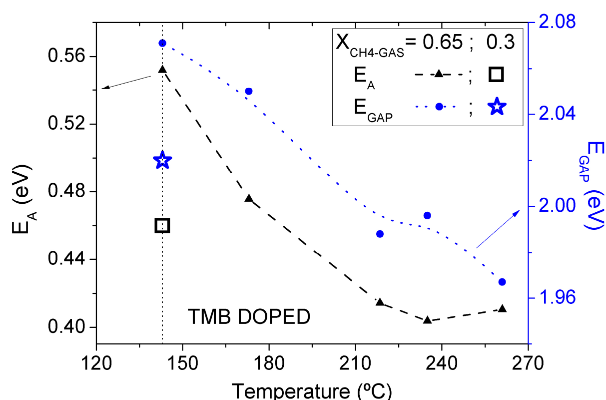

Figure 7. Effect of deposition temperature on the p-a-SiC:H optoelectronic properties for TMB doping case. Trimethylboron concentration was fixed at R_{TMB}=6×10^{-3}. The activation energy showed a noticeable deterioration for temperatures below 200ºC. In contrast, the energy-gap improved by decreasing the deposition temperature. The electrical properties degradation can be partially hindered by reducing $X_{CH4\text{-}GAS}$ from 0.65 to 0.3.

an almost linear relationship in both cases (see Figure 4). This fact indicated the existence of a close relationship between carbon content and the concentration of methyl groups incorporated in the alloy structure as Solomon et al. suggested [10]. Different researches have directly related the incorporation of these CH_3 groups with the formation of voids in the a-SiC:H material. However, this carbon content rise also led to additional effects that caused a material density loss [3].

It is well known that the absorption band at 1900-2200 cm^{-1} is composed of two contributions, a peak at 2000 cm^{-1} related to Si-H bonds surrounded by a dense network, and a peak at 2090 cm^{-1} usually associated with Si-H_X (X=1,2,3) bonds at "free" surface, e.g. voids [1, 2]. Thus, the so-called microstructure parameter (defined as $R^*=I_{2090}/(I_{2000}+I_{2090})$) gives additional information about the porosity of the alloy.

For the studied p-a-SiC:H films, the R^* presented a noticeable rise as the methane concentration increased (see Figure 6). In fact, for $X_{CH4\text{-}GAS}\geq 0.6$ (equivalent to $X_{CARBON\text{-}SOLID}\geq 0.12$) the band shift from 2000 to 2090 cm^{-1} was almost complete (see absorption band at 1900-2200 cm^{-1} in Figure 5), and the obtained $R^*\approx 1$. These results indicated that carbon incorporation favoured the formation of a less dense and more disordered a-SiC:H structure, as a consequence of hydrogen bonding to silicon as dihydride or clustered monohydride bonds.

A more detailed study of the optical properties allowed corroborating the mentioned effect on the alloy disorder. The Tauc-slope parameter decreased clearly with the gas methane concentration, suggesting an increase in a-SiC:H disorder, and the consequent higher density of defects (see Figure 6). All these results explained the previously mentioned degradation of the electrical properties as methane concentration increased.

3.3. Effect of deposition temperature

The substrate-temperature reduction had an important impact on the optoelectronic properties of the p-a-SiC:H. The activation energy showed a noticeable deterioration for temperatures below 200ºC (see Figure 7). In contrast, the energy-gap improved more than 0.1 eV by decreasing the deposition temperature from 260 to 140ºC.

Such behaviour was similar to what was observed as the methane concentration was raised. In this sense, the evolution of the optoelectronic properties suggested a temperature dependence of the amount of carbon incorporated to the alloy structure. However, the XPS analysis revealed that the carbon content in the p-a-SiC:H remained almost invariant (see Figure 8). Furthermore, the FTIR results did not show any relevant differences in the absorption peaks associated with carbon (see Figure 9).

On the contrary, silicon-bonded hydrogen increased clearly for lower temperatures (see Figure 8). This effect was related to a slower hydrogen elimination rate on the growing surface [15]. As a consequence, hydrogen from a-Si:H growth precursor SiH_3 is accumulated, which leads to the formation of Si-H_2 and Si-H_3 bonds. Indeed, the associated IR absorption peaks at 800 and 900 cm^{-1} showed a clear increase for the lower temperature (see Figure 9). Furthermore, this observation was reinforced by the detection of progressive shift toward higher energies of the 1900-2200 cm^{-1} absorption band as the temperature decreased. A higher Si-H_x (x=2, 3) concentration in the solid means a greater band gap, but also a more porous structure, as could be inferred from the refraction-index evolution (see Figure 8). This last result explained the observed deterioration of the electrical properties.

However, methane-concentration dependence of the p-a-SiC:H properties at 260ºC demonstrated that a lower $X_{CH4\text{-}GAS}$ value led to a better compactness and activation energy. Therefore, it was expected that the electrical characteristics of the lower-temperature alloy could be partially recovered by decreasing the methane concentration in the plasma. This hypothesis was verified for a substrate temperature of 140ºC, just below the typical upper limit for most plastic substrates. A $X_{CH4\text{-}GAS}$ reduction from 0.65 to 0.3 caused an important E_A decrease around 0.1 eV (see Figure 7). This activation energy value was not as good as that obtained at the highest temperature. Nevertheless, it is important to notice that hydrogen dilution was not used during the growing process in order to improve the electrical properties of the material. Thus, the transparent-conductive-oxide (TCO) chemical reduction

© Cognizure. All rights reserved.

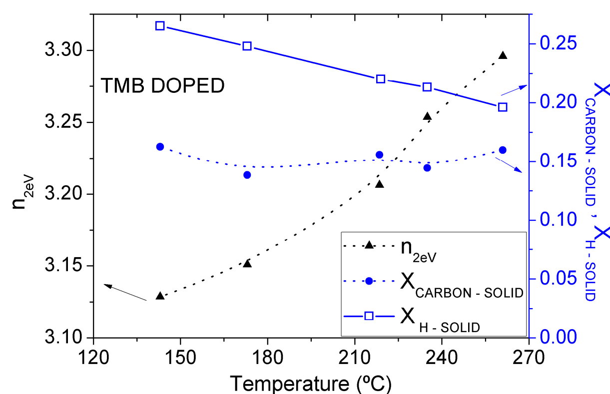

Figure 8. Effect of deposition temperature on the refraction index, carbon content, and hydrogen concentration for TMB doping case. Trimethylboron and methane concentrations were fixed at R_{TMB}=6×10^{-3} and $X_{CH4\text{-}GAS}$=0.65 respectively. Silicon-bonded hydrogen increased clearly for lower temperatures. On the contrary, the XPS analysis revealed that the carbon content in the p-a-SiC:H remained almost invariant. A more porous structure was obtained at lower temperatures, as could be inferred from the refraction-index evolution.

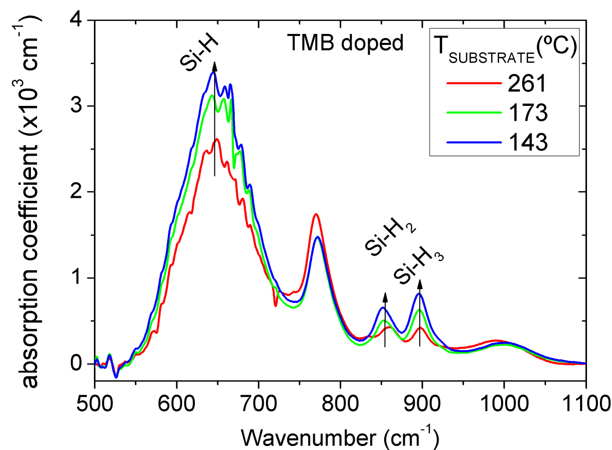

Figure 9. Effect of deposition temperature on the p-a-SiC:H IR absorption for TMB doping case. Trimethylboron and methane concentrations were fixed at R_{TMB}=6×10^{-3} and $X_{CH4\text{-}GAS}$=0.65 respectively. Hydrogen accumulation leads to the formation of Si-H_2 and Si-H_3 bonds, favouring a less dense structure. The associated IR absorption peaks at 800 and 900 cm^{-1} showed a clear increase for the lower temperature.

usually observed in the fabrication of a-Si:H solar cells would be minimized, favouring a short circuit increase [16]. Furthermore, since the hydrogen content remained high in this p-a-SiC:H at 140ºC, the energy gap was maintained over the 2-eV lower limit typically used as the criterion to validate front-emitter transparency.

All these results suggested that these deposition conditions were suitable for the fabrication of p-i-n devices onto plastic substrates. In future works, the applicability of this material for the development of flexible solar cells will be shown.

4. Conclusions

The dependence of the p-a-SiC:H properties on plasma composition and substrate temperature was analysed in detail. A clear improvement in the electrical characteristics was obtained by increasing the diborane concentration up to $R_{DB}=[B_2H_6]/[SiH_4]=0.01$. For further R_{DB} increase, E_A and σ saturated as a consequence of a structural distortion. Additionally, this phenomenon caused an important deterioration of the alloy optical properties. A suitable material for the development of high performance solar cells was found for R_{DB}=3×10^{-3}. The gap energy was modified by adjusting methane gas concentration $X_{CH4\text{-}GAS}$, and hence, carbon content. However, a higher CH_4 concentration in plasma also caused the incorporation of CH_3 groups and the formation of Si-H bonds as dihydride or clustered monohydride bonds. These two phenomena led to a more distorted and porous structure, and hence poorer electrical properties. This electrical conductivity deterioration was less important when using diborane owing to its higher doping efficiency. On the contrary, when TMB was used as the doping gas a higher optical transmittance was observed, probably because of an additional carbon contribution from the $B(CH_3)_3$ molecule. A high quality p-a-SiC:H was obtained for $X_{CH4\text{-}GAS}$=0.6 suitable for p-i-n device fabrication. The substrate-temperature reduction gave rise to variations of the p-a-SiC:H properties similar to those observed as $X_{CH4\text{-}GAS}$ was increased. When the substrate temperature was lowered, carbon content remained constant, but a higher E_{GAP} was obtained as a consequence of the incorporation of more hydrogen atoms. The observed increase of Si-H_x (x=2, 3) bonds at lower temperatures favoured a less dense structure with worse electrical properties. A p-a-SiC:H material with a better compactness and activation energy was obtained at 140ºC by re-adjusting the $X_{CH4\text{-}GAS}$ value. This alloy fulfilled the necessary requirements to develop flexible solar cells.

Acknowledgement

Partial financial support for this work has been provided by the Spanish Ministry of Science and Innovation under the projects AMIC (ENE2010-21384-C04-01) and INNDISOL (IPT-420000-2010-6).

References

1. R. E. I. Schropp, M. Zeman, Amorphous and Microcrystallline Silicon Solar Cells, Kluwer Academic Publishers, Dordrecht (1998).
2. A. V. Shah., Thin-Film Silicon Solar Cells, Engineering science: Micro- and Nanotechnology, EPFL Press (2010).
3. R. A. C. M. M. van Swaaij, A. J. M. Berntsen, W. G. J. H. M. van Sark, H. Herremans, J. Bezemer, W. F. van der Weg, J. Appl. Phys. 76 (1994) 251.
4. Y. Poissant, P. Roca I Cabarrocas, J. Non-Cryst. Solids 266 (2000) 1134.
5. B. Akaoglu, K. Sel, I. Atilgan, B. Katircioglu, Opt. Mater. 30 (2008) 1257.
6. G. Ambrosone, D. K. Basa, U. Coscia, P. Rava, Thin solid films 518 (2010) 5871.
7. JJ. Gandía, Células solares basadas en aleaciones de silicio amorfo y microcristalino, PhD Thesis, Universidad Complutense Madrid (2007).
8. JL. Hernandez-Rojas, ML. Lucia, I. Martil, G. Gonzalez-Diaz, J. Santa-Maria, F. Sanchez-Quesada, Appl. Opt. 31 (1992) 1606.
9. Y. Hishikawa, N. Nakamura, S. Tsuda, S. Nakano, Y. Kishi, Y. Kuwano, Jpn J. Appl. Phys. 30 (1991) 1008.

© Cognizure. All rights reserved.

10. I. Solomon, M. P. Schmidt, H. Tran-Quoc, Phys. Rev. B. 38 (1998) 9895.
11. J. Ristein and G. Weiser, Sol. Energ. Mater. 12 (1985) 221.
12. F. Demichelis, C. F. Pirri, E. Tresso, G. Dellamea, V. Rigato, and P. Rava., Semicond. Sci. Technol. 6 (1991) 1141.
13. A. Hadjadj, P. St'ahel, P. Roca i Cabarrocas, V. Paret, Y. Bounouh, JC. Martin, J. Appl. Phys. 83 (1998) 830.
14. Z. Y. Wu, B. Drevillon, M. Fang, A. Gheorghiu, C. Senemand, J. Non-Cryst. Solids 137 (1991) 863.
15. W. M. M. Kessels, A. H. M. Smets, D. C. Marra, E. S. Aydil, D. C. Schram, and M. C. M. van de Sanden., Thin Solid Films 383 (2001) 154.
16. S. Major, S. Kumar, M. Bhatnagar, K. L. Chopra, Appl. Phys. Lett. 49 (1986) 394.

Cite this article as:

J. D. Santos *et al.*: **Optimisation of p-type a-SiC:H for p-i-n solar cells.** ScienceJet 2012, **1**: 6

© Cognizure. All rights reserved.

Visible evidence for the formation of copper complexes in garlic extracts treated with copper sulfate and sodium nitrite mixture

Nicholas Sarpong Sarfo[a], Ibok Nsa Oduro[a], Kwabena Justice Sarfo[b,*]

[a] Department of Biochemistry and Biotechnology, Kwame Nkrumah University of Science and Technology, Kumasi, Ghana
[b] Department of Biochemistry, University of Cape Coast, Cape Coast, Ghana

[*]Author for correspondence: Kwabena Justice Sarfo, email: sarfojsk@yahoo.com
Received 4 Feb 2012; Accepted 27 Mar 2012; Available Online 19 Apr 2012

Abstract

Spectrophotometric evidence is described for the formation of copper complexes when crude garlic extracts were titrated with aliquots of equimolar concentration mixture of sodium nitrite and copper sulfate. Titrations could be monitored for all four different extracts prepared for each of the two garlic varieties used by the regeneration of a single diminished peak of copper(II) at a wavelength of 530 nm. The titration plots conform to the mole ratio and Job's continous variation plots of metal-ligand complexation. The sigmoidal absorbance plots obtained by the mole ratio method showed strong variations in the characteristic minimum, maximum, and the inflection points which were dependent on the type of garlic extract and on the variety of garlic. The similarity with the sigmoidal plot of copper–alanine titration is also provided in support of complexation of copper with components in garlic extract. The spectrophotometric patterns suggest complexation of copper(II) with dipeptide bonds and nitrosothiols. Thus, on average there was more than one inflection point per titration plot. The use of Jaccard's similarity relation to determine pairs of extracts of the two varieties of garlic likely to contain complexes common to the two is also provided. This study will help to delineate conditions under which $CuSO_4/NaNO_2$ decomposition reaction can be used for spectrochemical analysis of garlic and garlic products and for the investigation of garlic-derived copper complexes for nutritional and medicinal use.

Keywords: Visible absorption; Copper complexes; Garlic extracts; Inflection points; Similarity index; Decomposition reaction

1. Introduction

The properties of a metal-organic molecular complex are dependent on the nature of reactants and reaction conditions used for the synthesis [1]. Metals in the form of salts, carbonyls, hydroxides, and oxides have been used in the preparation of coordination products with synthetic and natural organic molecules as ligands [2, 3]. Naturally occurring metal ligands are concentrated in different parts of the plant including; seeds, leaves, roots, fruits, bark, and flowers. Plant-derived ligands comprise both primary and secondary metabolites which are mostly organic acids [4]. Copper-natural ligand complexes play an important role in cell physiology and therefore the search of plant materials for molecules for the preparation of novel complexes will expand the application of copper in the food industry, in nutrition, health, and research [5]. The search of such substances with new use as therapeutics, food supplements, or reagents will increase the value of certain cultivated food and medicinal crops.

As part of the achievement of this goal, this study was designed to determine spectrophotometric evidence for the formation of copper complexes in crude extracted solutions of garlic *in situ* by the treatment with the decomposition reaction of copper sulfate and sodium nitrite. Garlic (*Allium sativum*) is widely used in foods and for medicinal preparations. The phytochemical base of garlic is well-known much of which can serve as redox ingredients in metal complexation [6]. The use of the decomposition reaction of sodium nitrite and copper sulfate for the induction of copper-natural ligands complexation has not been explored. The ambidentate nature of nitrite ion towards metal centers can generate an initial Cu^{2+}/Cu^{1+} redox couple *in situ* which could induce copper complexation with ligands in a crude garlic extract in a single pot reaction at ambient conditions [7]. The visible spectrophotometric information would be a useful guide for the search, characterization and applications of garlic-derived copper complexes.

2. Experimental

2.1. Preparation of reagents and extraction buffers

Analytical grade compounds were used for the preparation of all solutions. Borate buffers and 0.1 M stock solutions of copper sulfate, sodium nitrite, and HCl were prepared with double distilled water. Three borate extraction buffers were prepared: a) 0.1 M boric acid/sodium tetraborate buffer at pH 10.0; b) 0.1 M boric acid/sodium tetraborate buffer with 6 M urea at pH 10.0; and c) 0.1 M boric acid/sodium tetraborate with 10% sodium dodecyl sulfate at pH 10.0.

2.2. Preparation of garlic extracts

The two varieties of soft neck garlic (*Allium sativum var. sativum*) Arthichoke and Creole which were used in this study are sold in Ghanaian markets as the Alata (Ala) and Chinese (Creole) garlic respectively. The garlic bulbs were washed thoroughly with double distilled water and used directly for sample preparation. For the preparation of borate-extractive ligands, 10 g of garlic bulbs from each variety were ground in 20 mL of each of the extraction buffers (a, b, c) in an ice-cooled environment. The homogenate was centrifuged

© Cognizure. All rights reserved.

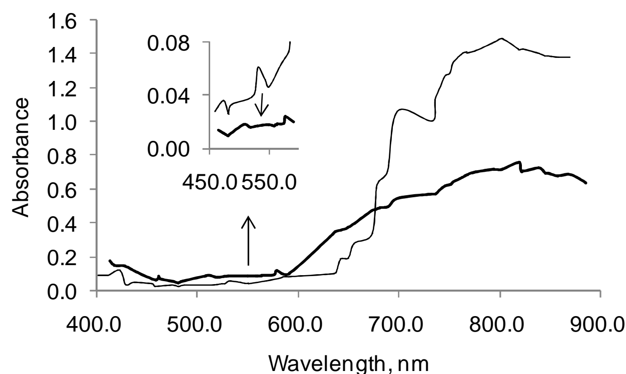

Figure 1. Visible spectra of 0.1 M $CuSO_4$ solution (—) and a decomposition reaction mixture of 0.1 M $CuSO_4$ and 0.1 M $NaNO_2$ (**—**). The inset highlights the diminished peak at 530 nm. NOTE: Absorbance values have been adjusted in order to place the $CuSO_4$ spectrum on top for clarity.

at 12,000 rpm for 15 min. The supernatant was decanted and stored at -20 °C prior to use as borate-extractive ligands. Urea and sodium dodecyl sulfate were used to solubilize membrane-bound proteins and peptides and to release co-existing small organic molecules. Garlic extract was also prepared with 0.1 M HCl and used as HCl-extractive ligands. The amounts of protein in the borate extracts were quantified using the biuret method [8].

2.3. Titrations and absorbance measurements

First, the mole ratio mode of titration was adapted for the titration of the different garlic extracts against copper sulfate and sodium nitrite decomposition mixture [9]. 3 mL each of 0.1 M sodium nitrite and 0.1 M copper sulfate in 0.1 M HCl were titrated with increasing volumes (0, 0.5, 1.0, 1.5, 2.0, 2.5, 3.0, 3.5, and 4.0 mL) of garlic extracts in a final volume of 10 mL adjusted with the corresponding extraction buffer. Titrations of the decomposition reaction mixtures (6 mL) with only the extraction buffers (4 mL) were performed and used as blanks during the absorbance recordings. Absorbance was recorded after 10 min of equilibration at room temperature at wavelength of 530 nm determined by wavelength scanning using a UV/visible spectrophotometer (Shimazu, Japan) with 1 cm path length. Absorbance values were used to plot spectral curves for the titrations. The titration of alanine against a copper phosphate suspension monitored at 630 nm as previously reported by others [10] was replicated and used as the standard sigmoidal plot for the compliance of a metal-ligand complexation which is based on the mole ratio mode of titration. Titrations of the extracts against the decomposition mixture were again conducted using the Job's [11] continuous variation method which was also monitored at 530 nm.

2.4. Data analysis

Absorbance values were recorded on spreadsheets and used to construct absorbance plots. The plots were further treated with the first derivative method to extract values for the inflection points for each plot using Microsoft Excel 2007 edition. These values were scored for each of the extracts depending on their presence (1) or absence (0) and used for the determination of the Jaccard similarity index [12]. Data from the continuous titration method were plotted to determine the ratio of the decomposition mixture to the extract that will give the maximum absorption at 530 nm.

3. Results and Discussion

Evaporation, pH, temperature and chemical reactions are common strategies used to induce metal-ligand complexation [13]. This study has established visible evidence for the induction of copper complexation with crude garlic extracts by the reaction of Cu(II) sulfate and sodium nitrite. Addition of an alkaline and acidic garlic extract to acidic decomposition reaction mixture of sodium nitrite and copper sulfate resulted in a gradual change in color and the color intensity of the reaction mixture also, which was monitored spectrophotometrically.

3.1. Wavelength scanning of copper sulphate and sodium nitrite solution

Preliminary spectrophotometric scans of Figure 1 produced a narrow and low absorption band of Cu(II) at 530 nm in addition to the characteristic broad band at greater than 600 nm. The 530 nm band was diminished after treatment with an equimolar concentration of acidic sodium nitrite (Figure 1 inset) with a concomitant generation of new peaks at 515 and 580 nm and a reduction of the broad band. Sodium nitrite and the garlic extracts have no peak around 530 nm. Employing the technique of difference absorption spectroscopy, there was regeneration of the 530 nm peak with the addition of the garlic extracts to the decomposition mixture. The generation of peak at 530 nm was therefore used as a diagnostic probe for the titration of ligands in the garlic extracts against the decomposition mixture by the mole ratio and continuous variation methods [9].

3.2. Titration by the mole ratio method

The absorption of the products of the decomposition reaction at 515 and 580 nm, and not at 530 nm, strongly supports the observation that the restoration of the peak at 530 nm upon addition of the garlic extracts was due to copper complexation with the ligands in the extracts [14]. Moreover, the regeneration of the peak at 530 nm was accompanied by a change in color from a deep green to different shades of green, depending on the type of garlic extract, and not to the characteristic pale blue color of Cu(II) sulfate. Absorption within the 500 – 700 nm wavelength range by copper complexes has been attributed to d-d electronic transition effects [15]. The resultant titration plots were sigmoidal (and not straight lines) with minimum, maximum, and inflection points, as shown in Figures 3 and 4, are typical of a stepwise metal-ligand reaction. The sigmoidal nature of Figures 3 and 4 are also similar to the copper-alanine complexation plot shown in Figure 2, which was replicated in this study for comparison [10]. The occurrence of the inflection points with distinct concavities is indicative of the differences in the stability of the complexes formed [15].

3.3. Titration by the continuous variation method

To verify the metal-ligand complexation nature of the reactions of Figures 3 and 4, the borate extracts (bo, bo-u and bo-s), were further titrated against the decomposition mixture in a continuous variation mode as shown in Figure 5 [11]. Again, titrations were monitored at same wavelength of 530 nm. In Figure 5, the maximum and minimum points occurred

© Cognizure. All rights reserved.

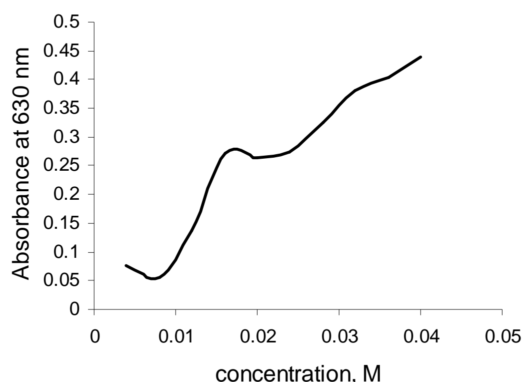

Figure 2. Spectral pattern showing equilibrium points of the stepwise formation of copper-alanine complexation. Titrants (0.5 mL) of alanine were stirred in equal volume of copper phosphate suspension for 5 min. The absorbance of the copper-alanine complexation was monitored at 630 nm.

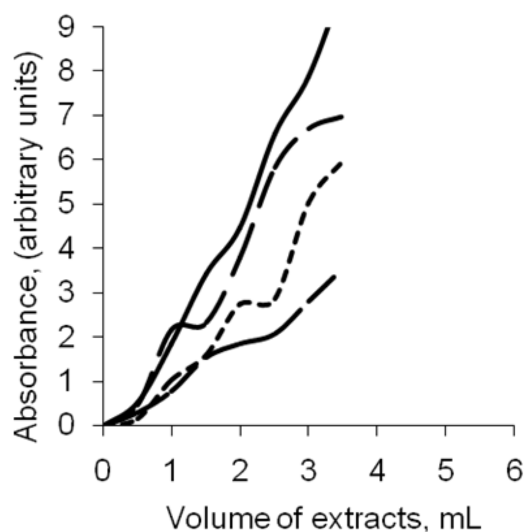

Figure 3. Spectral patterns of the copper complexation reactions using extracts obtained from Alata garlic. Extract in 0.1 M HCl (———, Ala-HCl) extract in borate buffer (— —, Ala-bo) extract in borate buffer with 6 M urea (▪▪▪▪▪▪, Ala-bo-u), extract in 10% sodium dodecyl sulfate (— · —, Ala-bo-s)
Note: Absorbance units have been equally weighted to allow spacing of plots.

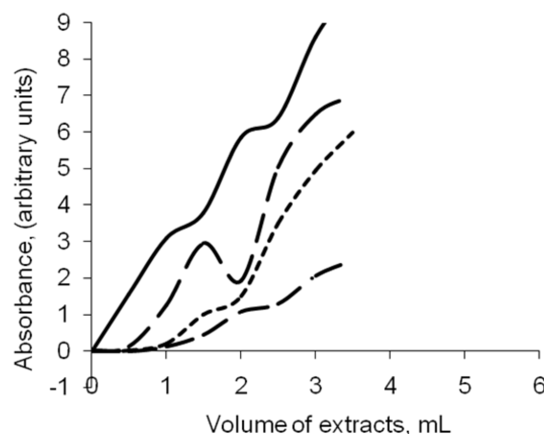

Figure 4. Spectral patterns of the copper complexation reactions using extracts obtained from Chinese garlic. Extract in 0.1 M HCl (———, Chn-HCl), extract in borate buffer (— —, Chn-bo), extract in borate buffer with 6 M urea (▪▪▪▪▪▪, Chn-bo-u), extract in borate buffer with 10% of sodium dodecyl sulfate (— · —, Chn-bo-s).

at between a total of 2.5 to 3 mL of titrants of garlic extract, similar to the highest value of inflection point of 2.75 mL as shown in Table 2. This value corresponds to the volume of titrant required to produce the most dominant complex product of Figures 3 and 4. The continuous variation plots of Figure 5 encompassed all the inflection points of their respective mole ratio plots of Figures 3 or 4. Thus one part each of the 0.1 M $CuSO_4$:0.1 M $NaNO_2$ mixture and the 2.75 ml of garlic extract were enough to obtain all complex products capable by the reaction.

3.4. Protein concentration of garlic extracts by the biuret method

The absorption pattern of SDS extracts in Figure 5 was a deviation from the other extracts but consistent for the two garlic varieties. This deviation was not observed under the mole ratio titration method though the SDS extracts recorded some of the lowest absorbance values in mole ratio titrations. This could be due to SDS competition with copper ions for protein binding sites. Consequently, the effect was more severe at low concentration of the decomposition mixture than at higher concentration as shown in Figure 5. This observation and the increase in absorbance at 530 nm prompted the determination of protein content of the garlic extracts by the biuret method. The method is based on binding of reduced copper to peptide bonds in alkaline medium with absorption at 540 nm which can also be disrupted by SDS monomers at concentration below the CMC. The high acidic content of the HCl-extracts was not conducive for the biuret protein determination and therefore were not included in the biuret and the continuous variation verification methods. As shown in Table 1, the borate-SDS (bo-s) extracts recorded the lowest protein concentration, a confirmation of the induction of copper complexation of the components in the garlic extracts.

3.5. Proposed complexation pattern

The regeneration of peaks, the reduction of absorbance of the SDS extracts of Figures 3, 4 and 5 and the reduction in protein concentration of the SDS extracts in Table 1 could all be observed in the d-d electronic transmission region of copper. It can be deduced that there was a change in the coordination sphere of the copper center due to the decomposition reaction and a subsequent reduction of Cu(II) to Cu(I) as consequence of the oxidation of NO_2^- to NO_3^- leading to the diminished peak at 530 nm and generation of new peaks at 515 nm and 580 nm as shown in the equations (i) and (ii) below:

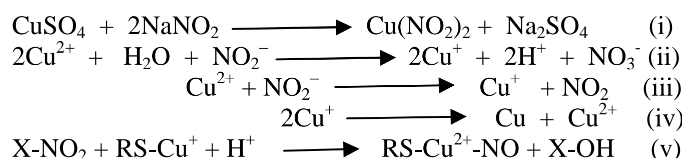

$$CuSO_4 + 2NaNO_2 \longrightarrow Cu(NO_2)_2 + Na_2SO_4 \quad (i)$$
$$2Cu^{2+} + H_2O + NO_2^- \longrightarrow 2Cu^+ + 2H^+ + NO_3^- \quad (ii)$$
$$Cu^{2+} + NO_2^- \longrightarrow Cu^+ + NO_2 \quad (iii)$$
$$2Cu^+ \longrightarrow Cu + Cu^{2+} \quad (iv)$$
$$X\text{-}NO_2 + RS\text{-}Cu^+ + H^+ \longrightarrow RS\text{-}Cu^{2+}\text{-}NO + X\text{-}OH \quad (v)$$

© Cognizure. All rights reserved.

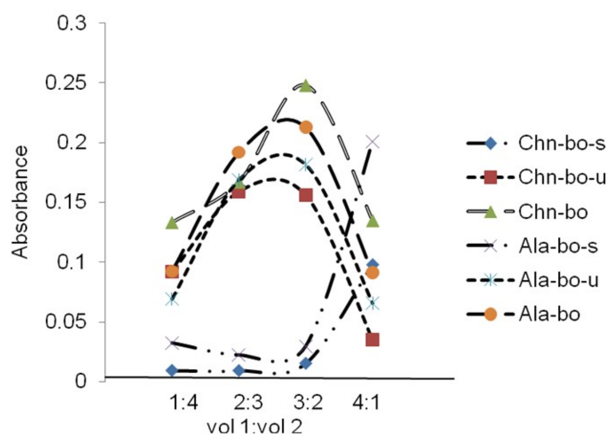

Figure 5. Spectral patterns of garlic extract titration against the decomposition reaction mixture. The total volume (vol 1 + vol 2) of the decomposition reaction mixture (vol 1) and garlic extract (vol 2) in a reaction was held constant but their fractional volumes (vol 1:vol 2) were varied.

Table 1. Percentage protein composition of garlic extracts.

	Alata garlic % protein	Chinese garlic % protein
Borate buffer extract	48.5	35.3
Urea-borate buffer extract	43.3	10.5
SDS-borate buffer extract	7.5	2.5

Alternatively, the NO_2^- ion could also be oxidized to nitrogen dioxide of equation (iii). Since Cu^+ is a stronger reducing agent than Cu^{2+} it would be more reactive towards the stabilizing ligands of the garlic extracts. However, Cu^+ complex would quickly disproportionate as shown in equation (iv) to the more stable Cu^{2+} complex hence the gradual regeneration of the 530 nm peak and the associated color changes which was dependent on the nature of extract. Thus the decomposition mixture is a complete redox reaction of the form: Cu^{2+}/Cu^{1+} // NO_2^- /NO_3^- (or NO_2). The stabilizing ligands, proteins and peptides in the extracts could give a reaction reminiscent of the binding of biuret to peptide bonds with absorption at 540 nm [8]. The 10 nm blue shift observed in this study could be due to the differences in the copper complexing media. In addition, the complex reaction of NO_2^- ions could lead to nitrosation of organosulfur compounds (sulphydryl and sulphides, (v)) in the garlic extract which are better stabilized by Cu(II) than Cu(I) ions at the near-neutral pH condition ($5 < pH < 7$) of the garlic-decomposition mixture reaction to give absorption at 530 nm [16].

3.6. Similarity analysis of the inflection points of titration plots

The differences of the proposed two core groups of copper coordination products of unique absorption at 530 nm could be the major cause of the differences in inflection points in Figure 3 and 4. This necessitated a similarity search to determine the pairs of extracts with complex product(s) that could be the true representative(s) of the two varieties for products formed from the decomposition mixture and garlic extracts. The expected ideal situation should be a unique visible light absorbing chemical product that can be easily formed *in situ* of most commonly aqueous-based extracts of the two cultivated varieties. Such a product can be readily adapted to simple microtiter plate formats that require inexpensive and widely available instrumentation for high-throughput analysis of extracts from that species. On the other hand any nutritional, medicinal and industrial relevance of such a product would boost the cultivation of the two varieties. In order to compare the visible evidence of the titrations, the inflection points of the mole ratio plots of Figures 3 and 4 were determined by first derivative method and manipulated by the Jaccard's similarity method. An inflection point in this study is the volume of titrant (volume of extract) in milliliters at which the stochiometric quantities of metal and ligand is reached was adapted from the mole ratio method of metal-ligand titration. After this point the absorbance levels off when the metal (or the ligand) is not in excess until a new complex begins to form as observed in Figures 2, 3, and 4. In Figures 3, 4 and 5 the metal is presented as the decomposition mixture that generated the Cu^{2+}/Cu^{1+} // NO_2^- /NO_3^- (or NO_2) redox mixture and the ligand is derived from the crude garlic extract. The concentrations of the 'two reactants' were unknown but the titration plots showed a complete compliance to the Job's continuous variation and the mole ratio patterns of metal-ligand complexation.

From Table 2, 8 inflection points were extracted from each of Figures 3 and 4 by first derivative method but the 16 points are represented by only five values of inflection points: 0.75, 1.25, 1.75, 2. 25, 2.75 mL. This implies that within extracts of the same or different variety, some values of inflection points were scored more than ones and others were not scored. The inflection point values can also be transformed as multiple of 0.5 giving constant increments of 1.5, 2.5, 3.5, 4.5 and 5.5 respectively. This shows that complexes obtained may be of the same unique copper (M) to ligand(L) composition such as $M_{1.5}L_{1.5}$, $M_{2.5}L_{2.5}$, $M_{3.5}L_{3.5}$, $M_{4.5}L_{4.5}$, $M_{5.5}L_{5.5}$. Such composition will give copper to ligand ratio of 1:1 corresponding to copper or ligand 'mole' ratio in a complex of 0.5. The observed pattern may be as a result of the selectivity of the mode of complexation to the type of garlic and the extractive ligands involved [17].

Each value of the inflection point was recorded in Table 2 as being present (1) or absent (0) for each of the plots (extracts) in Figures 3 and 4. 6 out of the 8 extracts gave 2 inflection points each and two extracts Ala-bo-s and Ala-bo-u gave 1 and 3 inflection points respectively. Thus, the presence (1) or absence (0) of an inflection point in Table 2 for any of the decomposition mixture – garlic extract reaction is supportive of the variability of the visible evidence of Figures 3 and 4. The scores of Table 2 for each of the 8 extracts (N = 8) were executed in a series N by N using the Jaccard's similarity relation. The resulting similarity matrix (Table 3) gave the numerical representation of how similar a pair of extracts are in terms of inflection points: 1= highest similarity and 0 = no similarity. Pairs of extract with similarity index 1 are more likely to have similar complex product(s) than pairs with less than 1 or zero similarity indices. Two categories of pairs of extracts can be identified in Table 3:

© Cognizure. All rights reserved.

Table 2. Inflection points (IP) as titer values (mL) corresponding to maximum absorption at 530 nm. Titer values were obtained from the absorbance plots (Figures 3 and 4). Values were scored for each extract depending on their presence (1) or absence (0).

IP mL	Ala-HCl	Ala-bo	Ala-bo-u	Ala-bo-s	Chn-HCl	Chn-bo	Chn-bo-u	Chn-bo-s
0.75	0	1	1	0	1	1	0	0
1.25	1	0	0	1	0	0	1	0
1.75	0	0	1	0	0	0	0	1
2.25	1	1	0	0	0	1	1	0
2.75	0	0	1	0	1	0	0	1

Table 3. Jaccard's similarity index of copper-garlic ligand complex. Indices were compiled for the crude extracts (N) from the Alata and Chinese garlic varieties based on Table 2.

N	Ala-HCl	Ala-bo	Ala-bo-u	Ala-bo-s	Chn-HCl	Chn-bo	Chn-bo-u	Chn-bo-s
Ala-HCl								
Ala-bo	0.33							
Ala-bo-u	0.00	0.33						
Ala-bo-s	0.33	0.00	0.00					
Chn-HCl	0.00	0.33	0.66	0.00				
Chn-bo	0.33	1.00	0.25	0.00	0.33			
Chn-bo-u	1.00	0.33	0.00	0.50	0.00	0.33		
Chn-bo-s	0.00	0.00	0.50	0.00	0.33	0.00	0.00	

a) 16 pairs of extracts of different garlic variety (non bolded area). 9 out of the 16 pairs scored indices in the range of 0.25 to 1 and 7 pairs scored zero. The pairs that gave similarity index of between 0.5 and 1.0 whose products would be of greatest interest to search for the representative complex product(s) of the two varieties were: Ala-bo/Chn- bo (1), Ala-HCl/Chn-bo-u (1), Chn-HCl/Ala-bo- u (0.66), Ala-bo-u/Chn-bo-s (0.5), and Ala-bo-s/Chn-bo-u (0.5). The rest of pairs in this category scored similarity coefficients of 0.25 and 0.33 as shown in Table 3 and are less likely to contain common complex products.

b) 12 pairs of extracts of the same variety (bolded areas): 6 pairs out of the 12 scored similarity index of 0.33 each and 6 pairs scored zero. The two bolded areas gave similar pattern of indices indicating no intra-experimental variability. This was expected of cultivars of same species as a result of a unique chemical reaction between their extractive ligands and the copper redox solution.

4. Conclusions

Spectrophotometric evidence has been provided in this study that validates the use of a redox system derived from equimolar mixture of sodium nitrite and copper sulfate for crude preparations of copper complexes in garlic extracts. The reaction can be carried out at room temperature and different extractant conditions such as pH and additives. The proposed complexation pattern could involve organosurphur compounds, proteins and peptides in garlic extracts as ligands of the complexation. There was an average of two inflection points per titration plot and only five values of inflection points which were multiples of 0.5 from the total of eight titration curves. These findings are suggestive of a reaction that gave unique products or groups of products of constant order (1.5, 2.5, 3.5, 4.5 and 5.5) of structural composition. For the two garlic varieties Alata and Chinese, pairs of extracts have been identified through the Jaccard Similarity Relation that are likely to contain common representative complex product(s) of the two varieties. Such complex products could be tested for their functional properties or serve as molecular entities for the development of customized colorimetric screening protocol for rapid identification of the two varieties of garlic and their products.

Acknowledgement

The authors are thankful to the Department of Biochemistry and Biotechnology, Kwame Nkrumah University of Science and Technology for providing garlic samples, chemicals, equipment, and laboratory space.

References

1. M. B Francis, T. F Jamison, E. N. Jacobsen, Curr. Opin. Chem. Biol. 2 (1998) 422.
2. F. M. A. M. Aqra, Transition Met. Chem. 29 (2004) 921.
3. P. Laokul, S. Maensiri, J. Optoelectron. Adv. Mater. 11 (2009) 857.
4. T.Bahorun, V. S. Neeraheen, O. I. Anuoma, Afr. J. Biotechnol. 4 (2005) 1530.
5. R. D. Hancock, A. E.Martell, Chem. Rev. 89 (1989) 1874.
6. R. Kuma, R. Singh, Russ. J. Coord. Chem. 32 (2000) 192.
7. N. S. Bryan, Free Radical Biol. Med. 41 (2006) 691.
8. A. G. Gornal, C. J. Baldawil, M. M. David, J. Biol. Chem. 177 (1949) 751.
9. K. Sharma, I.Singh, Food Anal. Methods 2 (2009) 311.
10. H. Amagase, B. L. Petesch, H. Mastuura, S. Kasuga, Y. Itakwa, J. Nutr. 131 (2001) 955.
11. A. Job, Ann. Chim. Phys. 9 (1928) 113.
12. P. Jaccard, Bull. Soc. Vandoise Sci. Nat. 33 (1901) 547.
13. K. M. Wellman, B. K. Wong, PNAS 69 (1989) 824.
14. Y. Yaci, S. Denizligil, N. Bicak, T. Atay, Angew. Makromol. Chem. 195 (1992) 89.
15. A. N. Wijewickreme, D. D. Kitts, T. D. Durance, J. Agric. Food. Chem. 45 (1997) 4577.
16. S. C.Askew, D. J. Barnett, J. Mcaninly, D. L. H. William., J. Chem. Soc. 2 (1995) 741.

© Cognizure. All rights reserved.

17. G. R. Zhao, Z. J. Xian., J. X. Ye, Y. J. Yuan, Z. X. Guo, Food Chem. 99 (2006) 767.

Cite this article as:

Nicholas Sarpong Sarfo *et al.*: **Visible evidence for the formation of copper complexes in garlic extracts treated with copper sulfate and sodium nitrite mixture.** ScienceJet 2012, **1**: 7

© Cognizure. All rights reserved.

Compact charge model for ultra-thin nanoscale Double Gate MOSFETs

M. A. Abdi[a], F. Djeffal[a,b,*], T. Bendib[b], M. Chahdi[a] , A. Benhaya[b]

[a] *LEPCM, University of Batna, Batna, Algeria*
[b] *LEA, Department of Electronics, University of Batna, Batna, Algeria*

[*] *Author for correspondence: F. Djeffal, email: faycaldzdz@hotmail.com*
djeffaldzdz@yahoo.fr
Received 4 Feb 2012; Accepted 27 Mar 2012; Available Online 19 Apr 2012

Abstract

In this paper, a new approach to investigate the inversion charge behavior in ultra-thin nanoscale Double Gate MOSFETs by using the Gradual Channel Approximation (GCA) and Genetic algorithm (GA) optimization technique is presented. Our proposed analytical approach combines the universal optimization and fitting capability of GA and the cost-effective optimization concept of quantum correction, to achieve accurate and simple compact models for nanoscale circuits design. The obtained results showed that the predictions of the quantum capacitance, threshold voltage shift and quantum inversion charge density are in close agreement with the 2-D numerical simulations. The developed models can also be implemented into circuits simulators to study the nanoscale CMOS-based devices without impact on the computational time and data storage.

Keywords: Nanoscale; DG MOSFET; Genetic algorithm; Modeling

1. Introduction

As the MOSFET gate length enters nanoscale field, short channel effects such as threshold voltage roll-off and subthreshold swing become increasingly significant, which limit the scaling capability of MOSFET devices [1, 2]. To overcome these limitations and realize high-performance transistors, a new transistor called Double Gate (DG) MOSFET (Figure 1) has been proposed as potential candidate for lower CMOS-based circuits design [1, 2]. This is mainly due to the superior control of short channel effects (SCEs) because of the reduced influence of the drain voltage on the inversion channel charge behavior. To extract information accurately about the charge inversion profile requires the solution of the coupled Schrödinger - Poisson equations based on the non-equilibrium Green's function (NEGF) formalism, assuming quantum effects are to be fully accounted [3]. But from the nanoscale CMOS circuits design point of view even 2-D solution of numerical NEGF is an overkill approach in term of both computational cost and complexity [3]. However, for circuits simulations high computational speed is necessary if the model is to be implemented in circuits simulators (PSPICE, CADENCE). Therefore, accurate analytical models are required to study and simulate the nanoscale devices.

For analytical devices modeling, the Gradual Channel Approximation (GCA) model is widely used for analytical semiconductor device modeling. This model, based on first two moments of Boltzman transport equation (BTE), is simple with powerful methods for devices simulation. On the other hand, it is well known that GCA model is not accurate enough for simulation of deep-submicrometer devices in which, rapid changes and confinement of eclectic field, and non-local effects such as velocity overshoot and quantum effects are pronounced [4-6]. Recently, several papers have been published to model the nanoscale DG MOSFET [7-10]. However, in these publications, simple and accurate closed expressions for quantum capacitance, inversion charge were not provided, thus limiting the models use by designers.

In this work, we present an efficient and systematic techniques for nanoscale DG MOSFETs modeling, where simple and accurate device models can be automatically achieved from a computational process to maximally reduce human trial and error efforts. In addition, the models should be formulated such that it can be conveniently incorporated into existing circuit simulators for high-level circuit simulation and yield design. Unlike the numerical models used to study the nanoscale structure, such as 2-D numerical Non-Equilibrium Green's Function (NEGF) formalism, which is complicated and requires a high computation time and storage memory, the

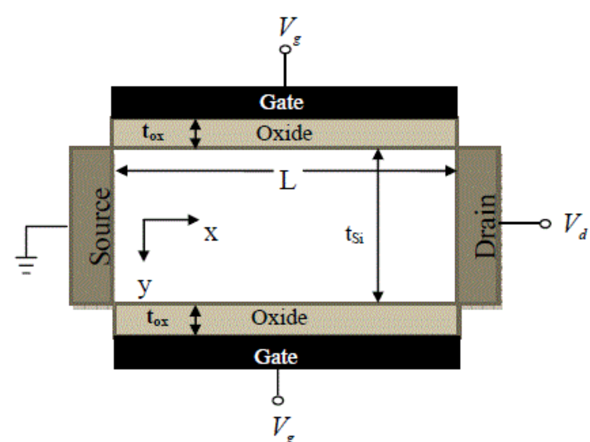

Figure 1. Schematic sketch of symmetrical DG MOSFET structure investigated in this study with (channel doping N_A =10^{16} cm^{-3}, t_{si} represents silicon thickness and t_{ox} is the oxide thickness).

© Cognizure. All rights reserved.

proposed approach has lower complexity and lower simulation time.

2. Modeling methodology

Recently, Artificial Intelligence (AI) techniques have been recognized as an important approach for the semiconductor devices computer-aided design area in addressing the growing challenges of designing next generation of nanoelectronic devices, circuits, and systems [3,9]. The AI-based methods represent important steps towards automating the device modeling process. However, because the genetic algorithms have to learn the device behavior from numerical or experimental databases without using existing device physical models like: drift-diffusion (D-D), hydrodynamic and gradual-channel approximation (HGCA), which makes the reliability of the AI-based model low and questionable. In GA, variables of a problem are represented as genes in a chromosome, and the chromosomes (population) are evaluated according to their fitness values. Given a random initial population GA operates in cycles called generations. The problem to be solved is defined in terms of an evaluation function (fitness function), which is used to evaluate the chromosomes. A chromosome evaluated as having a high fitness value is likely to be a good solution of the problem.

Implementation of GA requires determination of six fundamental issues: chromosome representation, selection function, the genetic operators, initialization, and evaluation function [11, 12].

Based on the efficiency proven by NEGF for the modeling of nanoscale DG MOSFETs and the difficulty imposed at the moment by the constraints of the nanotechnology (sub-50 nm) to form an experimental database [3,9], we have used the NEGF formalism as accurate model.

The Gradual Channel Approximation (GCA), which assumes that the quasi Fermi potential stays constant along the direction perpendicular to the channel, is used in our study as approximate model. Accurate models for long channel double-gate MOSFETs [10,13-15] have been recently developed using the conventional approaches, showing good agreement with 2-D numerical simulations. The inclusion of short-channel effects (SCEs) in undoped multiple gate MOS models, using physical equations and without decreasing the order of continuity of the devices, is still a modeling challenge.

2.1. Inversion charge modeling

Breaking away from the premise of the GCA means that one needs to solve the Poisson equation given by

$$\Delta\phi(x,y) = \frac{qn_i}{\varepsilon_{si}} e^{(\phi(x,y)-\phi_F)/V_{th}} \tag{1}$$

where q is the electron charge, n_i is the silicon intrinsic concentration, ε_{si} is the silicon permittivity, V_{th} is the thermal voltage, $\phi(x,y)$ represents the 2-D electrostatic potential distribution in the channel region, and ϕ_F is the non-equilibrium quasi-Fermi level referenced to the Fermi level in the source, satisfying the following boundary conditions

$$\phi_F(0,y) = 0 \tag{2a}$$

$$\phi_F(L,y) = V_{ds} \tag{2b}$$

V_{ds} being the drain voltage. ϕ_F can be approximated by a second order polynomial function, using [16], as

$$\phi_F(x) = \frac{V_{ds}}{L^2} x^2 \tag{3}$$

In our approach, Genetic Algorithm (GA) generates the optimal and corrected distribution of these parameters, which are inserted in the approximate model (GCA) to produce simulation results close to the accurate model (NEGF). The proposed GA-based approach algorithm is given as,

Step1: Solving GC approximate model (3).
Step2: Classical inversion charge model (5).
Step3: Corrected oxide capacitance model (6a).
Step4: Corrected threshold voltage model (6b and 6c).
Step5: Corrected inversion charge model (6) in (5).
Step6: Optimization of corrected inversion charge model using Gas.
Step7: Stopping criterion (4). If no we have reproduction of Gas operators and return to step 3 else pass to step 8.
Step8: Quantum inversion charge model (7).

These electrical parameters distributions have been used for training and optimisation of GA to generate optimise and accurate analytical model to study the nanoscale DG MOSFETs. In the present study, a mean squared error of each parameter, Par, the j_{th} generation is taken as the fitness function,

$$f = \frac{1}{M}\sum_{V_{ds}}\sum_{V_{gs}}\sum_{T_{si}}\sum_{T_{ox}}\sum_{L}\left[\frac{Par_{NUM} - Par_{GA-ANA}}{Par_{NUM}}\right]^2 \tag{4}$$

where f is the fitness value; Par_{GA-ANA} is the predicted parameter based on GA and analytical computations; Par_{NUM} represents the target function (numerical results based on 2-D numerical, NEGF, simulation); and M represents the number of samples (database size). It is aimed to minimize this fitness function, for each parameter, in order to develop accurate simple compact drain current model for nanoscale DG MOSFETs.

Taur in [17], has introduced a long channel model for the inversion charge of undoped DG MOSFET devices based on a 1-D analytical solution of Poisson equation incorporating only the mobile charge term as,

$$Q_i = C_{ox}\left[-2C_{ox}\frac{V_{th}^2}{Q_0} + \sqrt{\left(2C_{ox}\frac{V_{th}^2}{Q_0}\right)^2 + 4V_{th}^2 \ln\left(1 + e^{\frac{V_{gs}-V_{fb}-\phi_F+V_T}{2V_{th}}}\right)}\right] \tag{5}$$

where $C_{ox} = \varepsilon_{ox}/t_{ox}$ represents the oxide capacitance per unit area, V_{fb} is the flat band voltage, V_T is the threshold voltage, and Q_0 is the charge coefficient given [17] by $Q_0 = (8V_{th}\varepsilon_{si}/t_{si})$.

For silicon films thinner than 5 nm, quantum confinement should be considered; it leads to a reduction of the channel charge density and an increase of the threshold voltage.

© Cognizure. All rights reserved.

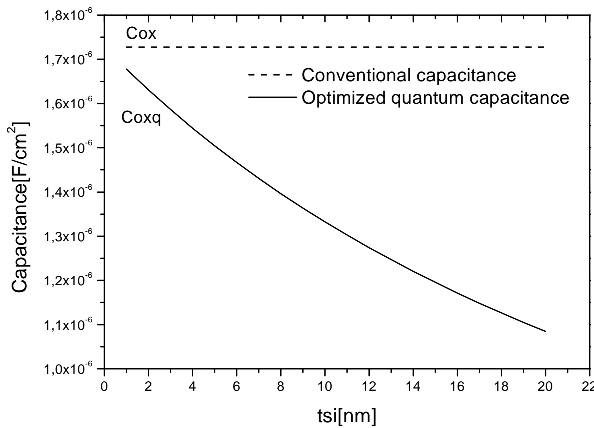

Figure 2. Classical and optimized quantum oxide capacitance versus film thickness.

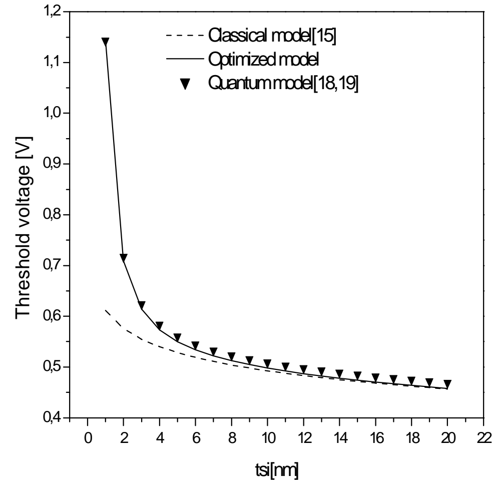

Figure 3. Classical and quantum threshold voltage versus film thickness.

From (5), we can see that an accurate model of the inversion charge depends mainly on the oxide capacitance and threshold voltage. Therefore, in order to develop an accurate charge model, new oxide capacitance and threshold voltage models, which include the quantum effects, should be introduced in (5). Figure 2 shows the variation of the quantum oxide capacitance, C_{oxq}, as function of channel thickness. This capacitance can be defined as the series combination of the C_{ox} and the inversion capacitance per unit area, and it is given by the following approximated expression:

$$C_{oxq} = \frac{C_{ox}}{1+\xi_1 C_{ox} T_{si}} \tag{6a}$$

Figure 3 shows the variation of the quantum threshold voltage, V_{Tq}, as function of channel thickness. This variation can be given as,

$$V_{Tq} = V_T + \delta V_{Tq} \tag{6b}$$

With δV_{Tq} represents the threshold voltage shift due to the quantum effects and it is given by,

$$\delta V_{Tq} = \frac{\xi_2}{T_{si}^2} \tag{6c}$$

Where ξ_1 and ξ_2 are fitting parameters.

Now, substituting the quantum oxide capacitance, C_{oxq}, (6a) and the quantum threshold voltage, V_{Tq}, (6b) into (5), a new inversion charge model can be given as,

$$Q_{iq} = C_{oxq}\left[-2C_{oxq}\frac{V_{th}^2}{Q_0} + \sqrt{\left(2C_{oxq}\frac{V_{th}^2}{Q_0}\right)^2 + 4V_{th}^2 \ln\left(1+e^{\frac{V_{gs}-V_{fb}-\phi_F+V_T+\delta V_{Tq}}{2V_{th}}}\right)}\right] \tag{7}$$

The fitting parameters (ξ_1 and ξ_2) in (7) can be extracted using (4).

3. Results and Discussion

For the purpose of GA-based optimization of (7), routines and programs for GA computation were developed using MATLAB 6.5 and all simulations are carried out on a Pentium IV, 3 GHz, 1 GB RAM computer. For the implementation of the GA, tournament selection is employed which selects each parent by choosing individuals at random, and then choosing the best individual out of that set to be a parent. Scattered crossover creates a random binary vector. It then selects the genes where the vector is unity from the first parent, and the genes where the vector is zero from the second parent, and combines the genes to form the child. An optimization process was performed for 20 population size and maximum number of generations equal to 100, for which stabilization of the fitness function was obtained. The obtained results of the proposed approach are presented for the studied device in two-dimension. The transistor length is 20 nm with 20 mesh points and its thickness is 5 nm with 5 mesh points. Therefore, simulation data are 2D matrices of 20×5. The quantum simulations, self-consistent computations, have been carried out using 2D Silvaco and nanoMOS2.5 numerical simulators tools [18,19].

Figure 4 shows the inversion charge density versus the gate-source voltage for nanoscale undoped DG MOSFET. The increase and the shift of the inversion charge density due to the QM effect are well predicted by our model, given in (7). For below threshold voltage and in the subthreshold regime, quantum and classical inversion charge densities are close to each other. However, for a high gate-source voltage, the electrons are strongly confined in the direction perpendicular to the Si-SiO_2 interface due to the increasing influence of the vertical electric field component. In Figure 5, an excellent accord was found between our inversion charge model and the numerical Poisson-Schrödinger self-consistent (NEGF) simulation.

In our approach, the developed model is an accurate simple analytical closed expression with 2 global optimized fitting parameters (ξ_1=1.72×$10^{11}$and ξ_2=5.32×10^{-15}). Therefore, the proposed model can be easily used by circuit simulation programs such as PSPICE for more accurate predictions of nanoscale DG MOSFET characteristics.

© Cognizure. All rights reserved.

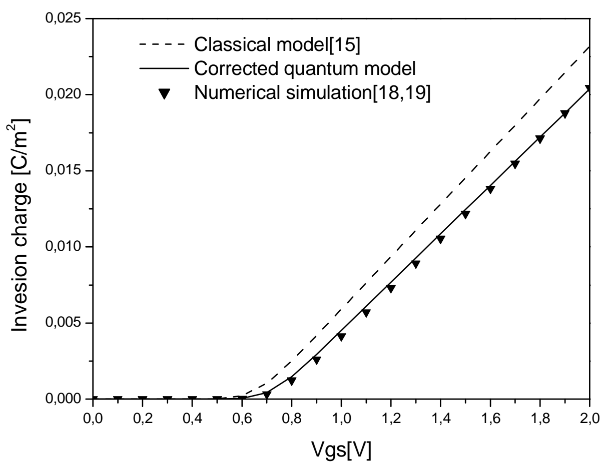

Figure 4. Classical and corrected quantum inversion charge versus gate-source voltage.

4. Conclusions

In this paper, a new analytical inversion charge model including quatum confinement effects for undoped ultra thin nanoscale DG MOSFETs has been developed. The 2-D self-consistent numerical computation and Gradual Channel Approximation are used as accurate and approximate models, respectively. With mapped parameters between accurate model and approximate one, the GCA model is capable of producing results of the accurate 2-D numerical simulation. The presented analytical inversion charge model overcomes problems using classical models. The proposed model has several advantages such as accuracy, simplicity and applicability for wide device dimensions range. The encouraging obtained results have indicated that the proposed closed analytical form is particularly suitable to be introduced in electronic devices simulators to study and investigate the nanoscale CMOS-based circuits.

Acknowledgment

This work was supported by Microsoft, and administered by TWAS, the academy of sciences for the developing world and AAS, the African Academy of Sciences.

References

1. The International Technology Roadmap for Semiconductors (2007). Available at: http//public.itrs.net.
2. F. Djeffal, Z. Ghoggali, Z. Dibi, N. Lakhdar, Microelectron. Reliab. 49 (2009) 337.
3. F. Djeffal, M. Chahdi, A. Benhaya, M.L. Hafane, Solid-State Electron. 51 (2007) 48.
4. F. Stern, Self-consistent results for n-type Si inversion layers, Phys. Rev. B. 5 (1972) 4891.
5. G. Baccarani, S. Reggiani, IEEE Trans. Electron Devices 46 (1999) 1656.
6. Qiang Chen, and James D Meindl, Nanotechnology 15 (2004) 8549.
7. J.A. Lopez-Villanueva, P. Cartujo-Cassinello, F. Gamiz, J. Banqueri and A.J. Palma, IEEE Trans. Electron Devices 47 (2000) 141.
8. Juzer Vasi, V. Ramgopal Rao, Solid-State Electron. 53 (2009) 1001.
9. F. Djeffal, M.A. Abdi, Z. Dibi, M.Chahdi and A.Benhaya, Mater. Sci. Eng. B 27 (2007) 1111.
10. M. Reyboz, O. Rozeau, T. Poiroux, P. Martin, J. Jomaah, Solid-State Electron. 50 (2006) 1276.
11. Goldberg DE, Genetic algorithms in search, optimization, and machine learning, Addison-Wesley (1989).
12. Painton L, Campbell J, IEEE Trans. Reliab. 44 (1995) 172.
13. B. Iñiguez,, T. A. Fjeldly, A. Lázaro, F. Danneville, and M. Jamal Deen, IEEE Trans. Electron Devices 53 (2006) 2128.
14. S. Xiong, T. J. King and J. Bokor, IEEE Trans. Electron Devices 52 (2005) 1859.
15. Y. Taur, X. Liang, W. Wang and H. Lu, IEEE Electron Device Lett. 25 (2004) 107.
16. Q. Chen, E. M. Harrell, and J. D. Meindl, IEEE Trans. Electron Devices 50 (2003) 1631.
17. Y. Taur, IEEE Trans. Electron Devices 48 (2001) 2861.
18. ATLAS: 2D Device Simulator, SILVACO International (2008).
19. Z. Ren, R. Venugopal, S. Goasguen, S. Datta, M. Lundstrom, IEEE Trans. Electron Devices 50 (2003) 1914.

Cite this article as:

M. A. Abdi *et al.*: **Compact charge model for ultra-thin nanoscale double gate MOSFETs.** ScienceJet 2012, **1**: 8

© Cognizure. All rights reserved.

Femtosecond study of the interaction of intense femtosecond laser pulse with Kr clusters using Landau damping

N. Boucerredj*, K. Beggas, A. Brichni

Laboratoire des semi-conducteurs, Département de Physique, Faculté des Sciences, Université Badji Mokhtar, B. P. 12, 23000 Annaba, Algérie

Authors for correspondence: N. Boucerredj, email: boucerredj@yahoo.fr

Received 4 Feb 2012; Accepted 27 Apr 2012; Available Online 28 Apr 2012

Abstract

We study the rare gas cluster (Kr and Ne) containing 10^3 to 10^5 atoms per cluster, irradiated by an intense femtosecond laser pulse. The irradiation of these clusters with the intense laser leads to high excitation energy which is the source of the energetic electrons, high ion charge state and fragmentation process. We have used the modified nanoplasma model for the study of different mechanisms of ionization, expansion and explosion of the cluster. In this model, we consider a cluster with radius of few nanometers in a strong linearly polarized laser fields. The dimensions of the cluster are much smaller than the laser wavelength. The model treats all ionization processes, heating, electron emission and expansion process. We study in detail the different parameters of the nanoplasma leading to the final explosion of the cluster with and without Landau damping. We have found that the hydrodynamic pressure increases 10 times of its value when adding the Landau damping term. We have also found ions with energy up to 9 keV.

Keywords: Nanomaterials; Intense laser; Rare gas clusters; Landau damping

1. Introduction

During the last few years, there is an important attention on the investigation of the interaction of clusters with high-intensity laser pulses. The distinction between the average and local density of clusters leads to an important difference between clusters and solids, as well as between clusters and individual atoms when they interact with intense femtosecond laser pulses [1-4]. Several phenomena were observed in the experiments; such as the generation of highly charged ions and electrons [5-8], X-ray emission and fusion reaction in Deuterium clusters [9]; these phenomena are few of the potential applications of these laser cluster interactions [10].

Several models have been developed to explain the experimental features observed in the interaction of high laser intensity with atomic clusters. In our work we have used the nanoplasma model developed firstly by T. Ditmire et al [11], reformulated by M. Belkacem et al [12, 13] and we have modified and adapted the model to our study. The nanoplasma model offers a complete scenario of the interaction taking into account ionization, heating and explosion processes simultaneously. The cluster is treated as spherical nanoplasma where plasmon resonance takes place. In this model, large electron temperatures are reached and highly charged ions are produced at resonance. The properties of the formed nanoplasma are governed by collisional processes involving electrons and multicharged ions during or after the laser pulses [14]. The electron gas exerts a strong hydrodynamic pressure which combined with the coulomb one, leads to the final explosion of the cluster. The goal of our study is to investigate in detail a comparative study of the dynamics of expansion and explosion of the cluster using the standard and the modified nanoplasma model (with the addition of the term of Landau damping).

In this paper, we examine a theoretical study of the interaction of intense femtosecond laser pulse with large Kr_n clusters (n= 3×10^5 atoms) using the nanoplasma model with the inclusion of the term of electron surface collisions in the expression of the electron ion collision frequency. We describe briefly the nanoplasma model and we present some results of this study; finally we draw our conclusion.

2. Nanoplasma model

The nanoplasma model was proposed firstly by T. Ditmire et al [11]. In this model, the cluster is assumed to be a spherical plasma ball and density is assumed to be spatially uniform throughout the cluster expansion. This model predicts that the resonance absorption occurs near the $3n_{crit}$ (where n_{crit} is the critical density); the model assumes that the plasma density and electron temperature are spatially uniform throughout the cluster expansion. In this model, we consider that the cluster has a radius of few nanometers in the electric field of an intense linearly polarized laser fields; the electric field of the laser is given by

$$\vec{E}_{ext}(t) = E_0 \times exp\left(-2\times ln\,2\times\left(\frac{t}{\tau}\right)^2\right)\vec{e}_z \,. \qquad (1)$$

Where τ is the full width at half maximum (FWHM) and E_0 is the amplitude of the laser field.

In the standard model [11], the electrons collide only with the heavy ions, but in our model the electrons collide with the heavy ions and with the surface of the cluster. Therefore, we use the expression of the total electron-ion collision frequency given by

© Cognizure. All rights reserved.

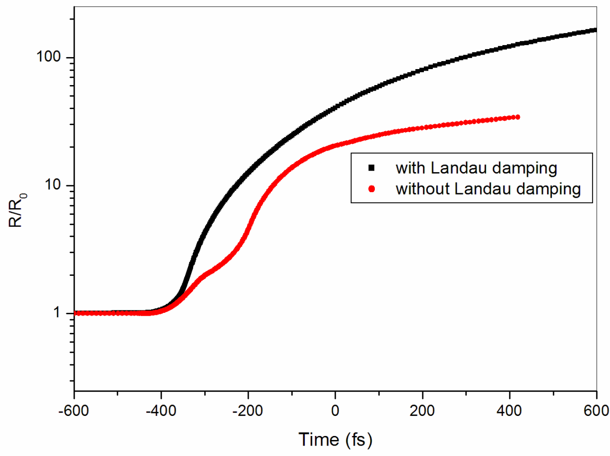

Figure 1. Variation of Kr_n (n=3×10^5 atoms) cluster radius R normalized to the initial cluster radius R_0 as a function of time irradiated with 300 fs, 470 nm laser pulse and peak intensity of 2.5×10^{21} W/m^2(with and without electron surface collisions).

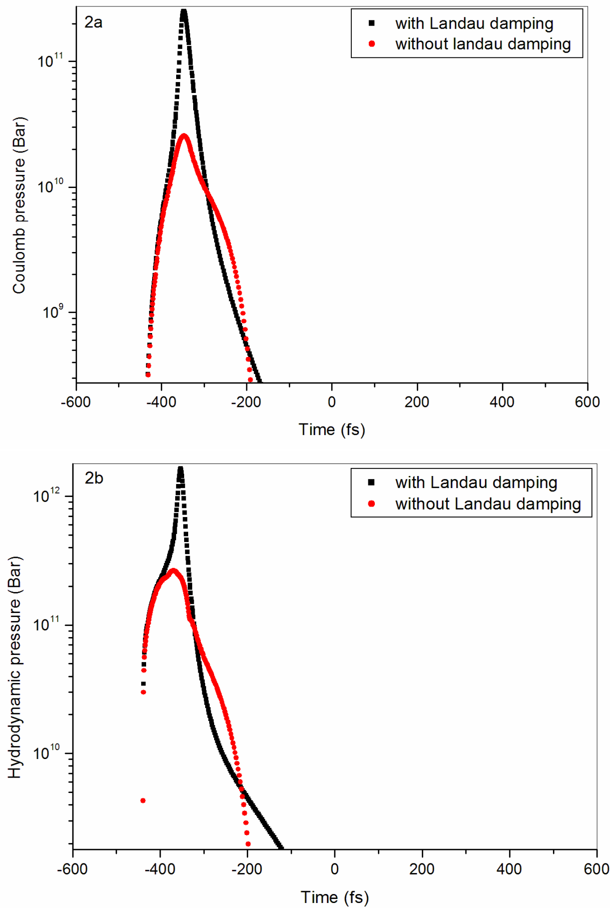

Figure 2. Temporal evolution of the a) coulomb and b) hydrodynamic pressures of Kr_n (n=3×10^5 atoms) cluster with and without electron surface collisions (FWHM= 300 fs, λ=470 nm and I=2.5×10^{21} W/m^2).

$$\nu(w)=\nu_{ei}(w)+\nu_s(w) \quad (2)$$

Where ν_{ei} is the electron ion collision frequency of the standard model of T. Ditmire [11] and ν_s is the electron-surface collision frequency added in our model and given by

$$\upsilon_s=\frac{v}{R} \quad (3)$$

where R is the radius of the cluster and v is the effective electron velocity

$$v=\sqrt{v_{th}^2+v_q^2} \quad (4)$$

With thermal velocity

$$v_{th}=\sqrt{\frac{k_B\times T_e}{m}} \quad (5)$$

Where k_B is the Boltzmann constant, T_e is the electron temperature and m_e is the electron mass.
And quiver velocity of the electron in the field defined as

$$v_q=\frac{e\times E_{int}}{m\times w} \quad (6)$$

Where e is the elementary charge, E_{int} is the internal field and w is the laser pulsation.

The expansion of the cluster is governed by the following equation

$$\frac{d^2R}{dt^2}=5\times\frac{P_t}{n_i\times m_i}\times\frac{1}{R} \quad (7)$$

Here n_i and m_i represent the ion density and mass, respectively and

$$P_t=P_c+P_h \quad (8)$$

Where P_c, P_h are the coulomb and hydrodynamic pressures, respectively and R denotes the nanoplasma radius.

3. Results and Discussion

We consider a Kr_n cluster containing 3×10^5 atoms irradiated by a Gaussian laser pulse with wavelength 470 nm, pulse duration 300 fs, and peak intensity 2.5×10^{21} W/m². The considered ionization mechanisms are direct optical ionization through tunnel ionization and electron-ion collisions. The temporal evolution of the cluster radius normalized to the initial value of the cluster radius is shown in Figure 1. In the beginning, the cluster expands rapidly with Landau damping than without Landau damping, during the pulse when heating of the electrons in the cluster begun; after that, the radius tends to very high values which characterize the final explosion of the cluster. The contributions of the coulomb and hydrodynamic pressures are shown in Figures 2a and 2b. During the majority of the plasma expansion dynamics seen in Figure 1, the dominant pressure is the hydrodynamic pressure with a little contribution from the coulomb pressure. The increase of the total charge of the cluster leads to the increase of the coulomb pressure to 2.63×10^{11} bar (Figure 2a) with Landau damping ten times the maximum value of P_c without Landau damping. However, this value is small compared to the hydrodynamic pressure due to the hot electrons (Figure 2b), P_h≈1.70×10^{12} bar with Landau damping larger than 2.79×10^{11} bar without Landau damping. Those pressures cause a sharp increase in the cluster expansion (Figure 1), then the explosion of the cluster.

© Cognizure. All rights reserved.

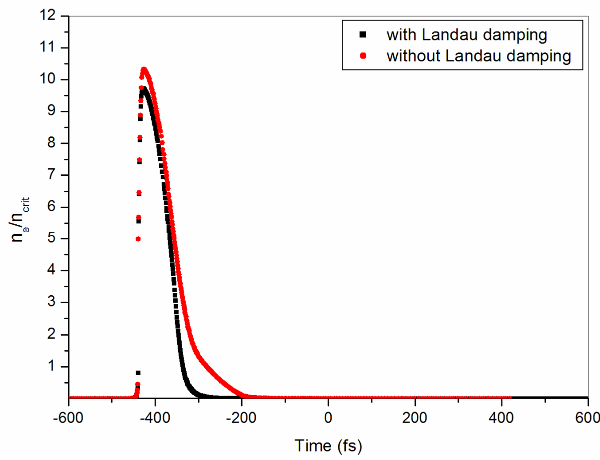

Figure 3. Temporal variation of the electron density normalized to the critical one of Kr_n (n=3×10^5 atoms) cluster with and without electron surface collisions, I= 2.5×10^{21} W/m^2, 300 fs (FWHM) and λ=470 nm.

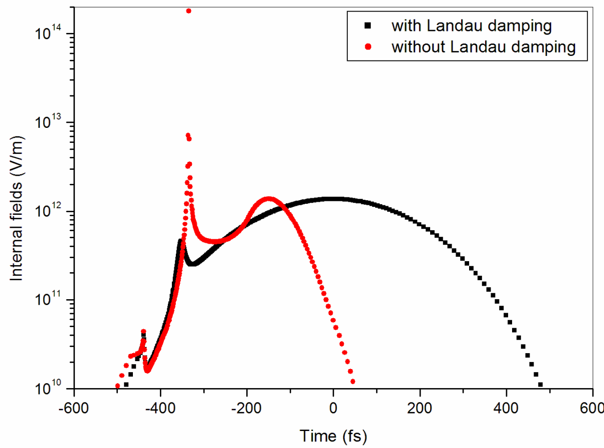

Figure 4. Variation of the internal fields as a function of time for Kr_n cluster (n=3×10^5 atoms, Full width at half maximum (FWHM) =300fs, λ=470 nm and I=2.5×10^{21} W/m^2).

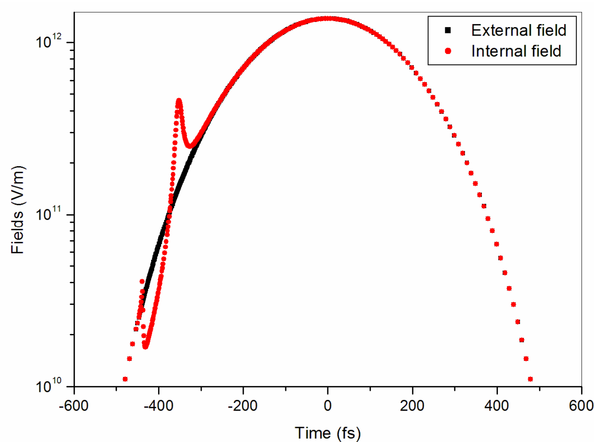

Figure 4a. Temporal evolution of the external and internal fields for Kr_n cluster with Landau damping term (n=3×10^5 atoms, FWHM =300fs, λ=470 nm and I=2.5×10^{21} W/m^2).

We show in Figure 3 the variation of the electron density normalized to the critical one with and without the term of electron-surface collisions as a function of time; by field ionization electrons are produced from the neutral atoms. The formation of nanoplasma occurs, when a sufficiently large number of electrons have been stripped from the atoms by tunnel ionization. When electrons velocities increase, the electrons quickly reach the surface and may be reflected many times during the resonance duration. The field inside the cluster (Figure 4) is shielded for the value of electron densities $n_e > 3n_{crit}$, where n_{crit} (the critical electron density) is given by

$$n_{crit} = \frac{\varepsilon_0 \times m_e \times \omega^2}{e^2}. \tag{9}$$

(where e is the elementary charge, m_e the electron mass, w the laser pulsation and ε_0 is the vacuum dielectric constant), and reaches a maximum when $n_e = 3n_{crit}$. The electron density increases with time and the electrons absorbs energy from the field through collisions. The energetic electrons can then escape from the cluster and the shielding disappears as the electron density n_e drops down to $3n_{crit}$. The electric field is then enhanced and reaches its maximum value, E_{max}= 1.80 ×10^{14} V/m (Figure 4) without the term electron surface collisions, but E_{max}= 4.71 ×10^{11} V/m with this term and we see that the divergence of the electric field disappears when adding the electron-surface collision frequency in the expression of the total electron-ion collision frequency (Eq. 2). For showing the laser pulse profile, we represent in Figure 4a, the variation of the external and internal fields as a function of time with Landau damping term.

When the parent atoms are ionized, the electrons inside the cluster absorb the electromagnetic power, heating up the cluster through which electrons absorb photons when colliding with ions and we have a large ionization rate. During the rising edge of the pulse, electrons are produced from the neutral atoms by field ionization. The rapid increase of the number of quasi free electrons leads the system through a first resonance. The electron density (Figure 3) rises to reach $3n_{crit}$ at time t=-438.59 fs, for both cases (time of the first resonance); at this point more electrons are liberated through tunnel and optical ionization. The combined effect of free streaming of electrons out of the cluster and the hydrodynamic expansion of the cluster is that the electron density starts to fall, after peaking at over $\approx 9n_{crit}$ with electron-surface collisions and $\approx 10n_{crit}$ without this term at the same time. The field inside the cluster again starts to rise as the electron density drops. At t≈-352.59 fs with electron-surface collisions and t≈-333.83 fs without electron-surface collisions, the electron density in the cluster drops to $3n_{crit}$ and we have the second resonance of the internal field (with higher value 4.71×10^{11} V/m and 1.80×10^{14} V/m respectively). The variation of the ion energy with cluster radius is shown in Figure 5. For the case of the standard model, the maximum ion energy is of order of 102.24 eV less than 1.109 keV, with the term electron-surface collisions added in our model, for the same value of the cluster radius 169 A°. After the explosion of the cluster, we have found ions with energy up to 9 keV with the term electron surface collisions added in the expression of the electron ion collision frequency in our model, but 89.2 eV without this term (i.e. standard model). The electron surface collision frequency added here has an important influence on the dynamics of the nanoplasma.

© Cognizure. All rights reserved.

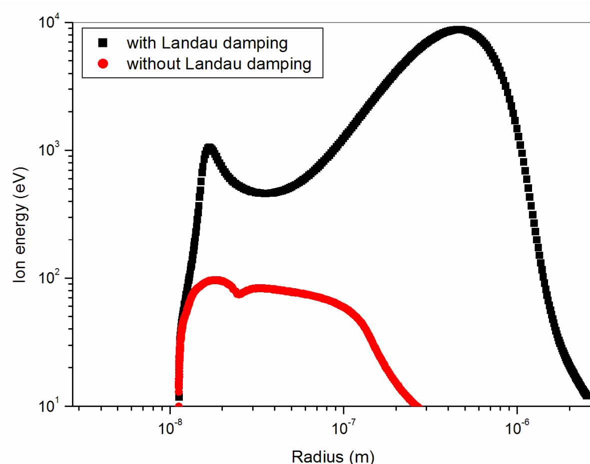

Figure 5. Variation of ion energy as a function of cluster radius for Kr_n (n=3×10^5 atoms) cluster irradiated with 300 fs, 470 nm laser pulse and peak intensity of 2.5×10^{21} W/m^2 (with and without electron surface collisions).

4. Conclusions

The interaction of intense femtosecond laser pulse with large Krypton cluster produced energetic electrons and ions. We have found that the addition of the term electron-surface collisions in our model have an important influence on the dynamics of the nanoplasma. We have found that the expansion of the cluster is rapid with the electron surface collisions term than in the case of the standard model. The coulomb and hydrodynamic pressures are amplified ten times as big as in the standard model. The maximum ion energy is above 9.325 keV with the term electron-surface collisions but 89.20 eV without this term.

References

1. P. G. Reinhart and E. Suraud, Introduction to cluster dynamics, Wiley-VCH Verlag, Weinheim (2004).
2. K. Nishihara, H. Hamitani, M. Murakami et al, Nucl. Instrum. Meth. A. 464 (2001) 98.
3. A. Heidenreich, I. Last and J. Jortner, Eur. Phys. J. D 46 (2008) 195.
4. Du Hong-Chuan, Zhu Peng-Jia, Sun Shao-Hua and LiuZuo-Ye, Chin. Phys. B 18 (2009) 2427.
5. M. Lezius, S. Dobosz, D. Normand and M. Schmidt, Phys. Rev. Lett. 80 (1998) 261.
6. T. Ditmire, J. W. G. Tisch, E. Springate, M. B. Masson, N. Hay, R. A. Smith, J. P. Marangos and M. H. R. Hutchinson, Nature 386 (1997) 54.
7. A. McPhersonB. D. Thompson, A. B. Borisov, K. Boyer and C. K. Rodes, Nature 370 (1994) 631.
8. T. Ditmire, J. W. G. Tisch, E. Springate, M. B. Masson, N. Hay, J. P. Marangos and M. H. R. Hutchinson, Phys. Rev. Lett. 78 (1997) 2732.
9. T. Ditmire, J. Zweiback, V. P. Yanovsky, T. F. Cowan, G. Hays and K. B. Wharton, Nature 398 (1999) 489.
10. Amol R. Holkundkar and N. K. Gupta, Contrib. Plasma Phys. 49 (2009) 403.
11. T. Ditmire, T. Donnelly, A. M. Rubenchik, R. W. Falcon and M. D. Perry, Phys. Rev. A. 5 (1996) 3379.
12. F. Megi, M. Belkacem, M. A. Bouchen, E. Suraud and Zweicknagel, J. Phys. B: At. Mol. Opt. Phys. 36 (2003) 273.
13. M. Belkacem, F. Megi, P. G. Reinhard, E. Suraud and G. Zwicknagel, Phys. Rev. A. 73 (2006) 051201.
14. V. P. Krainov and M. B. Smirnov, Phys. Rep. 370 (2002) 237.

Cite this article as:

N. Boucerredj *et al.*: **Femtosecond study of the interaction of intense femtosecond laser pulse with Kr clusters using Landau damping.** ScienceJet 2012, **1**: 9

© Cognizure. All rights reserved.

Mössbauer studies of the nanostructured Fe (Si, Cr) alloys

B. Bouzabata[a,*], Z. Bensebaa[a], A. Djekoun[a], J. M. Grenèche[b]

[a] *Laboratoire de Magnétisme et de Spectroscopie des Solides (LM2S), Département de Physique, Faculté des Sciences, Université Badji Mokhtar- Annaba, B.P 12-23000 Annaba, Algérie*
[b] *Laboratoire de Physique de l'Etat Condensé, UMR CNRS 6087, Université du Maine, 72085 Le Mans, France*

[*]*Authors for correspondence: B. Bouzabata, email: bouzabata@yahoo.fr*
Received 4 Feb 2012; Accepted 20 Apr 2012; Available Online 28 Apr 2012

Abstract

Nanostructured Fe (Si,Cr) alloys were elaborated by mechanical alloying of pure elements with 3 compositions $Fe_{80}Si_{10}Cr_{10}$, $Fe_{70}Si_{20}Cr_{10}$ and $Fe_{75}Si_{10}Cr_{15}$ milled for 5, 10 and 15 hours (h). Mössbauer spectra of the milled powders, taken at room temperature, show a broad ferromagnetic component and for low silicon content (10% at.) a central paramagnetic singlet peak. Adequate computer fittings can then be achieved by a distribution of hyperfine fields P (B) from which the environments of the Fe atoms and the mean hyperfine parameters can be deduced. It is then seen that the nanostructured alloys are highly disordered. For the $Fe_{80}Si_{10}Cr_{10}$ alloy, increasing the milling time up to 15 hours gives a more homogeneous distribution that can be separated in two regions for low and high fields that can be attributed to different atomic substitutions of the Fe atoms and/or to the contribution of the grain boundary structure. Increasing the Cr content such as in the nanostructured $Fe_{75}Si_{10}Cr_{15}$ alloy induces a heterogeneous and larger distribution of hyperfine fields with 4 peaks, indicating the presence of various Fe environments usually observed in the FeCr alloys. In the contrary, adding the Si such as in the nanostructured $Fe_{70}Si_{20}Cr_{10}$ alloy, inhibits the formation of the paramagnetic phase and favors the formation of nanoclusters with very small hyperfine fields.

Keywords: Nanocrystalline material; Mechanical alloying; Fe (Cr,Si) alloy; ^{57}Fe Mössbauer spectrometry

1. Introduction

The Fe (Si,Cr) alloys are usually used with large grains as soft magnetic materials since they are found industrially in electromagnetic wave absorber for mobile phone, local area network or in radar systems. In fact, they have been subject of several studies related with their structural and magnetic properties [1,2]. And additions of Si and Cr to Fe alloys enhance respectively the electrical resistivity and the corrosion resistance at atmospheric and higher temperatures. In the nanostructured $(Fe_{65}Co_{35})_{100-x}Si_x$ (x=0,10,20) [3] or in $Fe_{50}(Co_{50})$-6.5 wt%. Si [4] alloys, Si also influences the decrease of grain sizes [3] as well as the values of saturation magnetization. In flaky $Fe_{85}Si_{9.5-x}Al_{5.5}$ Cr_x (x=0,2,4,6) alloy powders [5], adding Cr to replace Si acts to the formation of a metastable α-Fe(Al,Si) superlattice phases. It is then of high interest to study these nanostructured Fe (Si,Cr) alloys since the nanometric grain size is expected to improve mechanical and magnetic properties. These kinds of materials are very attractive since their nanometric property is implying further fundamental studies and technological applications [6,7]. Various methods such as mechanical alloying (M.A) [8] are used for their elaboration. M.A by high energy ball milling is a well-known powder producing process and has been used to synthesize a broad variety of non-equilibrium states with respect to microstructure and composition including amorphous structures [9,10] starting from pure elemental or pre-alloyed powders submitted repeatedly to severe deformations with fracture and welding processes [8]. M.A leads to achieve chemical reactions and usually induces structural changes.

In our work, the nanostructured $Fe_{80}Si_{10}Cr_{10}$, $Fe_{70}Si_{10}Cr_{15}$ and $Fe_{70}Si_{20}Cr_{10}$ alloys were elaborated by M.A . The grain sizes of the obtained powders are less than 25 nm for milling times above 3 hours. Structural and magnetic properties were investigated. And influences of Si and Cr additions on the structural and atomic disorders are discussed mainly from the results of Mössbauer spectra.

2. Elaboration and fittings procedures

Mechanical alloying was carried out in a planetary high energy ball mill (Fritsch Pulverisette P7) starting from pure elements of iron, silicon and chrome, with different relative concentrations. Their primary particles were previously observed by scanning electron microscopy [11] with sizes of about 6, 150 and 200 microns respectively. Mechanical milling was carried out at a frequency of 6.6 Hz under argon atmosphere, using hardened steel balls and vials. The ball to powder weight ratio was set to 17:1. The milling times were 5, 10 and 15 h. The ^{57}Fe Mössbauer spectra were performed at room temperature in a transmission geometry using a conventional constant acceleration spectrometer. Hyperfine parameters were obtained from the fittings of the Mössbauer spectra by using the MOSFIT program [12], with an adequate distribution of hyperfine fields $P(B) = \Sigma\, a_n \{ \cos(n\pi\, B/ Bc) - (-1)^n\}$, where Bc= 34 Tesla (T) and the mean hyperfine field $\langle B\rangle = \Sigma\, B\, P(B)/ \Sigma P(B)$. Also P (B) is set to zero if calculated values are negative.

The mean grain size of all milled powders was less than 25 nm. This indication has been obtained from the Rietveld fit of the XRD spectra by using the Maud program. The variations of <L> (mean grain size) and of the microstrain as a function of milling time (hours) (given from the fit of the XRD spectra) are given in the Figure 1 (for $FeSi_{10}Cr_{15}$ powder as an example).

© Cognizure. All rights reserved.

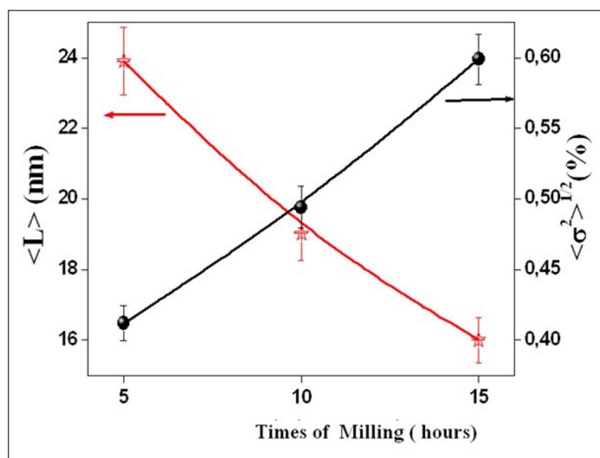

Figure 1. Rietveld fit of the XRD spectra by using the Maud program for $FeSi_{10}Cr_{15}$ powder.

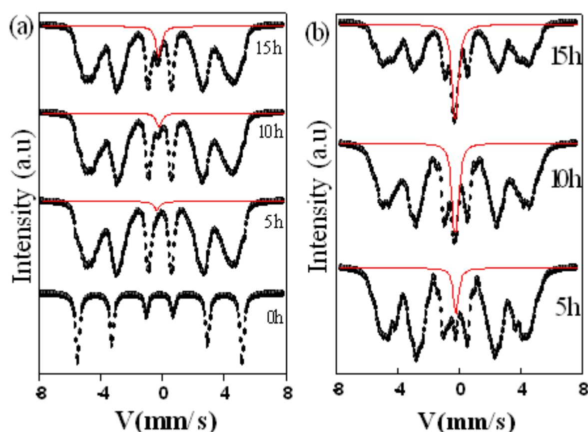

Figure 2. Mössbauer spectra of the $Fe_{90-x}Si_{10}Cr_x$ (x=10, 15) mixture milled for different times: (a) $Fe_{80}Si_{10}Cr_{10}$ (b) $Fe_{75}Si_{10}Cr_{15}$.

3. Hyperfine parameters of the Mössbauer spectra

Mössbauer spectra of the $Fe_{80}Si_{10}Cr_{10}$ and $Fe_{75}Si_{10}Cr_{15}$ powders, taken at room temperature, for different milling times are shown in Figure 2. As expected, the Mössbauer spectrum of the unmilled $Fe_{80}Si_{10}Cr_{10}$ powder (Figure 2(a)) presents the six symmetrical sharp lines of pure iron. After 5 h of milling time, the spectrum consists of a ferromagnetic sextet with 6 broad lines characteristic of a disordered structure where iron atoms are largely replaced by atoms of silicon and/or chromium atoms and a paramagnetic singlet with a relative area (or relative concentration) of about 1%. For higher milling times (15 h), the paramagnetic phase increases to about 4%. Increasing the relative concentration of Cr as in the case of the $Fe_{75}Si_{10}Cr_{15}$ powder (Figure 2(b)) gives the same features with two ferromagnetic and paramagnetic contributions. However, as shown by small variations in the lines 1 and 6, the distribution of the hyperfine fields is not homogeneous indicating the presence of various environments of iron. Also, the intensity of the paramagnetic singlet line is higher. Its relative concentration increases from 6.5% to 17.5% as the milling time varies up to 15 h. Values of the mean isomers shifts (relatively to metallic iron) are given in Table 1 and they

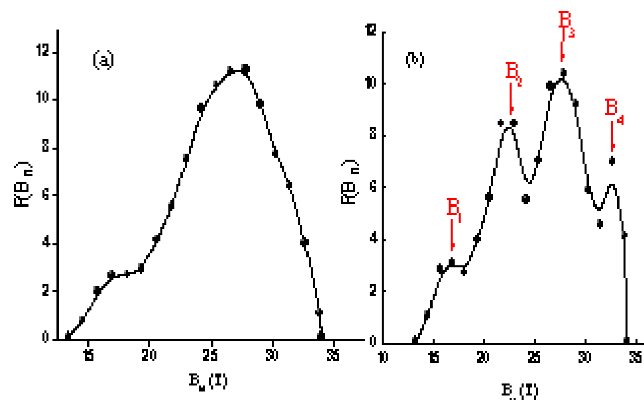

Figure 3. Hyperfine fields distribution $P(B_{hf})$ of the (a) $Fe_{80}Si_{10}Cr_{10}$ and (b) $Fe_{75}Si_{10}Cr_{15}$ mixture milled for 15 h.

all are negative indicating the main influence of Cr atoms (to the contrary of Si atoms that increase the isomer shift of iron).

Figure 3 shows the hyperfine field distribution curves of the $Fe_{80-x}Si_{10}Cr_x$ (x=10, 15) powders milled for 15 hours. It is observed that the hyperfine distributions curve P (B_{hf}) of the $Fe_{80}Si_{10}Cr_{10}$ powder (Figure 3(a)) can be separated in two regions: one with low fields and probabilities (< 20 T, B (probable) = 17 T) and the other with high fields and probabilities (range 20-33 T, B (probable) = 27 T), with a relative area ratio of 9 and 91%, respectively. This result is reported and discussed in detail in reference [11]. But the hyperfine field distribution curve $P(B_{hf})$ of the $Fe_{75}Si_{10}Cr_{15}$ powder milled for 15 h (Figure 3b) is composed of 4 distributions (or 4 Gaussian components) corresponding to 4 different most probable hyperfine fields at values of B_1 = 17 T, B_2 = 22 T , B_3 = 28 T and B_4 = 32.7 T.

These values of hyperfine fields can be related to the different environments of iron. It is well known that one Cr atom in the first and in the second neighbour shell decreases the values of the hyperfine field by 3 and 2 T, respectively [13]. Also, one Si atom in the first coordination shell decreases the hyperfine field by 2.5 T [14]. Value of B_1 can then be obtained for a chromium-rich FeCr alloy where iron atom may have 5 to 7 chromium atoms on the two first coordination spheres. Values of B_2 and B_3 can also be obtained in Fe (Si, Cr) alloy where the iron atom is surrounded in the first coordination sphere by 5 to 2 atoms of either Si or Cr. And value of B_4 is probably due to an environment similar to that of pure iron that is not yet alloyed with Si and Cr.

The above results indicate that the paramagnetic phases are mainly due to the presence of Cr atoms. And an addition of Cr to 15% at. increases the structural and atomic disorders since the distribution of hyperfine fields is not homogeneous being decomposed in 4 main contributions.

The Mössbauer spectra and the corresponding hyperfine field distribution curve, P (B_{hf}), for the $Fe_{70}Si_{20}Cr_{10}$ powder are presented in Figure 4. It is observed that the Mössbauer spectra consist of a unique sextet with enlarged lines related to the existence of several types of local environments of iron that results in a distribution of hyperfine fields P (B_{hf}). This structured disorder in which iron atoms are diversely and largely replaced by atoms of Cr and Si produces a disordered solid solution.

However, the observed P (B) of the $Fe_{70}Si_{20}Cr_{10}$ powder extends to very low hyperfine fields (about 2 T) although with very low probabilities. The low hyperfine fields

© Cognizure. All rights reserved.

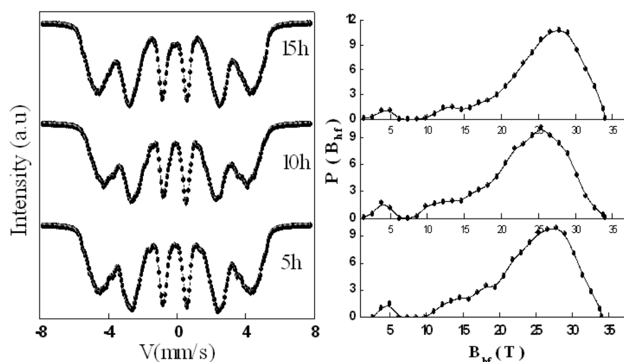

Figure 4. Mössbauer spectra and the corresponding hyperfine fields distribution $P(B_{hf})$ of $Fe_{70}Si_{20}Cr_{10}$ mixture for different milling times.

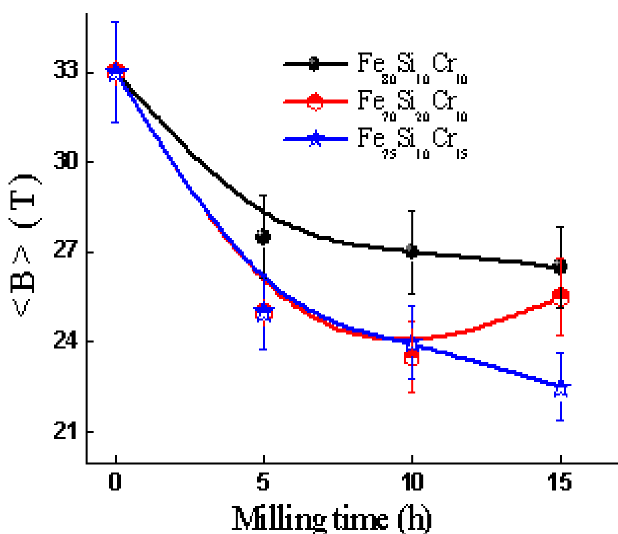

Figure 5. Milling time dependence of the mean hyperfine field, <B> (T), of the $Fe_{80}Si_{10}Cr_{10}$, $Fe_{75}Si_{10}Cr_{15}$ and $Fe_{70}Si_{20}Cr_{10}$ mixture.

are usually attributed to the nanoclusters or disordered grains boundaries. Figure 5 presents the dependence of the mean hyperfine field (<B> (T)) with milling time of the ferromagnetic component of the milled $Fe_{80}Si_{10}Cr_{10}$, $Fe_{75}Si_{10}Cr_{15}$ and $Fe_{70}Si_{20}Cr_{10}$ powders. A gradual decrease of the mean hyperfine field is observed for the $Fe_{80}Si_{10}Cr_{10}$, $Fe_{75}Si_{10}Cr_{15}$ mixture that is related to the gradual substitution of iron atoms by Cr and Si. Lower values of the mean hyperfine fields for the $Fe_{75}Si_{10}Cr_{15}$ mixture is also due to the higher concentration of added substituted elements. However, the mean hyperfine field of the milled $Fe_{70}Si_{20}Cr_{10}$ powder increases after 15 hours of milling. This behavior is due to the non-formation of the paramagnetic phase that increases the relative concentration of iron. Similar results were obtained in the milled $FeCr_{31}Co_{12}$ [15], FeCr [16] and FeSi alloys [17, 18].

The variation of the mean isomeric shift <IS> (mm/s) with milling time of the ferromagnetic component of the $Fe_{80}Si_{10}Cr_{10}$, $Fe_{75}Si_{10}Cr_{15}$ and $Fe_{70}Si_{20}Cr_{10}$ powders is shown in Figure 6. It is observed that <IS> is negative for the milled $Fe_{75}Si_{10}Cr_{15}$ alloy and positive for the other milled alloys due to the probable compensating effect of Si relatively to Cr. Furthermore, it increases gradually with milling time for the

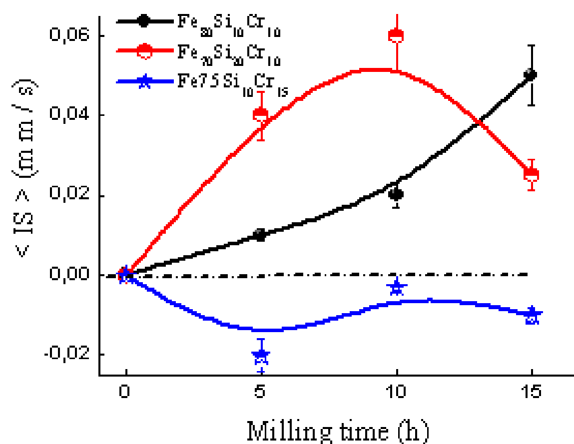

Figure 6. Variation of the isomeric shift <IS> of the ferromagnetic contribution of the $Fe_{80}Si_{10}Cr_{10}$, $Fe_{75}Si_{10}Cr_{15}$ and $Fe_{70}Si_{20}Cr_{10}$ mixture with milling time.

$Fe_{80}Si_{10}Cr_{10}$ powder indicating different kinetics of substitutions of Si and Cr atoms in the iron atom.

4. Conclusions

Nanostructured $Fe_{80}Si_{10}Cr_{10}$, $Fe_{75}Si_{10}Cr_{15}$ and $Fe_{70}Si_{20}Cr_{10}$ alloys were elaborated by mechanical alloying. From Mössbauer spectra and the obtained distribution of hyperfine fields, it is seen that Cr increases the formation of a paramagnetic phase and a highly disordered ferromagnetic phase with various environments of iron atoms. Addition of Si inhibits the paramagnetic phase and shows the presence of small hyperfine fields.

References

1. M. S. Kim, E. H. Min, J. G. Koh, J. Magn. Magn. Mater. 321 (2009) 581.
2. R. S. Turtelli, T. Krenicky, A. Penton-Madrigal, R. Grossinger, I. Skorvanek, H. Sassik, E. Estevez-Rams, M. Schonhart, C. da F. Barbatti., J. Magn. Magn. Mater. 304 (2006) 687.
3. M. Yousefi, S. Sharafi, Mater. Design 37 (2012) 325.
4. T. D. Zhou, J. K. Tang, Z. Y. Wang, J. Magn. Magn. Mater. 322 (2010) 2589.
5. M. Khajepour, S. Sharafi, J. Alloys Compd. 509 (2011) 772.
6. Z. Bensebaa., B. Bouzabata., A. Otmani, J. Alloys Compd. 469 (2009) 24.
7. F. Karimzadeh, M. H. Enayati, M. Tavoosi, Mater. Sci. Eng. A 486 (2006) 45.
8. C. Suryanarayana, Prog. Mater Sci. 46 (2001) 1.
9. N. Bensebaa, S. Alleg, F. Z. Bentayeb, L. Bessais, J. M. Grenèche, J. Alloys Compd. 388 (2005) 41.
10. S. W. Du, R. V. Ramanujan, J. Magn. Magn. Mater. 292 (2005) 286.
11. Z. Bensebaa, B. Bouzabata, A. Otmani, A. Djekoun, A. Kihal, J. M. Grenèche, J. Magn. Magn. Mater. 322 (2010) 2099.
12. F. Varret, J. Teillet, Mosfit program, unpublished (1976).
13. S. M. Dubiel, J. Zukrowski, J. Magn. Magn. Mater. 23 (1981) 214.
14. E. Japa and K. Krop, J. Phys. Stat. Sol. (b) 96 (1979) K65.
15. F. Z. Bentayeb, S. Alleg, B. Bouzabata., J. M. Grenèche, J. Magn. Magn. Mater. 288 (2005) 282.
16. C. Lemoine, Thèse de Doctorat: Etude structurale et magnétique de mélanges FeCr élaborés par mécanosynthèse, Université de Rouen-France (2000).

© Cognizure. All rights reserved.

17. M. Abdellaoui, C. Djega-Mariadassou, E. Gaffet, J. Alloys Compd. 259 (1997) 241.
18. L. K. Varga, F. Mazaleyrat, J. Kovac and J. M. Greneche, J. Phys. Condens. Matter 14 (2002) 1985.

Cite this article as:

B. Bouzabata *et al.*: **Mössbauer studies of the nanostructured Fe (Si, Cr) alloys.** ScienceJet 2012, **1**: 10

© Cognizure. All rights reserved.

Low-RF-power deposition of p-type microcrystalline silicon emitters

A. Casado[a,*], I. Torres[a], J. D. Santos[a], R. Barrio[a], J. J. Gandía[a], J. Cárabe[a], G. Bianco[b], M. Losurdo[b], G. Bruno[b]

[a] CIEMAT, Av. Complutense, 22, 28040, Madrid, Spain
[b] IMIP, CNR, via Orabona, 4, 70126 Bari, Italy

[*]Authors for correspondence: A. Casado, email: alberto.casado@ciemat.es
Received 4 Feb 2012; Accepted 27 Apr 2012; Available Online 28 Apr 2012

Abstract

P-doped microcrystalline silicon films (μc-Si:H(p)) have been deposited by plasma-enhanced chemical vapour deposition (PECVD) using low RF power, from a silane and trimethylboron ($SiH_4/B(CH_3)_3$) mixture diluted in helium (He) and hydrogen (H_2). The material has been optically, electrically and structurally characterised. This work focuses on the effect of depletion regime on the properties of μc-Si:H(p). Four deposition parameters have been explored, all of them determining the amount of energy supplied per gas molecule, specifically the pressure (*P*), the total mass-flow (Φ_T), the He- and H_2-dilution – *D(He)* and $D(H_2)$ – and the applied radio-frequency power (*RFP*). The material developed here is intended to be used in the future as a BSF (back surface field) in silicon-heterojunction (SHJ) solar cells with a metal/TCO/a-Si:H(n)/c-Si(p)/μc-Si:H(p^+)/metal configuration.

Keywords: Silicon heterojunction; Microcrystalline silicon; Solar cells; Emitter; He-dilution; Depletion regime

1. Introduction

Different materials have been developed and investigated in the field of semiconductor-based photovoltaics in a quest for a gradual decrease of production costs. A myriad of solar cells have also been implemented by introducing one (or generally more than one) novel material depending on diverse technical and commercial purposes.

Since the first report by Veprek [1], microcrystalline silicon (μc-Si:H) has been intensively studied and tested in many optoelectronic devices, such as sensors and solar cells. The wide range of possible microscopic structures of this material allows it to be employed in multiple configurations. High conductivity, good optical properties and stability in the presence of light are, among others, important advantages of this material. Different properties can be achieved depending on the material intrinsic structure, i.e. crystallite size, distribution, orientation, amorphous matrix density, hydrogen content, etc. Microcrystalline silicon is usually prepared by adding hydrogen to the gas mixture and boosting RF power and process pressure. These conditions favour the formation of powder, the deposition of material on the chamber walls and the formation of defects on the sample surface owing to an excessive ion bombardment. The present work is aimed at finding softer plasma conditions for the PECVD preparation of microcrystalline silicon, having in mind its use as a solar-cell emitter, with particular emphasis on its application to silicon-heterojunction solar cells.

Microcrystal growth is favoured by the competition between silicon deposition from silane and selective etching from hydrogen, so the presence of hydrogen atoms in the plasma is absolutely essential. These hydrogen atoms are not only generated by the decomposition of the molecular hydrogen usually included in the gas mixture, but also by the breaking of the silane molecules. In either case, the density of atomic hydrogen in the plasma is directly related to the amount of energy absorbed per gas molecule, i.e., to the depletion regime. Previous studies [2] have demonstrated that such a ratio is governed by the power-to-flow ratio, rather than just by power. Of course pressure also plays an important role by means of its direct influence on residence time. Taking all this into account, the deposition conditions have been tuned in such a way that it has been possible to deposit microcrystalline silicon films in low-RF-power conditions.

The material developed in this work is intended to be used as a back-surface field (BSF) [3] in a silicon-heterojunction (SHJ) solar cell, with a metal/TCO/a-Si:H(n)/c-Si(p)/μc-Si:H(p^+)/metal configuration, forming a p-p+ junction at the rear side of the cell. Thus, no restrictions on transparency or gap energy are necessary. Instead, a high conductivity, σ, a low activation energy, E_A, and acceptable doping levels are sought.

The dopant atoms are obtained from trimethylboron, TMB or $B(CH_3)_3$, which is a thermally stable gas, and much less hazardous than diborane. Additionally, it reduces the risk of boron contamination in hot zones [4].

He-dilution has been used on the basis of former results in our laboratory [2]. Although it has been widely reported before that H_2-dilution is a convenient approach to obtain microcrystalline material, previous results in the literature show that it is also possible to deposit μc-Si:H from He-diluted plasmas [2, 5-7]. Since He is an inert gas, reactions of the diluent with the crystalline precursors are avoided. This fact, together with the possibility to obtain a high-density plasma at a relatively low power, pressure and temperature, makes He a suitable diluent for the deposition of μc-Si:H. Here He is used as an extra diluent, combined with H_2. In this way, it may be seen as a component providing an additional degree

© Cognizure. All rights reserved.

Table 1. Deposition parameters for the five sets discussed. The substrate temperature during deposition, and the distance between electrodes, have been fixed to 245ºC and 22 mm, respectively. Also the SiH_4 and TMB fluxes have been set to 1.5 and 0.4 sccm, respectively. Deposition time has been calculated so as to obtain approximately the same thickness (***d***) for all samples. The error in ***d*** is due to a different-from-expected growth rate.

Set ID	*P* (mTorr)	*RFP* (W)	*D(He)* (%)	$D(H_2)$ (%)	Φ_T (sccm)	*d (nm)*
P	500 - 1300	100	95,5	0	41,9	300 ± 44
$\boldsymbol{\Phi_T}$	700	100	97 - 100	0	41.9 - 91.9	285 ± 15
He + H	550	100	95.5 - 71.6	0 - 23.9	41,9	205 ± 30
RFP1	700	40 - 100	96	0	41,9	250 ± 6
RFP2	550	40 - 100	71,6	23,9	41,9	220 ± 20

of freedom: when a continuous flow of He is introduced in the chamber, the quantitative composition of the mixture of gases involved in the crystallisation process (namely SiH_4 and H_2) becomes more accurately controllable.

2. Experimental

2.1. Film preparation

Microcrystalline silicon films were deposited by means of a radio-frequency plasma (RF-PECVD) system, equipped with a shower-head electrode, using an excitation frequency of 13.56 MHz. All samples were grown from a gas mixture of He, SiH_4, TMB and, in a number of cases H_2, onto 10x10-cm^2 soda-lime glass substrates.

The deposition parameters for the different sets of samples discussed in this article are shown on Table 1. Previous experiments had indicated that microcrystalline material grew only for the lowest fluxes of TMB and silane, consistently with results in the literature [8]. Yet our mass-flow controllers imposed a lower limit for each gas.

The dilution *D(X)*, corresponding to gas *X*, is defined as:

$$D(X) = 100 * \Phi_X / \Phi_T$$

Φ_X being the flux corresponding to gas *X*, and Φ_T the total flux defined as the sum of the fluxes of every gas entering the chamber:

$$\Phi_T = \Sigma\, \Phi_i$$

2.2. Film characterisation

Conductivity under dark (σ_D) and light (σ_L) conditions were measured at room temperature in a coplanar configuration with evaporated aluminium contacts. Voltages were induced by means of a Keithley 228A bipolar power supply in the range from -100 V to +100 V and currents were measured by means of a Keitley 619. A metal-halide class-A solar simulator Atlas SC575 provided AM1.5G calibrated 100 mW/cm^2 irradiance for photoconductivity measurements.

Thicknesses were obtained from reflectance, R(λ), and transmittance, T(λ). Spectra were measured with a UV-VIS-NIR Perkin-Elmer Lambda 1050 spectrophotometer by applying standard procedures [9].

Spectroscopic-Ellipsometry (SE) measurements were carried out in the range 1.5-6.5 eV by means of a phase-modulated spectroscopic ellipsometer (UVISEL-Horiba Jobin Yvon), at the 70º angle of incidence. The film thickness and structure were derived by fitting the pseudo-dielectric function using the Bruggeman effective-medium approximation (BEMA) and a linear regression analysis. SE has already been shown to be a very useful technique to characterise both structure and thickness of μc–Si:H [10, 11]. Here an accurate match with thicknesses obtained from other optical methods was obtained, as it will be shown in the next section.

Raman crystalline fraction (χ_{Raman}) was calculated from micro-Raman spectra according to the expression:

$$\chi_{\text{Raman}} = \frac{I_{\mu c-Si}}{I_{\mu c-Si} + I_{a-Si}} = \frac{I_{520} + I_{510}}{I_{520} + I_{510} + I_{480}}$$

This relation takes into account the amorphous (I_{480}), the crystalline (I_{520}) and the grain-boundary (I_{510}) contributions, and is often used for crystalline fraction determination from Raman spectra [12, 13]. The peak at 510 nm considers the grain boundaries and varies in relation to typical grain sizes inside the material [14, 15]. The χ_{Raman} quantity should be taken only as a laboratory check, since it usually underestimates the real crystalline fraction [12, 16-18].

3. Results and Discussion

The influence of four deposition parameters on the properties of μc-Si:H(p) are discussed in this section. Specifically, the pressure (*P*), the total flux (Φ_T), the He- and H-dilution – *D(He)*, $D(H_2)$, respectively - and the applied radio-frequency power (*RFP*), have been varied and five sets of samples have been analysed.

In general, deposition conditions for obtaining either intrinsic, (i), or p-doped μc-Si:H may not match at all. In the present work, similar deposition conditions to those reported in reference [2] (in which the same reactor was used to deposit intrinsic μc-Si:H) have been initially chosen.

3.1. Effect of pressure

A set of samples obtained by varying *P* from 500 to 1300 mTorr is considered in Figure 1. Possibly the low values measured for σ in this set are caused by a large density of defects, where majority carriers can be trapped in, as has been suggested previously [19]. This is perhaps worsened by low doping levels. χ_{Raman} follows the same trend as σ, although it is not shown in Figure 1. The activation energy (and the crystalline fraction, which follows the trends of σ but is not shown for clarity of the pictures) indicates that the amorphous-to-crystalline transition occurs from 500 to 550 mTorr. For pressures between 550 and 1000 mTorr, the electrical properties are maintained, whereas for higher *P* they are clearly deteriorated. Also a slight photosensitivity ($PS = \sigma_D / \sigma_L$) is observed for these samples, suggesting insufficient doping.

3.2. Effect of total flux

Generally, SiH_4 high-depletion regime promotes microcrystalline growth [2, 20]. The ratio (RFP / Φ_T) regulates the energy available per molecule and thus the depletion. One way to obtain a high depletion is to diminish the total flux. In this case, Φ_T has been varied between 41.9

© Cognizure. All rights reserved.

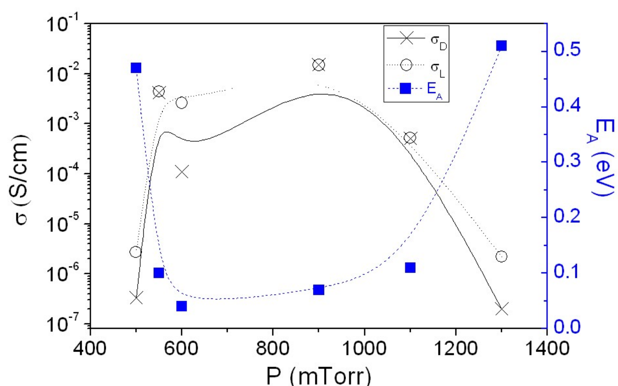

Figure 1. Conductivity under respectively dark (σ_D) and light (σ_L) conditions on the left, and activation energy (E_A) on the right, as a function of pressure (P) in the chamber.

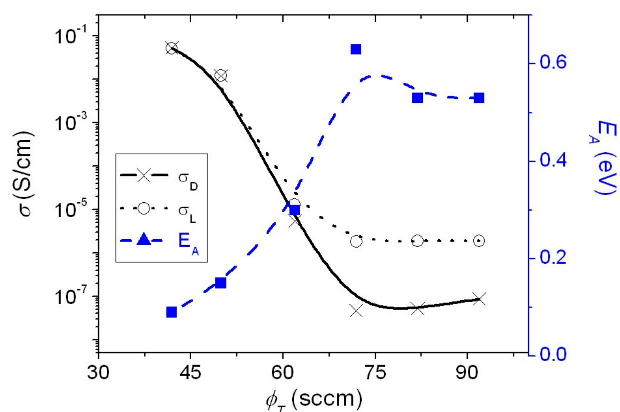

Figure 2. Conductivity (σ) on the left axis and activation energy (E_A) on the right one, plotted as functions of the total flux.

Table 2. Raman crystallinity fraction as a function of He and H_2 dilution.

D(He) (%)	D(H_2) (%)	χ_{Raman} (%)
95.5	0.0	18.6
83.5	11.9	56.1
71.6	23.9	55.1

and 91.9 sccm. As can be seen in Figure 2, there is an increment of σ by decreasing Φ_T values, while E_A reaches a minimum at the lowest Φ_T, indicating the transition to μc material.

Correspondingly, the Raman crystallinity follows the same tendency as σ, and shows the same transition. This may indicate that at constant pressure, t_R increases when Φ_T decreases (at low fluxes, molecules will remain longer inside the chamber). Additionally, a high t_R implies high probability of SiH_4 dissociation and this increases the probability of crystalline precursor formation. Thus lower the total flux, the higher the probability of crystalline nuclei formation, and hence a higher crystalline ratio may be achieved. This explains also the increment of the conductivity.

3.3. Effect of dilution

Table 2 shows the crystallinity fraction as a function of He and H_2 dilution, indicating that the addition of H_2 to the gas mixture is considerably convenient to achieve high crystalline fractions. SE spectra confirm this result, as it can be inferred from Figure 3. Here, it can be seen qualitatively that the E_1 and E_2 interband critical points respectively at 3.6 eV and 4.2 eV, which are a signature of the crystalline phase (see for example [10]) are enhanced as He is replaced by H_2.

The improvement of film crystallinity has also been observed when comparing two sets of samples, one with only He (set named RFP1) and the other one with He-H_2-dilution (RFP2). Figure 4 shows the conductivity and Raman crystalline fraction obtained for each set. It has been repeatedly demonstrated in previous studies that H_2 favours crystalline-precursor formation and it has been mentioned that it could

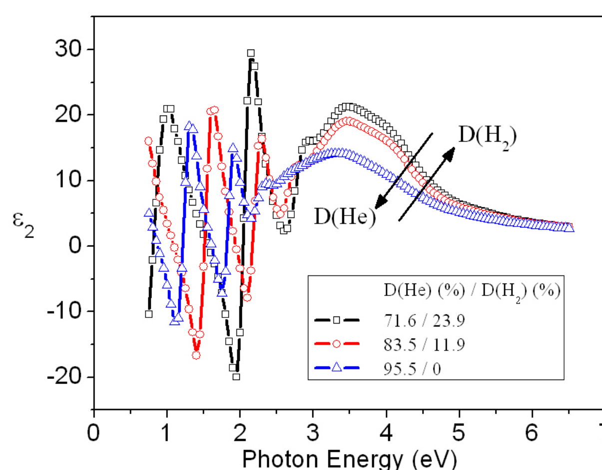

Figure 3. Imaginary part of the pseudo-dielectric function of three samples made at different H_2 and He-dilution. The E_1 (at 3.6 eV) and E_2 interband critical points (at 4.2 eV) are enhanced with the increase of H_2, indicating an improvement t of the crystalline phase.

even passivate grain-boundary defects [21]. Having observed above (Figure 1) that pressure changes between 550 and 700 mTorr do not significantly affect the material conductivity and E_A, it is deduced that H_2 is facilitating, together with He, the crystalline growth of the initial nuclei, in agreement with previous studies [22, 23].

3.4. Effect of the RF-power

RFP variation is another way to explore different depletion conditions. As it can be seen in Figure 4, *PS* becomes negligible for *RFP* ≥ 80W when the samples are made with He-dilution (RFP1) only. With the increase in applied RF-power, a higher amount of TMB molecules are dissociated, resulting in more Boron atoms in the plasma. In addition, an increment of crystallinity with *RFP* is observed for this set, as shown in Figure 4. The B incorporation into the material is facilitated by the crystalline character of the lattice, and therefore higher doping levels are obtained when increasing *RFP*.

© Cognizure. All rights reserved.

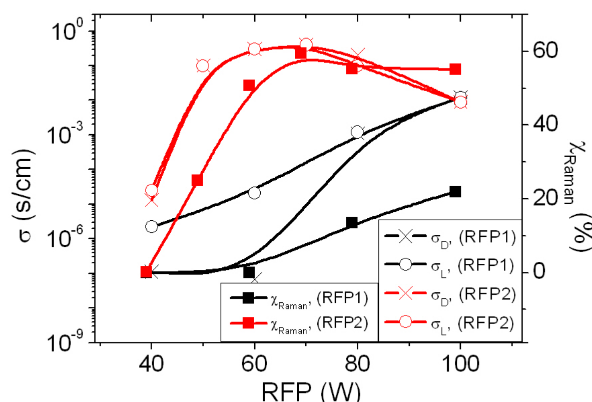

Figure 4. Photoconductivity (σ_L) dark conductivity (σ_D) and Raman crystallinity for both sets: RFP1 (700 mTorr, He-dilution) and RFP2 (550 mTorr, He+H_2 dilution). (Corresponding deposition parameters are listed on Table 1).

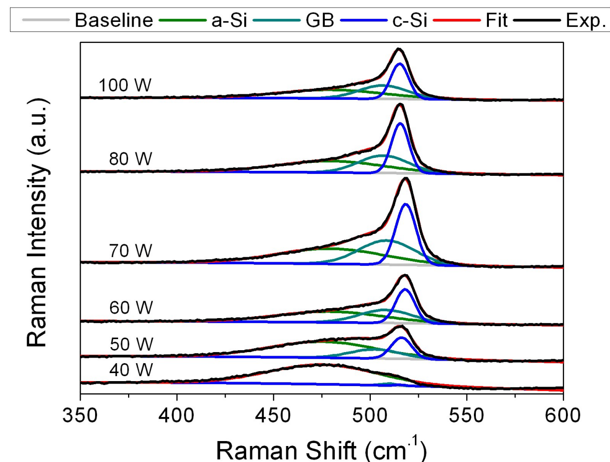

Figure 5. Micro-Raman spectra from samples corresponding to the RFP2 set. Both the experimental spectra (Exp) and the fitting (Fit) are shown. The last is obtained from sum of the amorphous silicon (a-Si), grain boundary (GB), and the crystalline silicon (c-Si) contributions.

In the case of RFP2 (in which a small flow of H_2 is added to the gas mixture), both a conductivity and a crystalline fraction remarkably higher than those obtained for RFP1 are achieved for similar *RFP* values. The addition of H_2 to the gas mixture favours the enhancement of H^+ ions in the plasma even when the silane depletion regime is kept unchanged. This favours the triggering of microcrystal formation and, therefore a more efficient doping, since a higher crystallinity facilitates the diffusion of B atoms into the lattice, thus increasing σ and decreasing *PS*. Yet, too high applied *RFP* causes a conductivity drop of an order of magnitude (red points in Figure 4), probably owing to an excessive ion bombardment. This interpretation is consistent both with the evolution of the Raman crystalline fraction (see Figure 4 and Figure 5) and with SE measurements, where void density appears to rise at the maximum power (100 W) (See Table 3). At low *RFPs*, a low depletion of silane leads to a lack of microcrystalline precursors. From 40 to 50 W, the amorphous-to-crystalline transition can be observed.

Table 3 summarises the results of the optical modelling of SE spectra analysis for four of the samples of the RFP2 set with comparable thicknesses. First, an agreement has been found between thicknesses obtained from optical methods and from SE spectra fitting (this is true in general for all the samples analysed). It can also be observed there is a correlation between the incubation layer thickness, the growth rate and the conductivity. In fact hydrogen bombardment seems to control incubation-layer formation. For low depletion (low *RFP*), relatively few H atoms reach the surface, so most of the species thereon remain in the growing film and the resulting lattice turns out to be amorphous.

Finally, a poor adherence has been obtained when too high values of power are applied (typically above 100 W), possibly because of damage due to an increase of ion bombardment on the surface.

Table 3. Optical models obtained from SE spectra fitting by the BEMA. It has been supposed that the material has a three-layer structure: An inner layer, which represents the incubation layer, a bulk layer with different densities and a top layer which represents the roughness of the film (~50 % voids). Also shown on top is the *RFP* applied for the deposition of each sample, the thickness of each sample has been calculated by optical methods and the growth rate derived thereof.

	RFP (W)	50	60	70	100
	Optical thickness (nm)	206	256	228	180
	Growth rate (Å/s)	0.69	0.85	0.76	0.60
Roughness layer	**Thickness (nm)**	**9**	**8**	**7**	**4**
	Void (%)	55	44	52	50
	μc-Si (%)	30	12	37	3
	a-Si (%)	15	44	11	47
Bulk layer	**Thickness (nm)**	**139**	**159**	**121**	**135**
	Void (%)	3	0	0	9
	μc-Si (%)	10	69	65	64
	a-Si (%)	87	31	35	27
Incubation layer	**Thickness (nm)**	**41**	**72**	**64**	**17**
	a-Si (%)	67	100	96	100
	Void (%)	33	0	4	0

© Cognizure. All rights reserved.

4. Conclusions

Various techniques have been applied to characterise PECVD-deposited μc-Si:H(p). It has been shown that although it is possible to deposit μc-Si:H(i) from a He-diluted plasma, a small flow of H_2 allows a better-quality p-doped material to be used as a BSF in SHJ solar cells, with σ ~ 0.4 S/cm and a χ_{Raman} ~ 60%. This material might be used as a BSF in SHJ solar cells. An incubation layer with a thickness between 60 and 70 nm has been found for films deposited on glass. Although this result might appear incompatible with the aim to make microcrystalline emitters having thicknesses of the order of 30 nm, it should be stressed that the goal is the application to silicon-heterojunction cells. In such a case the layer will grow on crystalline silicon, thus replicating the underlying crystalline structure. This behaviour has already been observed in our a-Si:H(n) emitters. Concerning the relation between deposition conditions and microscopic structure, it has been found that the doping levels and the presence of defects might be influenced by the pressure and the *RFP*. On the other hand, the incubation layer thickness, conductivity and crystalline fraction can be explained in terms of the depletion regime. The RFP / Φ_T ratio seems to govern the microcrystalline growth and the doping efficiency. Additionally, it has been observed that higher crystalline fractions in the material allow improved B-doping.

References

1. S. Veprek, V. Marecek, Solid-State Electron. 11 (1968) 683.
2. I. Torres, et al., Thin Solid Films 518 (2009) 7019.
3. H. D. Goldbach, et al., J. Non-Cryst. Solids 352 (2006) 1872.
4. P. Roca i Cabarrocas, et al., J. Appl. Phys. 66 (1989) 3286.
5. O. Saadane, et al., J. Appl. Phys. 93 (2003) 9371.
6. K. Bhattacharya, D. Das, J. Phys. D: Appl. Phys. 41 (2008) 155420.
7. J. Cárabe, et al., Appl. Surf. Sci. 143 (1999) 11.
8. S. A. Filonovich, et al., Vacuum 83 (2009) 1253.
9. J. L. Hernández-Rojas, et al., Appl. Opt. 31 (1992) 1606.
10. M. Losurdo, J. Appl. Phys. 88 (2000) 2408.
11. M. M. Giangregorio, et al., Appl. Surf. Sci. 253 (2006) 287.
12. E. Vallat-Sauvain, et al., J. Non-Cryst. Solids 352 (2006) 1200.
13. A. Chowdhury et al., Effect of p-layer properties on nanocrystalline absorber layer and thin film silicon solar cells, 6th International Conference on Fine Particle Magnetism, Rome, Italy (Oct 09-12, 2007).
14. S. Veprek, et al., Phys. Rev. B 36 (1987) 3344.
15. C. Droz, et al., Sol. Energy Mater. Sol. Cells 81 (2004) 61.
16. C. Ossadnik et al., Thin Solid Films 337 (1999) 148.
17. M. Ledinský, et al., J. Non-Cryst. Solids 352 (2006) 1209.
18. M. Ledinský, et al., J. Non-Cryst. Solids 354 (2008) 2253.
19. F. Finger, et al., J. Non-Cryst. Solids 266-269 Part 1 (2000) 511.
20. G. Bugnon, et al., J. Appl. Phys. 105 (2009) 064507.
21. F. Finger, et al., Phys. Status Solidi C 1 (2004) 1248.
22. A. Matsuda, Thin Solid Films 337 (1999) 1.
23. S. Klein, et al., Sol. Energy 77 (2004) 893.

Cite this article as:

A. Casado *et al.*: **Low-RF-power deposition of p-type microcrystalline silicon emitters.** ScienceJet 2012, **1**: 11

© Cognizure. All rights reserved.

Effect of dual treatment based on porous silicon and sputter-deposited TiO_2 doped Cr film on the optoelectronic properties of monocrystalline Si

A. Hajjaji[a, b], M. Ben Rabha[a], N. Janene[a], W. Dimassi[a], B. Bessais[a], M. A. El Khakani[b,*], M. Gaidi[a,*]

[a] *Laboratoire de Photovoltaïque, Centre de Recherches et des Technologies de l'Energie, Technopole de Borj-Cédria, BP 95, 2050 Hammam-Lif, Tunisia*
[b] *Institut National de la Recherche Scientifique, INRS-Énergie, Matériaux et Télécommunications, 1650, Blvd. Lionel-Boulet, Varennes, Québec, Canada J3X 1S2*

[*]*Authors for correspondences: M. Gaidi, email: mounir.gaidi@crten.rnrt.tn*
M. A. El Khakani, email: elkhakani@emt.inrs.ca
Received 4 Feb 2012; Accepted 16 Apr 2012; Available Online 19 Apr 2012

Abstract

In this paper, we report on the use of a double treatment based on porous silicon and Cr-doped TiO_2 sputter-deposition, as a novel passivation technique for monocrystalline Si (c-Si). The passivation and antireflection properties of these treatments were investigated. In particular, effect of Cr doping concentration (in the 0-17 at. % range) on the optoelectronic properties of c-Si was investigated. It is particularly found that the PS/TiO_2 (2 at. % of Cr) treated samples present high photoluminescence (PL) intensity and an enhancement of the optoelectronic properties of the c-Si material with respect to other Cr doping concentrations. Consequently the total reflectivity, in the 350 - 700 nm wavelength range, decreases from 35% for untreated c-Si to about 13% after PS/TiO_2 treatment and the effective minority carrier diffusion length of the c-Si was enhanced from 181 µm to 340 µm after combining porous silicon and Cr-doped titanium dioxide deposition.

Keywords: Porous silicon; Titanium dioxide; Cr doped TiO_2; RF magnetron sputtering; C-Si passivation; Photoluminescence

1. Introduction

Porous silicon (PS) has been often explored for its strong visible room-temperature photoluminescence (PL) and for its high potential in silicon photovoltaic (PV) application [1-2]. However, a lack of PL signal stability and limited solar cell efficiency is usually observed and attributed to the instability of the Si-H bonds on the PS surface that gradually break in air [2]. To resolve this problem materials like titanium oxide (TiO_2) are used for their passivation effect. TiO_2 thin films are currently used in the PV industry as standard AR coating on the vast majority of screen-printed solar cells. Titanium dioxide (TiO_2) is in fact a large band gap semiconductor with many interesting properties. It presents a high refractive index and a low absorption coefficient in visible light, which makes it an excellent optical coating material [3]. TiO_2 films have many other unique properties, which make them highly attractive for a variety of applications such as photovoltaic devices [4], gas sensors [5], electrochromic displays and photocatalysts [6]. The optical gap of TiO_2 (3.2 eV) belongs to the ultraviolet region. However, the peak of the solar spectrum is in the visible region. This mismatching limits the use of TiO_2 in photovoltaic applications. Many methods have been proposed to solve these problems, but doping TiO_2 with foreign ions, such as Fe, Cr and Ni, is one of the most promising strategies for sensitizing TiO_2 to visible light and also for forming charge traps to keep electron–hole pairs separate [7,8]. In photovoltaic, the ability of tuning the band-gap energy (E_g) of the absorbing films is of prime importance in order to cover the maximum of the solar spectrum. Titanium dioxide films have been prepared by various vacuum techniques such as chemical vapor deposition [6], pulsed laser deposition [9] and sputtering [10]. In this work, we report on the use of magnetron co-sputtering technique to achieve TiO_2: Cr films deposition on porous silicon (PS), where Cr content can be controlled at will. The structural and optical properties of the developed PS /Cr-TiO_2 films were investigated. The focus is put here on the effect of the Cr content of the TiO_2:Cr films on their passivation effects and on the optoelectronic properties of c-Si treated wafers. The obtained result is very promising for the improved use of c-Si in photovoltaic industrial application.

2. Experimental

Experiments were carried out on p-type c-Si wafer with a thickness of 500 µm and a resistivity in the order of 0.5−3 Ω cm. PS is formed by electrochemical anodisation method (EC). The EC attack was performed in ethanol hydrofluoric acid solution. The electrolyte composition, current density and anodisation time were set respectively to HF (48 wt. %): ethanol=1:4; 15 mA/cm^2 and 19 min. Immediately after PS formation, the samples were rinsed with DI water and dried under N_2 flux in order to prevent the PS film from flaking and deterioration. Pure TiO_2 and TiO_2: Cr thin films were deposited by means of RF-magnetron co-sputtering (13.56 MHz) technique on the PS layer. The substrates were mounted on a holder and placed at a distance of ~20 cm from the sputtering-target. The sputtering deposition chamber was first cryo-pumped to a base pressure of ~ 10^{-8} Torr, and then filled with a mixture of high purity Ar and O_2 gases (to a ratio of 80:20) to reach a working pressure of ~1.2 mTorr. Before deposition on substrates, the targets were cleaned by pre-sputtering for 15 min while keeping their shutters closed. To deposit TiO_2: Cr films, we have proceeded with the concomitant sputtering of both highly pure TiO_2 and

© Cognizure. All rights reserved.

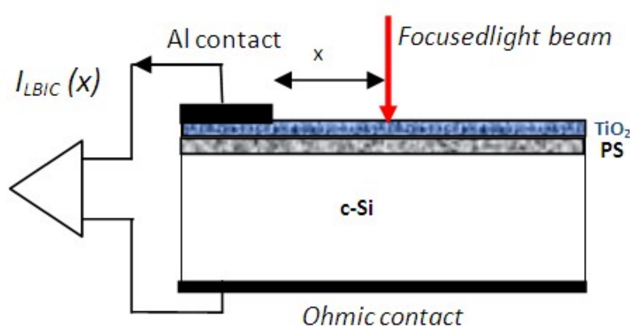

Figure 1. Sample design used for LBIC measurement.

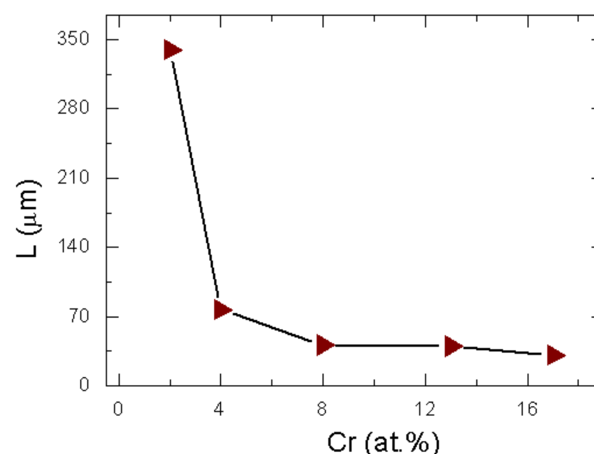

Figure 2. c-Si minority carrier diffusion length (L) as a function of Cr concentration (at. %). L for untreated c-Si and PS silicon treated sample is given for comparison.

Cr targets. To achieve an independent control of the Cr incorporation into the TiO_2: Cr films, the two targets were powered with two separate power sources. Indeed, while the TiO_2 target was powered with an RF power of 360 W, the Cr target was sputtered with variable power values (P_{cr}) ranging from 8 to 150 W. The Cr content increases with P_{cr} and could be varied from 2 to 17 at. % [11]. The deposition temperature was kept at ~550 °C and the sputtering time was set to 120 min. The thickness of the films, as estimated by means of calibrated quartz crystal microbalance and *ex-situ* measured by variable angle spectroscopic Ellipsometry (VASE) is in the range of 120 nm. The topography of the treat surfaces was investigated using AFM. The reflectance of the treated samples was measured in the 250 – 1200 nm wavelength range using a PerkinElmer Lambda 950 spectrophotometer equipped with an integrating sphere. The PL properties were measured using an Ar laser (λ = 488 nm) and detected by a cooled GaInAs detector with a standard lock-in technique. Finally the minority carrier diffusion length (L) of the active material was evaluated using the Light Beam Induced Current (LBIC) measurements on a Metal Insulator Semiconductor (MIS) type structure.

3. Results and Discussion

The minority carrier's diffusion length is one of the most important electrical parameters used in photovoltaic domain to quantify the optoelectronic quality of materials under study. As shown in Figure 1, the MIS device consists of an Al/Cr-TiO_2/PS/c-Si/Al type structure. The LBIC current is measured by scanning the laser beam c-Si close to the front Al metallic contact. The excitation spot is performed with the 633 nm wavelength of the He-Ne laser. At this wavelength the penetration depth of the beam is about 30 µm. The diffusion length L was estimated by fitting experimental LBIC measurements to theoretical ones using the following equation (1) [12, 13]:

$$I_{\mathrm{LBIC}}(x) = A \exp(-x/L)\, x^{-n} \qquad (1)$$

Where n is a constant which depends on the recombination velocity at the surface, and A is a constant which depends primarily on the beam intensity and the penetration depth. The n values are estimated according to the method reported in reference [13]. Figure 2 shows the values of diffusion length (L) depending on the concentration of the Cr. We observed decreases of the factor n from 1.5 for PS-treated c-Si to about 0.55 for PS/TiO_2-Cr (2 at. %) covered c-Si. This evolution is due to the reduction of recombination velocity at the c-Si surface as a consequence of the passivation effect of the used treatment. A strong improvement of the L from 100 µm for untreated c-Si to 180 after PS treatment and to 340 µm after PS/TiO_2-Cr (2 %.at) deposition is observed (Figure 2). When applying a pure TiO_2 film onto PS-treated c-Si, one would expect, at a first sight, that the enhancement of L could mainly be due to surface passivation through the reduction of the surface recombination velocity (S). However, the additional improvement of L observed for the TiO_2: Cr (2 at. %)/PS/mc-Si strongly suggests the possibility of a bulk passivation with the incorporation of the appropriate amount of Cr. This bulk passivation effect could be related to the incorporation of an optimal amount of Cr atoms and their chemical bonding with host matrix through Cr-Ti-O and Cr-Si-O type of bonding (and particularly at the grain boundaries, where the density of defects is high). This is consistent with the work of Hwang et al [14] who report that that TiO_2 passivation of PS helps to suppress unstable SiO_x and Si–O bond and re-constructed them into a more stable bond of Si–O–Si.

A clear evolution of the microstructure is observed with Cr content increases. From smooth surface for pure TiO_2 coating (Figure 3a) to non-porous fine granular structure for 4 at.% of Cr content and finally a rough and big size granular morphology for Cr content concentration ≥13 at.% Cr.

From the AFM surface morphology analysis of the PS and PS /Cr-TiO_2 surface, the RMS (Figure 3b) roughness is found to decrease from 514 nm for the former to 40 nm for the later. The decrease in the RMS roughness is attributed to Si pores filling by TiO_2 as already reported in the literature [15]. Figure 4 shows the total reflectance spectra evolution for a c-Si substrate after different treatments. These spectra show antireflection properties of the TiO_2: Cr/porous silicon. In the 350 - 700 nm wavelength range the reflectance is reduced from 35% for the untreated samples to a maximum of 13% for the coated ones. As confirmed by the AFM analysis, one can relate the decrease of the reflectance to the formation of rough ordered structure which is suitable for light trapping.

Figure 5 shows the PL spectra of TiO_2: Cr/porous silicon sample as a function of Cr concentration (at. %). The PL is intense, with a characteristic Gaussian-like spectrum. The maximum of the main PL peak is located between 550 and

© Cognizure. All rights reserved.

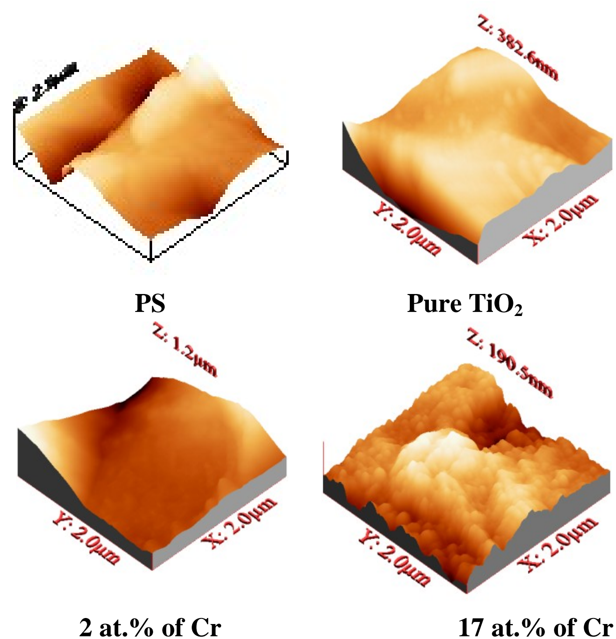

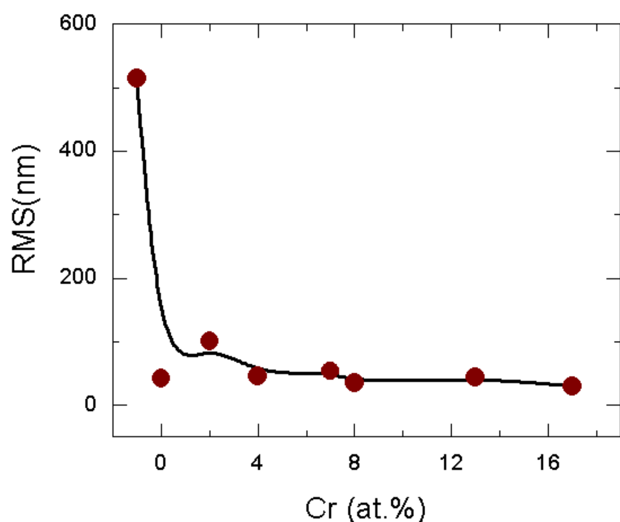

Figure 3. (a) AFM (3D) scans and (b) RMS of PS/TiO_2: Cr/c-Si samples as a function of Cr concentration (at. %).

700 nm and shows a FWHM around 1 eV. The maximum intensity of PL is obtained for the TiO_2-Cr (2.at %) concentration solution. The PL enhancement is due to surface passivation by Cr-TiO_2 layer. The passivation phenomena leads in fact to the decrease in the number of Si–H and Si–O–Si bonds and to the increase in the number of to more stable Si–Ti and Si-Cr bonds. As already reported PL can also be enhanced by filling the pores of PS with a conductive material [16]. Even if we do not have yet a clear cut interpretation of the origin of such passivation at the optimal Cr content, we do believe that this Cr content corresponds to the necessary amount of Cr atoms for the passivation of both TiO_2 and silicon through the formation of Cr-O-Ti and Cr-O-Si bonding.

For Cr concentration higher than 2 at. %, we observed a decrease of the PL peak intensity probably due to the creation of defects and impurities on silicon as previously reported by LBIC measurement (Figure 2).

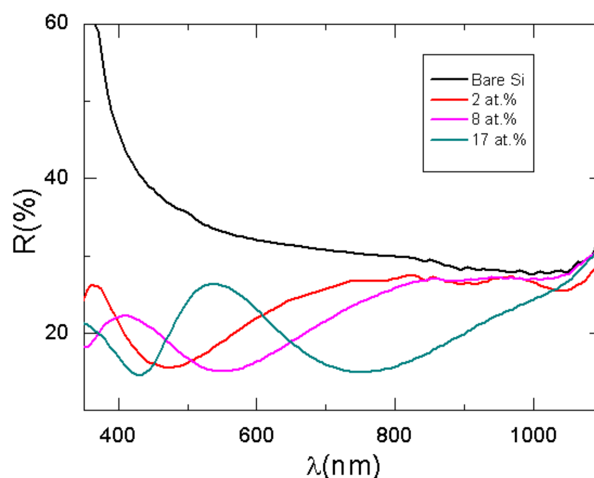

Figure 4. Influence of treatment on the total reflectivity as a function of Cr concentration (at. %).

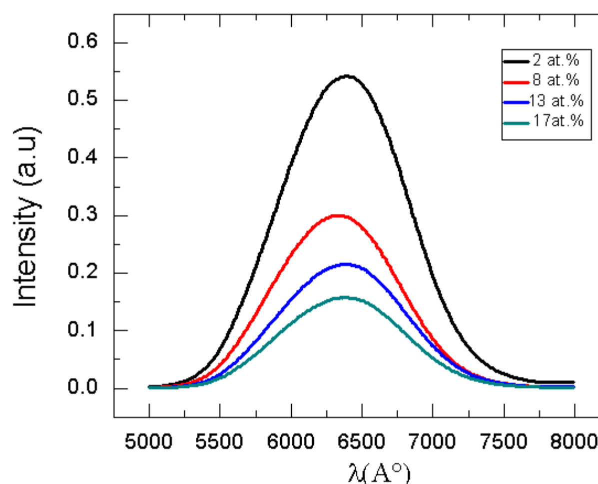

Figure 5. PL spectra of PS/TiO_2: Cr treated samples as a function of Cr content.

4. Conclusions

This study shows that Cr doped TiO_2 combined with PS is a good treatment to be used for c-Si passivation intended for solar cell application. It was demonstrated that the average total reflectivity decreases from 35% for untreated c-Si to 13% after TiO_2-Cr/PS treatment. From LBIC and PL analysis we confirmed that this combined treatment was very effective in improving the electrical and optical performances. As a result, the effective diffusion length was improved from 100 µm to 340 µm after Cr-TiO_2/PS treatment. The presence of an optimum Cr concentration has been experimentally confirmed at 2 at. %. At this point a strong enhancement is observed in the PL intensity and effective minority carrier diffusion length. The presented technique seems to be promising in c-Si solar cells manufacturing.

Acknowledgment

The authors (and particularly MAE) acknowledge financial support from both NSERC (the Natural Science and Engineering council) of Canada and from the FQRNT (le Fonds Québécois de la Recherche sur la Nature et les Technologies). The support from the Ministry of Higher Education and Scientific Research of Tunisia, is also acknowledged.

© Cognizure. All rights reserved.

References

1. R. Zhang, Y. Chen, Y. Zheng, and L. Chen, Chin. J. Lasers 36 (2009) 269.
2. V.Yu. Yerokhov and I.L Melnyk, Renew. sust. Energ. Rev. 3 (1999) 291.
3. L. Martinu, D. Poitras, J. Vac. Sci. Technol. A. 18 (2000) 2619.
4. S. Chatterjee, Sol. Energy 82 (2008) 95.
5. Ivano Alessandri , Elisabetta Comini , Elza Bontempi ,Guido Faglia , Laura E. Depero, Giorgio Sberveglieri , Sens. Actuators B 128 (2007) 312.
6. R. Dholam, N.Patel, M. Adami, A. Miotello, Hydrogen Energy 34 (2009) 5337.
7. Fujishima A, Zhang X, Tryk DA, Surf. Sci. Rep. 63 (2008) 515.
8. S.A. Campbell, H.S. Kim, D.C. Gilmer, B. He, T. Ma, W.L. Gladfelter, IBM J. Res. Dev. 43 (1999) 383.
9. Hua Long, Guang Yang , Aiping Chen, Yuhua Li, Peixiang Lu, Thin Solid Films 517 (2008) 745.
10. H. Tang, K. Prasad, R. Sanjines, P.E. Schmid, F. Levy, J. Appl. Phys. 75 (1994) 2042.
11. A. Hajjaji, M. Gaidi, B. Bessais and M. A. El Khakani, Appl. Surf. Sci. 257 (2011) 10351.
12. S.M. Davidson, C.A. Dimitriadis, J. Microsc 118 (1980) 275.
13. D.E. Ioannou, R.J. Gledhill, IEEE Trans. Electron Devices 30 (1983) 577.
14. J. D. Hwang and C. H. Chou, Appl. Phys. Lett. 96 (2010) 063503.
15. .N.V. Deshmukh, T.M. Bhave, A.S. Ethiraj, S.R. Sainkar, V. Ganeshan, S.V. Bhorasker, S.K. Kulkarni, Nanotechnology 12 (2001) 290.
16. Lang, W., Steiner, P. and Kozlowski, F., Porous silicon electroluminescent devices. J. Lumin. 57 (1993) 341.

Cite this article as:

Hajjaji *et al.*: **Effect of dual treatment based on porous silicon and sputter-deposited TiO_2 doped Cr film on the optoelectronic properties of monocrystalline Si .** ScienceJet 2012, **1**: 12

© Cognizure. All rights reserved.

Effect of double treatment based on porous Si and TiO_2 passivation on the optoelectronic properties of multicrystalline silicon substrates

N. Janene[a], A. Hajjaji[a,b], M. Ben Rabha[a], B. Bessais[a], M. A. El Khakani[b], M. Gaidi[a,*]

[a] *Photovoltaic Laboratory, Research and Technology Centre of Energy, Borj-Cedria Science and Technology Park, BP 95, 2050 Hammam-Lif, Tunisia*
[b] *Institut National de la Recherche Scientifique, INRS-Énergie, Matériaux et Télécommunications, 1650, Blvd. Lionel-Boulet, Varennes, Québec, Canada J3X 1S2*

[*] *Authors for correspondence: M. Gaidi, email: mounir.gaidi@crten.rnrt.tn*
M. A. El Khakani, email: elkhakani@emt.inrs.ca
Received 4 Feb 2012; Accepted 16 Apr 2012; Available Online 19 Apr 2012

Abstract

In this paper, we propose a novel passivation technique for multicrystalline silicon (mc-Si) wafers intended for solar cell applications. The new method combines the use of double treatment based on porous Si and TiO_2 passivation coating. Porous silicon (PS) was prepared by electrochemical anodization. TiO_2 nanoparticles were incorporated inside pores by the way of the pulsed laser deposition (PLD) technique with a thickness varying from 0.5 to 80 nm. The obtained nanocomposites were investigated for its passivation and antireflection properties. The combined treatment based on TiO_2/PS minimizes the average reflectivity from 30% for bare multicrystalline silicon to around 6% for the treated one. Depending on the TiO_2 nominal thickness a strong enhancement is observed on the photoluminescence intensity and on the effective minority carrier lifetime (τ_{eff}). As a consequence the τ_{eff} is improved from 2 µs for untreated sample to 319 µs after 0.5 nm TiO_2/PS treatment. A clear correlation between surface morphology evolution changes after each process and the minority carrier lifetime improvement is observed.

Keywords: Multicrystalline silicon; Porous silicon; Titanium dioxide; Lifetime minority carriers; Pulsed laser deposition

1. Introduction

Multicrystalline Si (mc-Si) wafers, used in solar cells fabrication, usually contain a large amount of impurities and defects, which could affect the minority carrier lifetime and thus cell efficiencies. In order to overcome this problem new process is needed to accomplish both surface and bulk passivation in mc-Si solar cells. SiN_x and SiO_2 treatments are usually used as a passivation coating [1,2]. They serve as AR coatings and provide surface and bulk passivation by allowing hydrogen diffusion into the device to passivate defects and impurities for improved device properties. Porous silicon (PS) has also been explored for its strong visible room-temperature photoluminescence (PL) and for its high potential in silicon photovoltaic application [3-5]. However, a lack of PL signal stability and limited cell efficiency is usually observed and attributed to the instability of the Si-H bonds on the PS surface that gradually break in air [4]. To resolve this problem materials like titanium oxide (TiO_2) are used for their passivation effect. TiO_2 thin films are used currently as the photovoltaic industry standard AR coating on the vast majority of screen-printed solar cells. [6,7]. TiO_2 coating of porous silicon is also found to reduce surface traps for charge carriers leading to an enhancement of the photoluminescence stability and optoelectronic properties of Si solar cell [8].

Titanium oxide films have been prepared by a variety of deposition techniques including chemical vapor deposition [9], sol gel processing [10], reactive sputtering [11, 12], and pulsed laser deposition (PLD) [13, 14]. Among these methods PLD seems to be a promoting technique to produce high quality thin films preserving the stoichiometry of multicomponent targets [15]. It presents several advantages including high deposition rate, flexibility in terms of deposition conditions, and good composition control [15]. Because of these numerous advantages, PLD has been shown to be particularly effective for the growth of nanostructured films. In the present work, we report on the structure, optical transmission, morphological, photoluminescence and minority carrier lifetime dependence on the nominal thickness of ultrathin films PLD-TiO_2 (from isolated nanoparticles, NPs, up to a 20 nm thickness) deposit on porous silicon (PS). The nominal film thickness was changed by increasing the number of laser ablation pulses. Interestingly, the thinnest films were found to give the highest PL intensity and a strong improvement of the minority carrier lifetime.

2. Experimental

The starting material was a p-type, boron-doped multicrystalline silicon substrate. The wafer has a thickness of approximately 400 µm and a resistivity ranging between 0.5 and 2.0 Ω*cm^{-1}. The porous layers were prepared by the electrochemical anodization technique, silicon substrate was used as the positive electrode and platinum wire mesh acted as the cathode. The electrolyte consists of 48% aqueous HF solution mixed with ethanol HF (48 wt. %): ethanol=1:4 and the current density was set to 20 mA/cm^2 for an etching time of 15 min. Immediately after PS formation, the samples were rinsed with DI water and dried under N_2 flux in order to prevent the PS film from flaking and deterioration.

A KrF excimer laser (wavelength = 248 nm, pulse durations of 12 ns) operating at a repetition frequency of 30 Hz was targeted at an angle of 45° on the rotating target TiO_2 (99.9% purity). The density of the target laser energy was set

© Cognizure. All rights reserved.

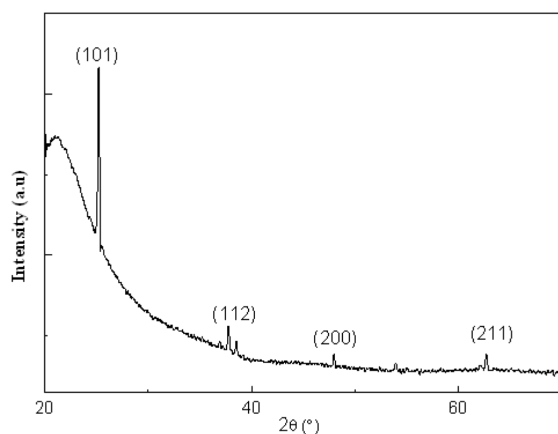

Figure 1. XRD patterns of TiO_2 thin film annealed at 500°C in oxygen for 60 min.

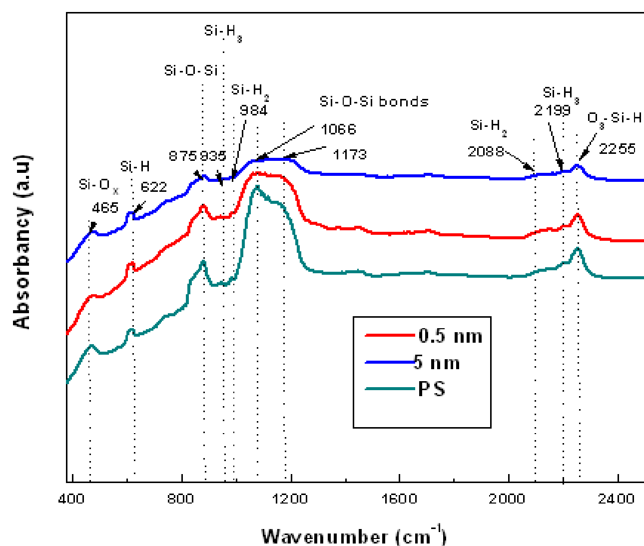

Figure 2. FTIR spectra of TiO_2/PS samples as a function of the TiO_2 nominal thickness.

at 4 J / cm ^{2}. TiO_2 thin films were deposited on two types of substrates, conventionally cleaned PS/Si and quartz. The substrates were mounted on a substrate holder and placed parallel to the target at a perpendicular distance of 5 cm. During the deposition step, the substrate holder was rotated in order to ensure a good uniformity of the film thickness. The TiO_2 depositions were carried out at room temperature under 10 mTorr of oxygen background pressure. The chamber was first turbo pumped to about 10^{-5} Torr before filling it with oxygen. Prior to deposition, the TiO_2 target was systematically cleaned by laser-ablating its surface for 10 min while the substrate was shielded from the ablation plume by a shutter. The nominal film thickness was varied from 0.5 nm to 80 nm by increasing the number of laser ablation pulses from 50 to 8000. The nominal TiO_2 film thickness (t) was obtained by multiplying the number of laser pluses by the average deposition rate (nanometer/pulse) derived from the deposition of a sufficiently thick film (150 nm) which thickness was directly measured from cross section scanning electron microscopy observations.

The crystallographic structure was examined by means of x-ray diffraction (XRD) technique using a Philips X'pert-MPD X-ray diffractometer (Cu K_α radiation). The surface morphology of the treated surfaces was investigated by atomic force microcopy (AFM). The band-gap energy of TiO_2 films were derived from the optical transmittance spectra $T(\lambda)$ measured on films deposited directly on quartz substrate. The spectrophotometric measurements of $T(\lambda)$ and reflectance $R(\lambda)$ were obtained in the 250 – 1200 nm wavelength range using a PerkinElmer Lambda 950 spectrophotometer equipped with an integrating sphere. The effective minority carrier lifetimes (τ_{eff}) were measured by photoconductance technique (WCT-120). The PL properties were measured using an Ar laser (λ = 488 nm) and detected by a cooled GaInAs detector with a standard lock-in technique.

3. Results and Discussion

Figure 1 shows typical XRD patterns of the 80 nm thick TiO_2 films deposited on quartz after annealing at 500°C for 60 min. The XRD peaks fits with those of TiO_2 in the anatase phase. The crystallite size is estimated to be 35 nm by using the Debye-Scherer formula. For ultrathin TiO_2 films with nominal thickness ranging of 0.5 nm to 5 nm the XRD diffraction signal is hardly detectable. This is indicative of the small amount of TiO_2 together with the small crystallite size (1-3 nm). No XRD peaks corresponding to TiO_2 phase are observed before annealing which is related to the presence of TiO_2 in an amorphous phase.

The FTIR spectra of the TiO_2/PS samples with different TiO_2 layer thicknesses are displayed in Figure 2. The two absorption bands centered around 935 and 984 cm^{-1} are attributed respectively to Si– H_3 and Si– H_2 vibration modes [16-18], while the absorption bands at 2254 cm^{-1} are attributed to Si–H stretching modes [18]. The FTIR spectra clearly show that the intensities of both the two Si–H_x absorption bands are decreased by increasing the TiO_2 film thickness. The intensity decreases of the Si–H absorption bands after TiO_2 coating is related to the destruction of the Si–H bonds leading to Si-Ti bond formation. On the other hand, the broad absorption band in the wavelength range from 1066 to 1173 originating from asymmetric stretching of Si–O–Si could be attributed to oxidation of PS [17, 19]. The FTIR spectra demonstrate that the intensity of the absorption band for the Si–O–Si bonds is also decreased after TiO_2 film deposition. Native oxides exist at the surface of PS by the reaction between Si atoms at the PS surface and oxygen molecules in air, so to call, natural oxidation. The native oxides will be reduced to Si atoms and the Si atoms will make bonds with Ti atoms.

Figure 3a shows the optical transmittance spectra T(λ) of the TiO_2 films. The transmittance spectra present a well-pronounced fundamental absorption, in the energy range depending on TiO_2 nominal film thickness (i.e, TiO_2 NP size). The maximum transmittance decreases as the TiO_2 nominal film thickness increases. These $T(\lambda)$ spectra were analysed following the Tauc plot method [20], and their band-gap energies estimated accordingly (Figure 3b). Comparison between the various band-gaps (Figure 2b) shows that the optical absorption properties are significantly affected by the nominal thickness of the TiO_2 films and thereby by the TiO_2 NPs size. The band-gap values are quite larger than the typical value quoted for bulk TiO_2 (3.2 eV). This band-gap broadening can be accounted for the quantum confinement

© Cognizure. All rights reserved.

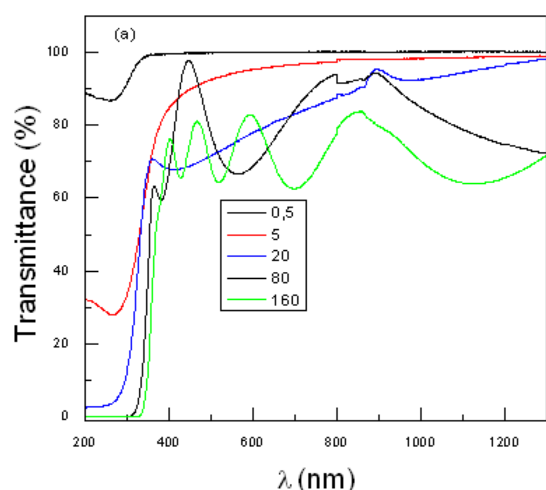

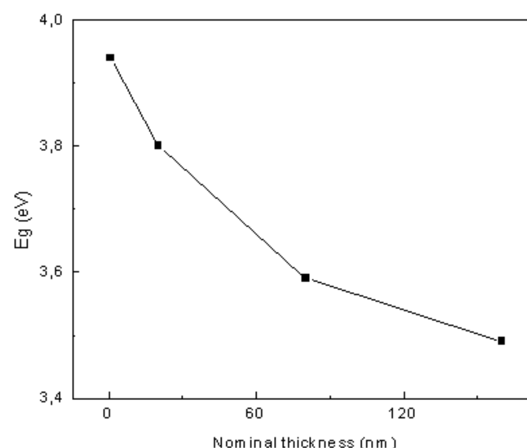

Figure 3. (a) Optical transmission and (b) band-gap evolution as a function of TiO_2 nominal thickness (nm).

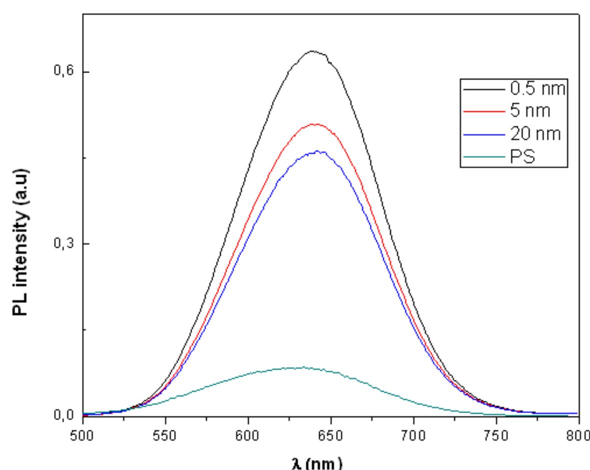

Figure 4. PS PL spectra as a function of TiO_2 nominal thickness.

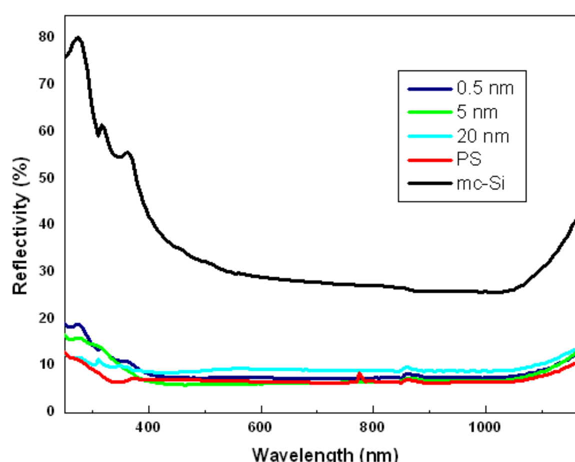

Figure 5. Effect of TiO_2 nominal thickness (nm) on the total reflectivity. Reflectivities of PS treated sample and for untreated mc-Si are reported for comparison.

effects as the TiO_2 films are expected to be composed by a very small NP size (in the range of nm).

Figure 4 shows room temperature PL spectra of PS versus film thickness of TiO_2. The photoluminescence spectrum presents a strong correlation between the PL intensity and the TiO_2 nominal thickness. We may extract a conclusion from the above discussion (FTIR measurement) that enhancement in the PL intensity of PS by depositing TiO_2 film on the PS is related to the decrease in the number of Si–H and Si–O–Si bonds and to the increase in the number of Si–Ti bonds. Therefore, the PL of the PS will be enhanced by deposition of a TiO_2 as previously reported by Sun et al [21]. On the other hand, the PL intensity tends to increase as the transmission increases. In comparison with the number of Si–O bonds in the TiO_2 (5nm)/ PS sample with that of the TiO_2 (0.5nm)/PS sample, we can conclude that the former is larger than the latter. However, the transmittance of the TiO_2 (5nm)/ PS sample is lower than that of the TiO_2 (0.5nm)/ PS. The enhancement observed in the PL intensity for the 0.5 nm TiO_2 coated PS is then the result of passivation effect and high optical transmittance.

Figure 5 shows the total reflectance spectra evolution for a mc-Si substrate for different treatments. These spectra show antireflection properties of the TiO_2/porous silicon. In the 350 - 1000 nm wavelength range the reflectance is reduced from 30% for the untreated samples to 6% for the sample coated with TiO_2/porous silicon. As shown in the AFM images (Figure 6), one can relate the decrease of the reflectance to the formation of rough ordered structure suitable for light trapping.

The effect of TiO_2 nominal thickness is also observed on the minority carrier lifetime (τ_{eff}). The evolution of, τ_{eff}, as a function of treatment is presented in Table 1. The results indicate a strong improvement in this parameter compared to the value obtained from the mc-Si. In fact, the lifetime increases from 2 µs for the untreated mc-Si to 319 µs for 0.5 nm TiO_2/porous Si treated one. Thickness higher than 5 nm leads to a decrease in lifetime. This improvement could be attributed to surface passivation, and to the reduction of

© Cognizure. All rights reserved.

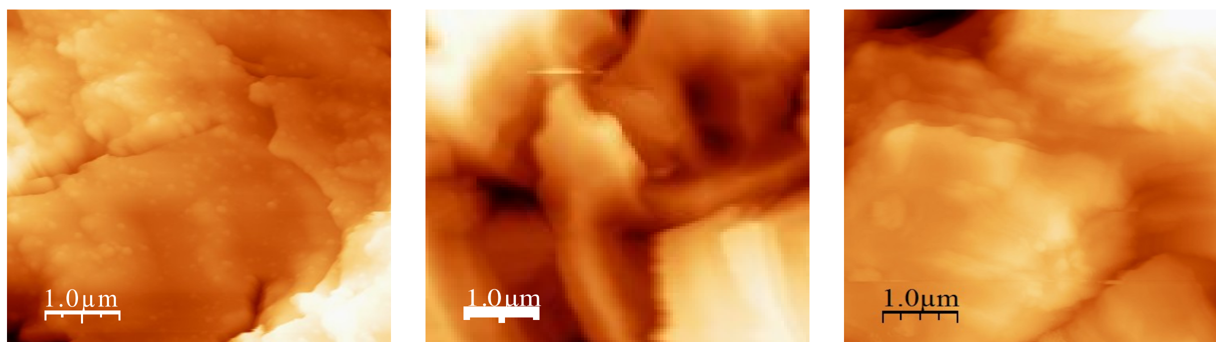

Figure 6. AFM micrograph images of 0.5 thick TiO_2 film on PS. AFM images for bare mc-S and PS/mc-Si are reported for reference.

Table 1. Evolution of effective minority carrier lifetime of mc-Si after different treatments. Measured at a minority carrier density (Δn) of $4x10^{14}$ cm^{-3}.

Sample	Bare mc-Si	PS	TiO_2 (0.5 nm) /PS	TiO_2 (5 nm) /PS	TiO_2 (20 nm)/ PS
τ_{eff} (µs)	2	40	319	165	3,4

surface recombination velocity due to a dual treatment based on combined TiO_2/porous silicon treatment.

4. Conclusions

In this work, we have demonstrated the beneficial effect of a double treatment based on TiO_2/PS on the optoelectronic properties of mc-Si. As a result the average reflectivity decreases from 30% for untreated sample to less than 6% for the treated one. For ultrathin TiO_2 film deposition a strong enhancement in the PS PL intensity is observed combined to a high effective minority carrier lifetime of the treated mc-Si. The experimental results enable us to conclude to the presence of an optimal TiO_2 nominal thickness leading to a high passivation effect.

References

1. G. Dingemans, M. M. Mandoc, S. Bordihn, M. C. M. van de Sanden and W. M. M. Kessels, Appl. Phys. Lett. 98 (2011) 222102.
2. H. Mäckel and R. Lüdemann, J. Appl. Phys. 92 (2002) 2602.
3. L. T. Canham, Appl. Phys. Lett. 57 (1990) 1046.
4. V.Yu. Yerokhov and I.L Melnyk, Renew. Sust. Energ. Rev. 3 (1999) 291.
5. M. Ben Rabha , B. Bessaıs, Sol. Energy 84 (2010) 486.
6. L. Martinu, D. Poitras, J. Vac. Sci. Technol. A 18 (2000) 2619.
7. S. Chatterjee, Sol. Energy 82 (2008) 95.
8. K.J. Kim, G.S. Kim, J. S. Hong, T.S. Kang and D. Kim, Sol. Energy 64 (1998) 61.
9. Abbas Hodroj, Odette Chaix-Pluchery, Marc Audier, Ulrich Gottlieb and Jean-Luc Deschanvres, J. Mater. Res. 23 (2008) 755.
10. W.F.Zhang, M.S. Zhang and Z.Yin, Phys. Status Solidi A 179 (2000) 319.
11. A. Dakkaa, J. Lafaitb, M. Abd-Lefdila and C. Sellab, M. J. Condens. Matter 1 (1999) 2.
12. A. Labidi , M. Gaidi , J. Guérin , A. Bejaoui , M. Maaref , K. Aguir, Thin Solid Films 518 (2009) 355.
13. Paul F. Ndione, Mounir Gaidi, Christophe Durand, Mohamed Chaker, Roberto Morandotti, and Grégory Rioux, J. Appl. Phys. 103 (2008) 033510.
14. A. Amassian, M. Gaidi and M. Chaker, L. Martinua, J. Vac. Sci. Technol. 24 (2006) 1.
15. M. Gaidi M. Chaker, P. F. Ndione, and R. Morandotti, B. Bessaïs, J. Appl. Phys. 101 (2007) 063107.
16. Walter Jaimes Salcedo, Francisco J. Ramirez Fernandez, Elisabete Galeazzo, Braz. J. Phys. 27 (1997) 158.
17. Chanseok Hong, Hohyeong Kim, Sunghoon Park, Chongmu Lee, J. Eur. Ceram. Soc. 30 (2010) 459.
18. Hohyeong Kim, Chanseok Hong, Chongmu Lee, Mater. Lett. 63 (2009) 434.
19. Z.H. Xiong , L.S. Liao, S. Yuan, Z.R. Yang, X.M. Ding, X.Y. Hou, Thin Solid Films 388 (2001) 271.
20. J. Tauc, R. Grigorovici, and A. Vancu, Phys. Status Solidi 15 (1966) 627.
21. J. Sun, X. Han, X.W. Du and Y.W. Lu, Mater. Lett. 59 (2005) 3135.

Cite this article as:

N. Janene *et al.*: **Effect of double treatment based on Porous Si and TiO_2 passivation on the optoelectronic properties of multicrystalline Silicon substrates.** ScienceJet 2012, **1**: 13

© Cognizure. All rights reserved.

An alternative explanation for the effect of Ge content on the density of end-of-range defects found in ion implanted relaxed SiGe alloys

A. Belafhaili[a,*], L. Laânab[a], P. F. Fazzini[b], F. Cristiano[b], N. Cherkashin[c], G. Benassayag[c], A. Claverie[c]

[a] LCS, Faculty of Sciences, Mohammed V University, Rabat, Morocco
[b] LAAS/CNRS, 7 Av de Col Roche 31077, Toulouse Cedex, France
[c] CEMES/CNRS and Université de Toulouse, BP 4347, F-31055 Toulouse Cedex, France

*Authors for correspondence: A. Belafhaili, email: aminebela@hotmail.com
Received 4 Feb 2012; Accepted 27 Apr 2012; Available Online 28 Apr 2012

Abstract

This work presents a study of an influence of the Ge content in relaxed SiGe alloys on the populations of end-of-range defects created by amorphizing ion implantation and annealing. For this, several relaxed layers of the alloy with variable Ge concentrations were grown by chemical vapor deposition, preamorphized by Ge^+ ion implantation, and subsequently annealed at 680°C. Identification of the defect types was realized by transmission electron microscopy under appropriate imaging conditions. These defects mostly consist of small (~ 10 nm long) interstitial {113} defects. Their density decreases along with the total number of atoms they contain for increasing Ge contents. Comparing our data with Monte Carlo simulations, we conclude that this effect for increasing Ge contents can be, for a large part, explained by the decrease of an excess of interstitials generated during amorphization beneath the crystal to amorphous (c/a) interface and by the increased diffusivity of self-interstitials in SiGe alloys.

Keywords: Ion implantation; Amorphization; End-of-range defects; TEM; Monte Carlo simulation; Interstitials

1. Introduction

To produce the abrupt ultra-shallow junctions required by ultimate CMOS technology, a preamorphization step consisting of a high dose Ge implant is often necessary before dopant implantation. However, during dopant activation annealing, End-Of-Range (EOR) defects form in the region located just beneath the former crystal to amorphous interface. These defects are at the origin of diffusion anomalies [1] and increase the junction leakage currents by introducing electrically active deep levels in the bandgap of Si [2-4]. The origin and thermal evolution of these defects have been recently understood and modeled [5] in silicon.

However, while SiGe alloys, relaxed or strained, are now used as “starting materials” for the fabrication of CMOS, too little is known on the behavior of these defects in such alloys during activation annealing. This hampers the possibility to simulate and optimize process conditions for optimum devices. Crosby et al. [6] have studied defect transformation and discussed the relative stability of these defects in Si and SiGe alloys while Fazzini et al. [7] noticing the same thermal behavior have interpreted their results invoking the enhanced interstitial self-diffusivity in Ge-rich alloys. In this context, the goal of this work is to bring new data proposing an alternative explanation for the apparent differences of thermal behavior between interstitial defects in Si and SiGe alloys.

1.1. Evolution of interstitial defects in Si

Ion implantation results in the creation of large concentration of interstitials and vacancies which, during annealing, tend to recombine and eventually condense to form various types of defects. After amorphizing implants, only the point defects left below the c/a interface participate in these annihilation/recombination processes, until only the interstitials in excess to the vacancies condense into interstitial precipitates [8]. As the annealing proceeds, these precipitates evolve from clusters (not seen by TEM) of 4 then 8 Si atoms [9] to the rod-like {113} defects [10, 11]. For “mild” annealing, clusters and {113} defects may coexist and the later become predominant when increasing the annealing time. For higher thermal budgets, these defects ultimately transform into two types of dislocation loops [12-14]. It has been ascertained that the various types of defects grow in size then change their structure by passing from one species to the other following an Ostwald ripening mechanism [13, 14] where the driving force is the decrease of the formation energy of the defect as they grow in size or change structure. Finally, it has to be noted that all this formalism has been recently injected into commercial process simulators and allows for the accurate simulation of the transient anomalous diffusion of dopants in Si [15].

For this study, annealing was intentionally performed at a relatively low temperature for which, in pure silicon, only {113} defects are observed by TEM. {113} defects are almost one-dimensional precipitates, well-known to the TEM community as ‘rod-like’ defects. They are formed by the agglomeration of di-interstitials, have a {113} habit plane and are elongated along a direction <110> with a Burgers vector of a/25 <116>. There are twelve variants of these defects from which 1/3 lies parallel to a {100} wafer surface. Because of their large formation energy [11, 16], i.e. their relative instability, these defects may dissolve before transforming into dislocation loops when located close to the surface of the wafer by transferring the interstitials they are composed of towards the surface where they annihilate [10,11,17].

© Cognizure. All rights reserved.

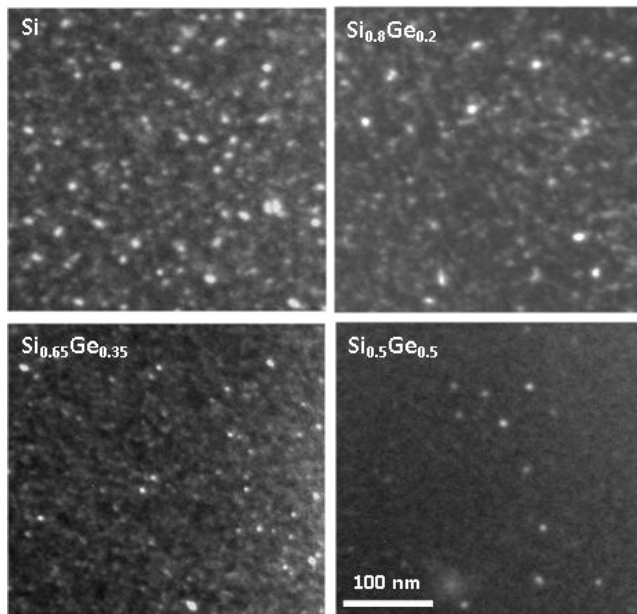

Figure 1. Plane view TEM micrographs (WBDF, B= [11$\bar{3}$], g= [422]) showing the variation of the {113} defects density and sizes, in the relaxed $Si_{1-x}Ge_x$, with the Ge content (x= 0; 0.2; 0.35 and 0.5). The samples were preamorphized by Ge^+ (35 keV, 1×10^{15} cm^{-2}) implantation and annealed at 680°C for 100s.

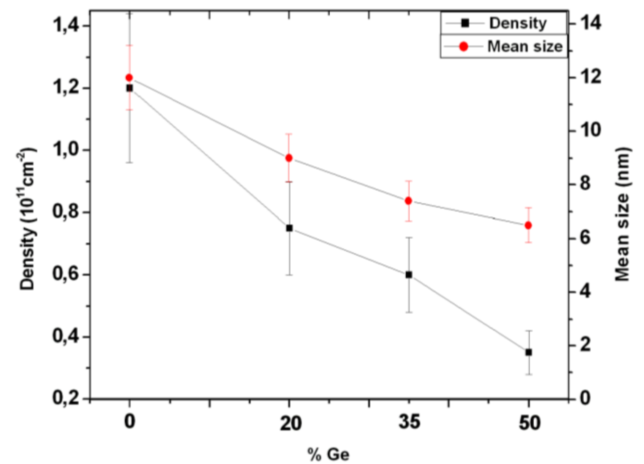

Figure 2. The {113} defects density and the mean size as a function of the Ge content for the samples of the Figure 1.

2. Experimental details and simulations

Fully relaxed SiGe alloy layers (1 μm thick) with increasing Ge content (0, 20, 35 and 50%) were grown by Chemical Vapour Deposition (CVD). These wafers were grown via a compositionally graded buffer layer in which the Ge is incorporated into the sample at an increasing rate of 10% Ge/μm. Pieces of these wafers were amorphized by Ge^+ implantation at 35 keV and with a dose of 1×10^{15} cm^{-2} then annealed at 680°C, for 100 s. Samples were then prepared by mechanical polishing and subsequent argon ion thinning until electron transparency for cross-sectional and plan-view observations. Transmission Electron Microscopy analysis was performed using a 2010-JEOL microscope in Weak Beam Dark Field (WBDF) mode to measure defect depths, densities and sizes. All observations have been carried out close to a B=<113> zone axis with a diffraction vector g=<422>. Under such conditions, defects contrast analysis shows that the majority of defects (about 83%) are visible by TEM [18]. From each TEM micrograph we obtain the projection of the defects on the image plan. To determine the mean size of defects, we multiply the size measured on the TEM images for each variant by their projection factor to go up to the real size, after we determine the mean size of defects.

The simulation of EOR defects formation is based on the 'excess interstitial' model [8] which has been tested in many cases [19- 21]. This model assumes that EOR defects are due to the clustering of atoms which survive the annihilation by thermal recombination with all the vacancies available beneath the c/a interface. The excess interstitial distribution is deduced from the well-known Monte Carlo (Stopping and Range of Ions in Matter) SRIM code in the full-cascade option. This program, developed by Ziegler et al. [22], computes by means of a Monte Carlo procedure the energy losses as well as the scattering of the charged particles along their paths. Once all events have been simulated, the code generates files containing data on energy deposition, radiation damage, ions, recoils and vacancies distributions.

3. Results and Discussion

In Figure 1, four plan-view WBDF micrographs show the changes of defect populations as a function of the Germanium content in the layers. After such a low budget thermal annealing, only very small (<10 nm) {113} defects are observed. It is clearly seen that both the density and the mean size of the defects decrease when the Ge content increases. The result of the quantitative analysis of such TEM images is graphically summarized in Figure 2. This graph shows that the {113} defect density decreases from about 1.2×10^{11} cm^{-2} to 3×10^{10} cm^{-2} while their mean size decreases from 12 nm to 6.5 nm when varying the Ge content from 0 to 50%. Knowing the density, the size distribution and the exact crystallographical features of these defects, it is possible to deduce, from plane viewTEM images, the areal density (cm^{-2}) of self-interstitials (noted N_b) stored in the {113} defects. This areal density is given by

$$N_b = d_{\{113\}}.L_{moy}.d_{tot}.W_m$$

Where $d_{\{113\}}$ is the atomic density in the {113} plane, L_{moy} is the mean length of {113} defects, d_{tot} is the areal density of {113} defects and W_m is the mean width of the {113} defects, usually taken as a constant equal to 4 nm [10, 18].

The variation of N_b with the Ge content is plotted in Figure 3. This figure shows that the number of atoms stored in the {113} defects decreases by a factor of 5 when passing from pure Si to $Si_{0.5}Ge_{0.5}$.

Cross- sectional TEM images of the same samples show that the depth-position of the defects is approximately the same for all Ge compositions [7], suggesting that the c/a interface are also located at the same depth-position after implantation, whatever the Ge content.

In the preceding studies [7], the authors have compared the evolutions of the different types of defects which were observed for sensibly larger annealing times and/or temperatures than used here. In our case, we observe only one type of defect, namely the {113}'s, whatever the Ge content in the layers. Thus, we first focus our attention on the dependence of the areal density of interstitials stored in these defects upon Ge content, as represented in Figure 3.

© Cognizure. All rights reserved.

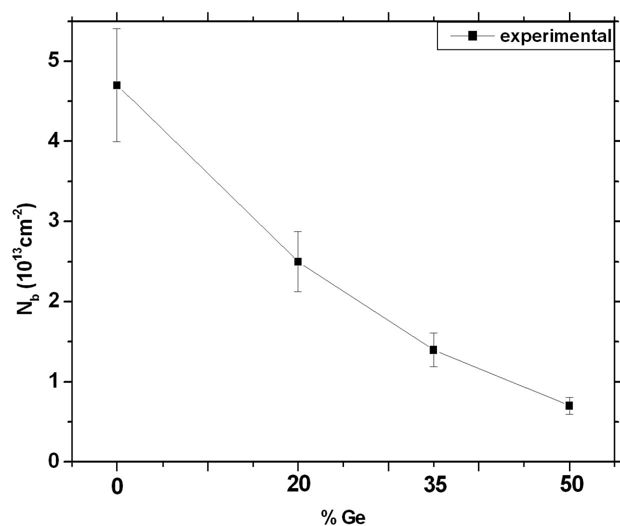

Figure 3. The measured concentration of trapped interstitials in the whole defect population as a function of the Ge content.

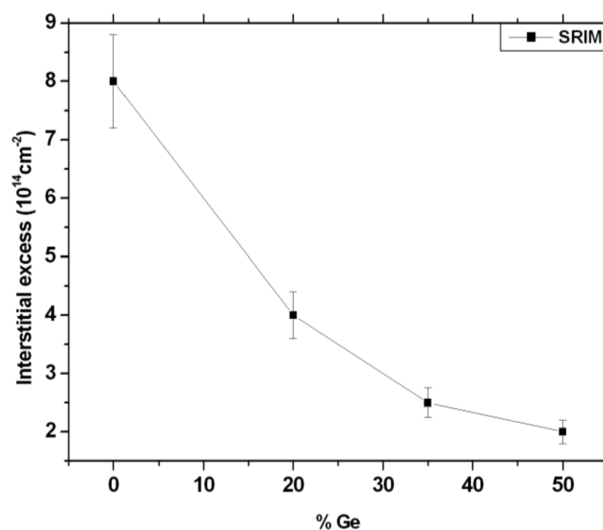

Figure 4. The excess interstitials below the c/a interface, calculated by SRIM code, as a function of the Ge content.

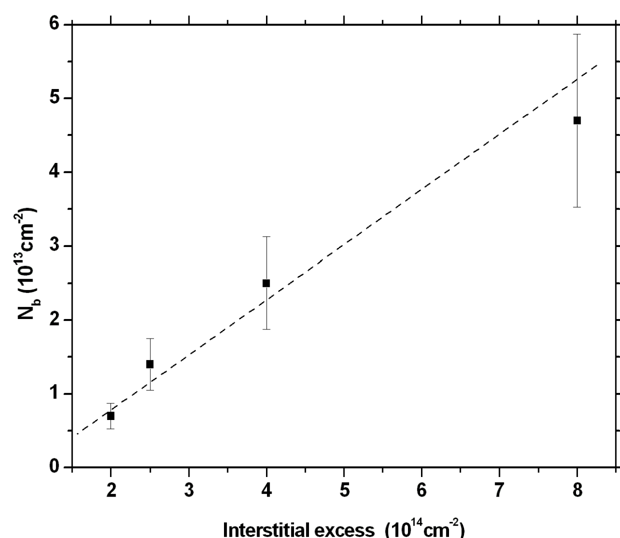

Figure 5. The concentration of trapped interstitial in {113} defects (extracted from TEM images) as function of the concentration of excess interstitials (calculated by SRIM).

Before invoking the "chemical effects", linked to the large differences in the formation energies of the defects in Si and SiGe, or the "surface effects", associated with the larger diffusivity and recombination efficiency of Si interstitials at the surface for SiGe alloys [7], we recall that the origin of these defects is principally attributed to the high concentration of "excess interstitials" which can be found beneath the c/a interface immediately after implantation. Indeed, all vacancies and interstitials initially created by the slowing down of the ions recombine during annealing. These recombination taking place much faster than the solid phase epitaxy of the amorphous layer and the self-diffusivity of Si being smaller in amorphous Si than in the crystal, the defects, which form by agglomeration of these excess interstitials, stay located below the original interface, as experimentally observed [23]. It has been shown that this explanation could quantitatively account for the changes in defect densities and sizes observed when varying the implantation energy, dose and even temperature in Si [19-21]. Moreover, it has been demonstrated that the total number of atoms bound to the defects was always proportional to the number of excess interstitial atoms left behind the interface, as calculated using the SRIM code [22] and provided that surface recombinations were negligible. This model has received the name of "excess interstitial" model [8,24] and is also now integrated into modern process simulator software [25].

Thus, it is quite natural to check whether or not the same model could explain alone or in part the influence of Ge content onto the defect populations. For this, we have computed the number of ions, of recoil atoms and of vacancies left beneath the c/a interface using the SRIM code. As in our previous work [20, 8], the number of "excess interstitials" left beneath the interface is obtained by subtracting the number of vacancies from the number of interstitials. Because of the low probability associated with particles reaching the deep crystalline region beneath the c/a interface, as many as 1×10^5 ions are necessary to reach a good statistical representation of the different species in this region. Displacement energies of 15 eV and 30 eV for Silicon and Germanium atoms were used in the SRIM program, respectively [26].

The variations of the calculated areal density of excess interstitials left beneath the c/a interface, assumed to be at a constant depth of 60 nm, is presented in the Figure 4 as a function of Ge content. Interestingly, it decreases with the Ge content.

Combining the experimental and simulation results in Figure 5, it appears that the areal density of interstitials stored in the {113} defects is a smooth monotonic, almost linear, function of the areal density of interstitials generated by the bombardment and that survive thermal recombination, as calculated by SRIM. Thus, the most obvious change in defect populations due to the increase of the Ge content in the SiGe layers can be explained through collisional arguments only. The number of interstitials stored in the defects, after moderate annealing, decreases when the Ge content in the layer increases. This behavior, observed also in simulations, can be simply explained through the increasing stopping power of the recoil atoms as the average mass, i.e. Ge content in the layer, increases.

© Cognizure. All rights reserved.

The same phenomenon has been previously invoked in silicon to explain the variation of EOR defects populations with ion beam energy [21] after amorphizing implants. In that case, it was observed that the defects always contained much less interstitials when the implant energy was reduced. It was further shown that this observation could be quantitatively explained by considering that the beam energy reduction resulted in the injection of a smaller density of self-interstitials beneath the c/a interface. In both cases, the same argument holds, the heavier, in the LSS (Lindhard, Scharff and Schiott) terminology [27] the ion, the smaller the density of the interstitial injected beneath the c/a interface, which is the origin of the EOR defects, becomes.

Finally, we get back to the populations characteristics themselves i.e., the average sizes and densities of the defects. It is known from the Ostwald ripening theory of precipitates that a change of the initial supersaturation (here the density of excess interstitials) before annealing results in a change of their density but not of their size (size invariant). This has been experimentally confirmed in the case of As precipitates in GaAs [28] but also in the case of EOR defects [29]. Thus, the change of defect density we have experimentally observed in the present study can be directly explained by this characteristic. However, the decrease of defect size observed for increasing Ge content cannot be explained through collisional arguments. In this case, the only explanation is that the defects are dissolving during annealing (non conservative Ostwald ripening) and that they dissolve faster when the Ge content increases. There, we meet again the arguments proposed by Fazzini [7] and Crosby [6]. Indeed, this increased dissolution rate can be due only to three possibilities or any combination of these three, i) a lower binding energy of the atoms to the defects, ii) a larger diffusivity of the interstitials and/or iii) a larger recombination efficiency of the interstitial at the wafer surface, when the Ge content increases. While the hypothesis i) and iii) are uncertain, the increased diffusivity of self-interstitial atoms in SiGe alloys is a proven fact [7].

4. Conclusions

In this work we have studied by TEM the influence of the Ge content on the populations of end-of-range defects created by amorphizing ion implantation in relaxed SiGe alloys followed by annealing at 680 °C for 100 s. Increasing the Ge content results in a net reduction of both the density and of the size of the EOR defects. We show that the density of interstitials contained in the defects after such a short and low temperature annealing is a quasi linear function of the density of excess interstitials generated by the amorphizing implant, initially located beneath the c/a interface. Thus, we suggest that collisional arguments can explain for a large part the observed difference. However, the observed reduction of the mean size of the defects for increasing Ge content cannot be explained from this argument. It is thought that this characteristic must be ascribed to the much larger diffusivity of self-interstitials atoms in SiGe alloys which favors the faster dissolution of the defects through the recombination of these interstitials at the wafer surface.

References

1. J. Liu, V. Krishnamoorthy, H. J. Gossman, L. Rubin, M. E. Law, K. S. Jones, J. Appl. Phys. 81 (1997) 1656.
2. D. Girginoudi and C. Tsiarapas, Nucl. Instrum. Meth. B. 266 (2008) 3565.
3. M. Minondo, J. Boussey, G. Kamarinos, Microelectron. Reliab. 37 (1997) 53.
4. H. L. Liu, S. S. Gearhart, J. H. Booske, W. Wang, J. Electron. Mater. 27 (1998) 1027.
5. S. Boninelli, N. Cherkashin, A. Claverie and F. Cristiano, Nucl. Instrum. Meth. B. 253 (2006) 80.
6. R. Crosby, J. Frazer, Dr. K. S. Jones, Dr. M. E. Law, A. N. Larsen, J. L. Hansen, Materials Research Society Symposium Proceedings Vol. 717 (2002).
7. P. F. Fazzini, F. Cristiano, E. Talbot, G. Benassayag, S. Paul, W. Lerch, A. Pakfar, J. M. Hartmann., Thin Solid Films 518 (2010) 2338.
8. L. Laânab, C. Bergaud, MM. Faye, J. Fauré, A. Martinez and A. Claverie,Materials Research Society Symposium Proceedings Vol. 279 (1993) 381.
9. N. E. B. Cowern, G. Mannino, P. A. Stolk, F. Roozeboom, H. G. A. Huizing, J. G. M. van Berkum, F. Cristiano, A. Claverie, M. Jaraíz, Phys. Rev. Lett. 82 (1999) 4460.
10. D. J. Eaglesham, P. A. Stolk, H. J. Gossmann, J. M. Poate, Appl. Phys. Lett. 65 (1994) 2305.
11. A. Claverie,B. Colombeau, B. De Mauduit, C. Bonafos, X. Hebras, G. Benassayag, F. Cristiano, Appl. Phys. A 76 (2003) 1025.
12. B. de Mauduit, L. Laânab, C. Bergaud, M. M. Faye, A. Martinez and A. Claverie, Nucl. Instrum. Meth. B. 84 (1994) 190.
13. C. Bonafos, D. Mathiot, A. Claverie, J. Appl. Phys. 83 (1998) 3008.
14. F. Cristiano, J. Grisolia, B. Colombeau, M. Omri, B. de Mauduit, A. Claverie, L. F. Giles, N. E. B. Cowern, J. Appl. Phys. 87 (2000) 8420.
15. P. Pichler, C. J. Ortiz, B. Colombeau, N. E. B. Cowern, E. Lampin, S. Uppal, M. S. A. Karunaratne, J. M. Bonar, A. F. W. Willoughby, A. Claverie, F. Cristiano, W. Lerch, S. Paul, PhysicaScripta T126 (2006) 89.
16. S. Takeda and M. Kohyama, Philos. Mag. 44 (1993) 101.
17. Y. lamrani, F. Cristiano, B. colombeau, E. Scheid, P. Calvo, H. Schafer, A. Claverie, Nucl. Instrum. Meth. B. 216 (2004) 281.
18. P. Calvo, A. Claverie, N. Cherkashin, B. Colombeau, Y. Lamrani, B. de Mauduit, F. Cristiano, Nucl. Instrum. Meth. B. 216 (2004) 173.
19. L. Laanab, C. Bergand, C. Bonafos, A. Martinez, A. Claverie., Nucl. Instrum. Meth. B. 96 (1995) 236.
20. L. Laânab, A. Martinez, A. Essaid, C. Bonafos, and A. Claverie, Annales de. Chimie Fr. 19 (1994) 459.
21. L. Laânab, B. Colombeau, C. Bonafos, and A. Claverie, J. Phys. IV France 123 (2005) 345.
22. J. F. Ziegler, J. P. Biersack, U. Littmark, The Stopping and Range of Ions in Solids, Pergamon Press, New York (1985).
23. E. Lampin, V. Senez and A. Claverie, J. Appl. Phys. 85 (1999) 8137.
24. A. Claverie, C. Bonafos, D. Alquier, A. Martinez, Solid State Phys. V47–48 (1996) 195.
25. E. Lampin, C. J. Ortiz, N. E. B. Cowern, B. Colombeau, F. Cristiano, Solid-State Electron. 49 (2005) 1168.
26. R. Wittmann, S. Uppal, A. Hossinger, J. Cervenka and Selberherr, ECS Trans. 3 (2006) 667.
27. J. Lindhard, M. Scharff, H. E. Schiott, Mat. Fys. Medd. Dan. Vid. Selsk. 33 (1963) 1.
28. N. A. Cherkashin, A. Claverie, C. Bonafos, V. V. Chaldyshev, N. A. Bert, V. V. Preobrazhenskii, M. A. Putyato, B. R. Semyagin, P. Werner, J. Appl. Phys. 023520 (2007) 102.
29. C. J. Ortiz, F. Cristiano, B. Colombeau, A. Claverie, N. E. B. Cowern, Mater. Sci. Eng. B 114–115 (2004) 184.

© Cognizure. All rights reserved.

Cite this article as:

A. Belafhaili *et al.*: **An alternative explanation for the effect of Ge content on the density of end-of-range defects found in ion implanted relaxed SiGe alloys.** ScienceJet 2012, **1**: 14

© Cognizure. All rights reserved.

Electronic and optical properties of Cu_2XS_3 (X=Si, Ge, Sn): Prospects for photovoltaics

V. L. Shaposhnikov[a], A. V. Krivosheeva[a], V. E. Borisenko[a], J.-L. Lazzari[b,*]

[a] *Belarusian State University of Informatics and Radioelectronics, P. Browka 6, 220013 Minsk, Belarus*
[b] *Centre Interdisciplinaire de Nanoscience de Marseille, UMR 7325 CNRS – Aix-Marseille Université, Case 913, Campus de Luminy, 13288 Marseille cedex 9, France*

[*] *Author for correspondence: J.-L. Lazzari, email: lazzari@cinam.univ-mrs.fr*
Received 4 Feb 2012; Accepted 26 Mar 2012; Available Online 19 Apr 2012

Abstract

In order to find cheap and environment-friendly materials applicable in photovoltaics, we have performed a theoretical study of structural, electronic and optical properties of Cu_2XS_3 (X=Si, Ge, Sn) ternary compounds by means of DFT calculations using the Vienna *ab initio* simulation package (VASP) and full-potential linearized augmented plane wave (FLAPW) method. The modified Becke-Johnson potential has been used. The different structural phases were considered: two hexagonal, two orthorhombic and one monoclinic. The latter one was determined to be the most stable for all these compounds. Cu_2XS_3 compounds in monoclinic phase are found to be direct-gap semiconductors with the band gaps of 1.73, 0.47 and 0.09 eV in Cu_2SiS_3, Cu_2GeS_3 and Cu_2SnS_3, respectively, following the tendency of decreasing the band gap with increasing of the group-IV element. It was found that the increase of the number of group-IV element always leads to the increase of lattice constants by about 3–5% and the unit cell volume up to 10%. Prospects for photovoltaic applications of the studied materials are discussed on the basis of analysis of their absorption coefficients.

Keywords: Photovoltaics; Band structure; Absorption coefficient

1. Introduction

The world energy consumption is continuously increasing since one century nearly reaching the equivalent of 13 TW per year for fossil resources. Solar energy will remain for long the most abundant and reliable source of energy [1], and nowadays the photovoltaic conversion attracts a special attention because of the global warming problem. To be used in solar cells, it is important to find cheap and environmentally friendly materials having preferably large direct band gaps and lattice constant close to silicon or gallium arsenide substrates. One of such promising candidates for photovoltaics may be Cu_2XS_3 (X = Si, Ge, Sn) compounds, which consists of rather cheap, not hazardous or toxic, and abundant chemical elements, as compared to those used for $CuInGaSe_2$ or CdTe based thin-films solar cells. Usually, Cu_2XS_3 materials are experimentally synthesized in a form of single crystals or thin films and may have disordered and not well defined crystal structure. Several phases were found for them in these experiments: cubic, tetragonal, orthorhombic, monoclinic, and hexagonal. Numerous papers are devoted to fabrication and characterization of Cu_2XS_3 compounds; however their structural, electronic and optical properties remain contradictory. Band gap of 0.3 eV has been observed for Cu_2GeS_3 [2], direct optical gaps of 1.15 eV [3] and 1.75 eV [4] were measured in Cu_2SnS_3 thin films. Theoretical investigations are practically absent in the literature. Only recently one group estimated the band structure and optical properties of Cu_2SnS_3 [5]. In this paper, we are trying to fill this lacuna of theoretical data.

2. Computational details

According to the experimental data [2, 6], Cu_2XS_3 compounds may have the following phases: monoclinic (space group *Cc*), base-centered orthorhombic (space group *Imm*2), *C*-base-centered orthorhombic (space group $Cmc2_1$), hexagonal (space group $P6_3/mmc$), and trigonal (space group P_3). Some undistorted phases were also observed: cubic (space group *F*-43*m*) and tetragonal (space group *I*-42*m*). Unfortunately, materials in these phases contain atomic sites with fractional occupational numbers, so they cannot be calculated within the methods dealing with periodical crystal structures. Thus, they were not considered in the present paper. The structural optimization has been performed by the projector augmented wave (PAW) method [7] with Perdew-Burke-Ernzerhof (PBE) functional [8] realized in Vienna *ab initio* simulation package (VASP) [9, 10]. The energy band structure and optical properties were calculated using the full-potential linearized augmented plane wave (FLAPW) method (WIEN2K package) [11]. In order to obtain the most realistic energy values the modified Becke-Johnson potential (mBJ) [12] has been applied in the WIEN2K calculations. The latter potential has been chosen because it allows obtaining energy gaps which are in better agreement with experiments than standard PBE. For example, the calculated mBJ band gaps (E_g) of 1.19 eV and 1.3 eV for Si and GaAs are found much closer to experimental values (1.12 eV and 1.42 eV) than PBE ones of 0.6 eV and 0.35 eV. Otherwise it needs practically the same computational time as for the usual generalized gradient approximation (GGA). This differs radically from the GW approximation which also gives good numerical results but takes about 100 times more time and requires incredibly powerful computing resources for calculations of large crystals.

© Cognizure. All rights reserved.

Table 1. The equilibrium lattice constants (Å), the total energy (eV) and unit cell volume (Å^3) per formula unit (f.u.) as well as theoretical band gap values (E_g) estimated within PBE and mBJ for Cu_2XS_3 compounds.

Phase	*a*	*b*	*c*	β	E_{tot}/f.u.	*V*/f.u.	E_g^{PBE}, eV	E_g^{mBJ}, eV
				Cu_2SiS_3				
$P6_3/mmc$	4.041	4.041	15.966	90	-48.942	225.817	–	–
*Imm*2	11.012	3.678	5.309	90	-55.904	214.980	0.16	0.56
Cc	6.364	11.202	6.354	71.69	**-56.026**	215.006	1.05	1.73
$Cmc2_1$	11.011	6.412	6.095	90	-56.008	215.195	1.16	1.66
P_3	6.377	6.377	6.158	90	-54.532	216.897	–	–
				Cu_2GeS_3				
$P6_3/mmc$	4.160	4.160	15.890	90	-47.917	238.103	–	–
*Imm*2	11.241	3.813	5.321	90	-52.702	228.101	–	0.09
Cc	6.503	11.335	6.541	70.84	**-52.709**	227.740	0.01	0.47
$Cmc2_1$	11.234	6.519	6.226	90	-52.609	227.968	0.21	0.71
P_3	6.552	6.552	6.208	90	-51.669	230.800	–	–
				Cu_2SnS_3				
$P6_3/mmc$	4.386	4.386	15.725	90	-46.098	261.961	–	–
*Imm*2	11.612	3.924	5.429	90	**-51.584**	247.341	–	–
Cc	6.710	11.621	6.741	70.33	-51.579	247.490	0.04	0.09
$Cmc2_1$	11.575	6.691	6.400	90	-51.449	247.861	0.01	0.11
P_3	6.705	6.705	6.392	90	-50.724	248.868	–	–

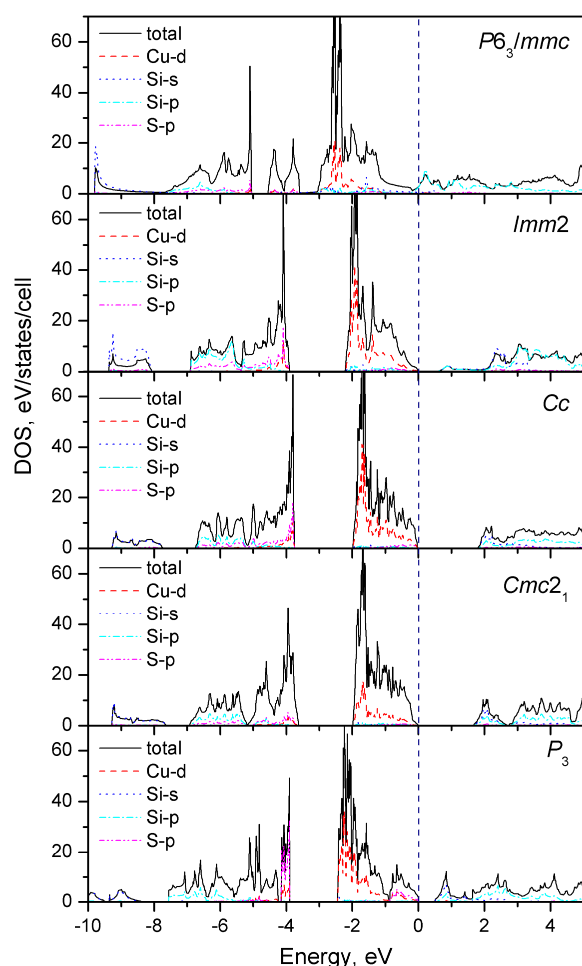

Figure 1. The total and projected DOS for different phases of Cu_2SiS_3 calculated within mBJ functional. Zero at the energy scale corresponds to the Fermi energy. To increase visibility, DOS spectra for Si-*s* and Si-*p* are multiplied by 10.

3. Results and Discussion

The analysis of the total energy per formula unit (f.u.) shows that Cu_2SiS_3 and Cu_2GeS_3 are energetically stable in the monoclinic phase while for Cu_2SnS_3 the total energy of *Imm*2 orthorhombic phase is slightly smaller than that for the monoclinic one. The hexagonal phase which was recently experimentally observed [6] is found less stable. The analysis of the structural parameters (Table 1) allows concluding, that the increase of the group IV element number in the Cu_2XS_3 family always leads to the increase of lattice constants by about 3–5% (except for *c* lattice constant in the hexagonal lattice) and the unit cell volume up to 10%. It also leads to the increase of interatomic distances except for Cu-S distances in the hexagonal lattice. The lattice constants of monoclinic Cu_2SiS_3 and Cu_2GeS_3 (6.35 - 6.54 Å) are found to differ much from ones for Si (*a*=5.43 Å) or GaAs (5.65 Å). Thus, an unstrained epitaxial growth of such materials on these substrates looks unlikely. The structural parameters obtained for Cu_2SnS_3 are in a good agreement with recent theoretical estimation [5].

The band gaps obtained by PBE and mBJ techniques are summarized in Table 1. Cu_2XS_3 compounds demonstrate semiconducting nature for monoclinic and both orthorhombic phases. Cu_2SnS_3 is practically gapless. The hexagonal and trigonal phases have metallic behavior, except for trigonal phase of Cu_2SiS_3. The band gaps follow the tendency of decreasing with increasing of the group IV element number as it was previously found for chalcopyrite semiconductors [13, 14]. Band gaps obtained with the mBJ functional are larger than that estimated with PBE one and look more trustable.

The analysis of the total and projected densities of states (DOS) for different phases of Cu_2SiS_3 (Figure 1) shows that the spectra are generally similar except for some features in the valence band of the hexagonal phase. The valence band near the Fermi level is characterized mainly by *d*-electrons of Cu for all compounds considered. The low-lying valence states are composed by *s*-electrons of Si or *p*-electrons of Ge or Sn which are hybridized with *p*-electrons of S. The conduction band near the Fermi level is mainly formed by *s*- or *p*-electrons of group IV element. The difference of DOS between Cu_2SiS_3 and two other compounds is that *s*- and *p*-states of Ge or Sn are separated by a small gap, while for Si they are mixed together.

© Cognizure. All rights reserved.

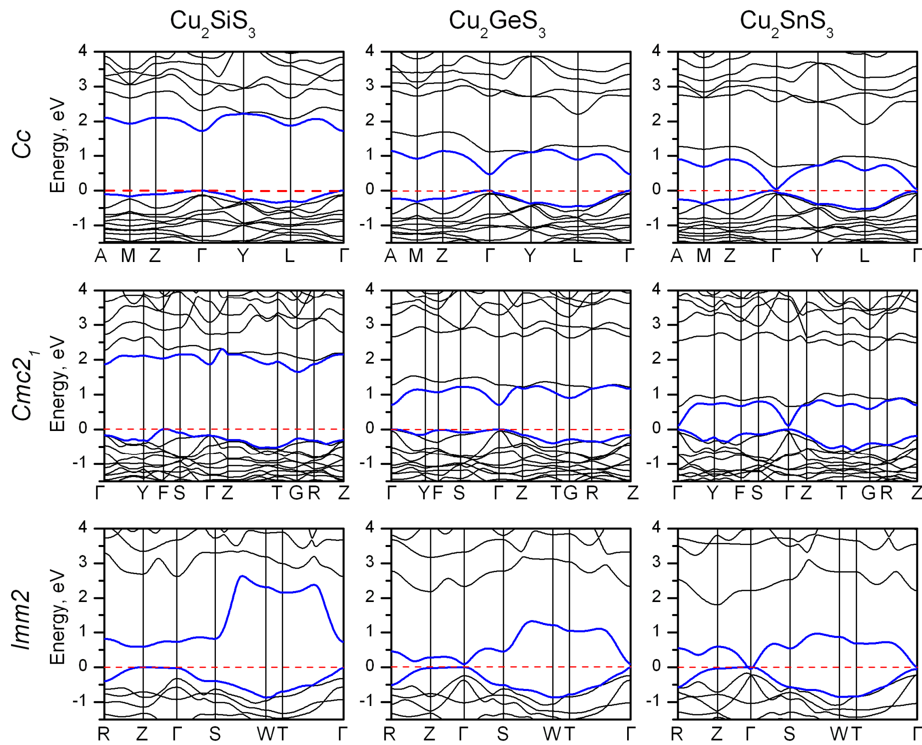

Figure 2. The band structures for monoclinic (*Cc*) and orthorhombic (*Cmc*2_1 and *Imm*2) phases of Cu_2XS_3. Zero at the energy scale corresponds to the Fermi energy.

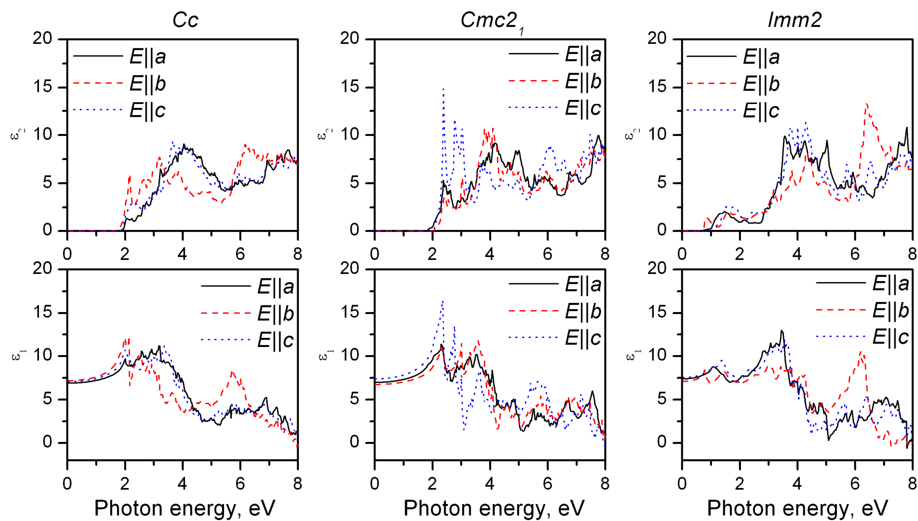

Figure 3. Imaginary (ε_2) and real (ε_1) parts of dielectric function of Cu_2SiS_3 in *Cc*, *Cmc*2_1 and *Imm*2 phases along different directions of light polarization.

The band structures of Cu_2XS_3 compounds in the monoclinic and two orthorhombic phases along the high-symmetry directions of the corresponding Brillouin zones are presented in Figure 2. All compounds in monoclinic case are characterized by a direct gap at the Γ-point. Cu_2GeS_3 and Cu_2SnS_3 in *Cmc*2_1 phase keep direct gap, while Cu_2SiS_3 has an indirect gap. In *Imm*2 phase the upper valence band is practically flat in Γ-Z direction. Our DOS and band structure calculated for monoclinic Cu_2SnS_3 look similar to those demonstrated in [5] except that the authors used hybrid non-local exchange-correlation functional (HSE) to calculate the electronic structure and optical properties. Thus, they have found the energy gap of 0.8-0.9 eV while our estimations show practically gapless case.

The imaginary part (ε_2) of the dielectric function of Cu_2SiS_3 (Figure 3) displays differences for the phases considered and strong anisotropy between light polarizations especially for *Cmc*2_1 phase. The spectra of the real part (ε_1) of the dielectric function reproduce the corresponding features of ε_2 having the value of static dielectric function $\varepsilon_1(0)$ of about 7 independently on the phase and light polarization.

© Cognizure. All rights reserved.

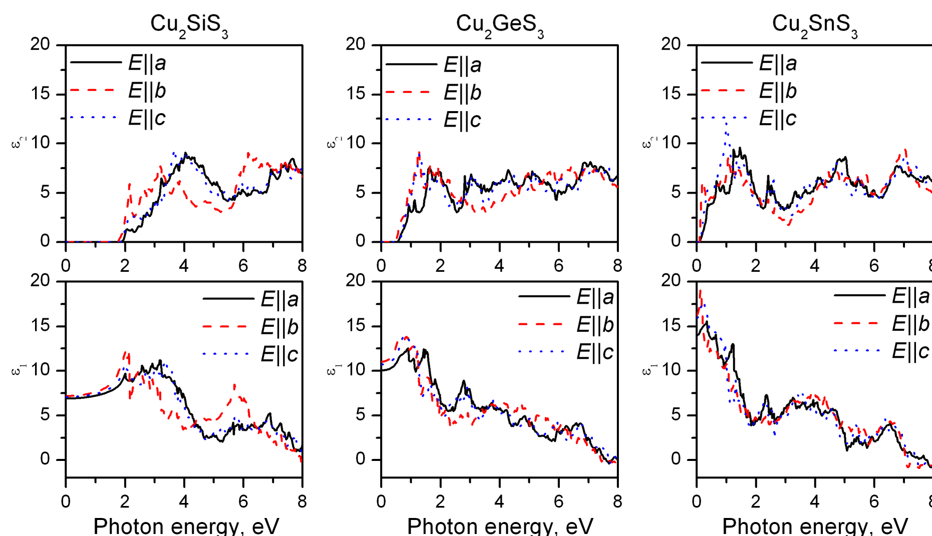

Figure 4. Imaginary (ε_2) and real (ε_1) parts of dielectric function of Cu_2SiS_3, Cu_2GeS_3 and Cu_2SnS_3 in monoclinic *Cc* phase along different directions of light polarization.

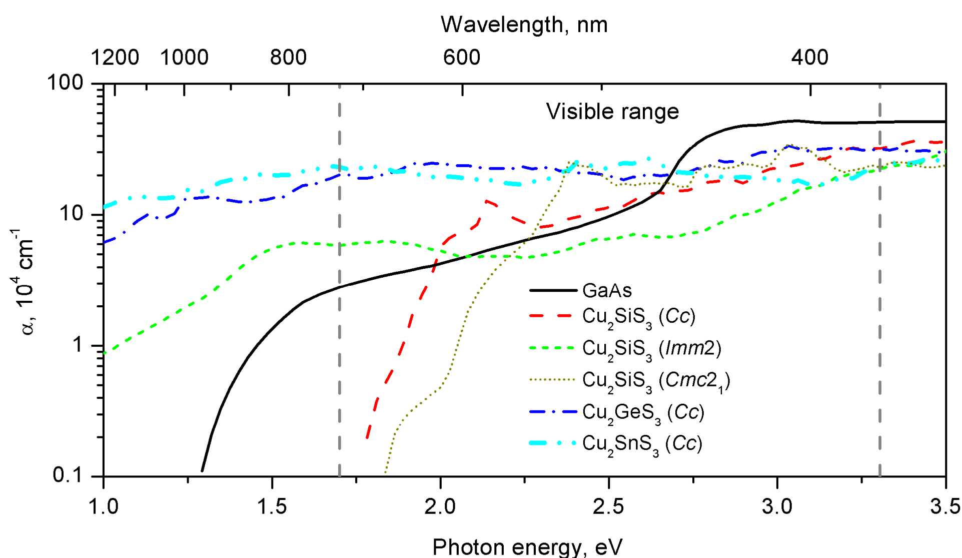

Figure 5. The averaged absorption coefficients of Cu_2XS_3 compounds.

The ε_2 and ε_1 curves of the dielectric function of Cu_2XS_3 compounds in the monoclinic *Cc* phase are presented in Figure 4. The spectra demonstrate some anisotropy between light polarizations consisting in shifting of main peaks and changing their amplitudes. All three compounds, being direct-gap semiconductors, are characterized by high dipole matrix elements ($|P|^2$) of the fist direct transition at the Γ-point. These values are about 0.03-0.05 for $E||b$ light polarization being somewhat smaller than that for GaAs (0.1). Thus, the first direct transition at the Γ-point is allowed and has large oscillator strength. This explains the sharp start of ε_2 especially for $E||b$. The static dielectric function $\varepsilon_1(0)$ increases with the increase of the group IV element number.

The optical absorption coefficient averaged over light polarizations is shown in Figure 5. It is obvious that Cu_2XS_3 compounds have absorption coefficients larger than 10^5 cm^{-1} above their respective band gaps. They are comparable to that of GaAs or Si, which are widely used for solar cells. Thus, Cu_2SiS_3 and $Cu_2Si_{1-x}Ge_xS_3$ solid solutions look promising for solar cell applications.

4. Conclusions

Crystal structure, energy band spectra and optical properties of Cu_2XS_3 (X= Si, Ge, Sn) ternary compounds in different phases were estimated by means of *ab initio* theoretical calculations. As a result, the monoclinic phase of these compounds was found to be the most stable. The change of the group IV element in the row Si–Ge–Sn increases interatomic distances (except for Cu-S distances in hexagonal lattice), as a result lattice constants are increasing by about 3–5% and the unit cell volume up to 10%. Cu_2XS_3 compounds were established to be semiconductors in monoclinic and both orthorhombic phases while Cu_2SnS_3 was found to be practically gapless. The hexagonal and trigonal phases demonstrate metallic behavior, except for the trigonal phase of Cu_2SiS_3. All compounds in the monoclinic phase have been

© Cognizure. All rights reserved.

found to be direct-gap semiconductors with the gaps of 1.73, 0.47 and 0.09 eV for Cu_2SiS_3, Cu_2GeS_3 and Cu_2SnS_3, respectively. The fist direct transition is allowed in dipole approximation and has sizable oscillator strength. The imaginary and real parts of the dielectric function demonstrate strong anisotropy between different light polarizations. Cu_2XS_3 compounds have absorption coefficients lager than 10^5 cm^{-1} near their absorption edges. Thus Cu_2SiS_3 and $Cu_2Si_{1-x}Ge_xS_3$ solid solutions seem to be promising materials for photovoltaic applications.

Acknowledgments

This work has been done within the program "Electronics" of the Ministry of Education of Belarus and BRFFR-CNRS grant № F11F-011.

References

1. A. Luque, J. Appl. Phys. 110 (2011) 031301.
2. O. Madelung, U. Rössler, M. Schulz (ed.), Landolt-Börnstein New Series, Group III: Condensed Matter, Ternary Compounds, Organic Semiconductors, Vol. 41E, Springer-Verlag (2000).
3. M. Bouaziz, M. Amlouk, S. Belgacem, Thin Solid Films 517 (2009) 2527.
4. A. Amlouk, K. Boubaker, M. Amlouk, Vacuum 85 (2010) 60.
5. Y.-T. Zhai, S. Chen, J-H. Yang, H.-J. Xiang, X.-G. Gong, A. Walsh, J. Kang, S.-H. Wei, Phys. Rev. B 84 (2011) 075213.
6. C. Wu, Z. Hu, C. Wang, H. Sheng, J. Yang, Y. Xie, Appl. Phys. Lett. 91 (2007) 143104.
7. G. Kresse, J. Joubert, Phys. Rev. B 59 (1999) 1758.
8. J.P. Perdew, K. Burke, M. Ernzerhof, Phys. Rev. Lett. 77 (1996) 3865.
9. G. Kresse, J. Hafner, Phys. Rev. B 49 (1994) 14251.
10. G. Kresse, J. Furthmüller, Phys. Rev. B 54 (1996) 11169.
11. P. Blaha, K. Schwarz, G.K.H. Madsen, D. Kvasnicka, J. Luitz, WIEN2k, An Augmented Plane Wave + Local Orbitals Program for Calculating Crystal Properties, Karlheinz Schwarz, Techn. Universität Wien, Austria (2001).
12. F. Tran, P. Blaha, Phys. Rev. Lett. 102 (2009) 226401.
13. A.V. Krivosheeva, V.L. Shaposhnikov, V.V. Lyskouski, V.E. Borisenko, F. Arnaud d'Avitaya, J.-L. Lazzari, Microelectron. Reliab. 46 (2006) 1747.
14. A.V. Krivosheeva, V.L. Shaposhnikov, V.E. Borisenko, F. Arnaud d'Avitaya, J.-L. Lazzari, Proc. SPIE 7377 (2008) 737705.

Cite this article as:

V. L. Shaposhnikov *et al.*: **Electronic and optical properties of Cu_2XS_3 (X=Si, Ge, Sn): Prospects for photovoltaics.**
ScienceJet 2012, **1**: 15

© Cognizure. All rights reserved.

Structure, electronic and optical properties of tin sulfide

V. L. Shaposhnikov[a], A. V. Krivosheeva[a], V. E. Borisenko[a], J.-L. Lazzari[b,*]

[a] *Belarusian State University of Informatics and Radioelectronics, P. Browka 6, 220013 Minsk, Belarus*
[b] *Centre Interdisciplinaire de Nanoscience de Marseille, UMR 7325 CNRS – Aix-Marseille Université, Case 913, Campus de Luminy, 13288 Marseille cedex 9, France*

[*]Author for correspondence: J.-L. Lazzari, email: lazzari@cinam.univ-mrs.fr
Received 4 Feb 2012; Accepted 26 Mar 2012; Available Online 19 Apr 2012

Abstract

Structural, electronic and optical properties of different phases of tin sulfide SnS_x ($1 \le x \le 2$) have been theoretically estimated by modern potential and approximation techniques (modified Becke-Johnson, GW approximation) beyond the density functional theory. All phases were found to be indirect-gap semiconductors. The room-temperature simple orthorhombic α-phase of SnS is characterized by the energy gap of about 1.2–1.6 eV, while the high-temperature C-centered orthorhombic β-SnS has a smaller gap of about 0.6 eV. The cubic phases which were experimentally observed in thin films possess a gap of about 0.7 eV, while the largest band gap, *i.e.* 2.4-2.9 eV, was found for hexagonal phases of SnS_2. The averaged absorption coefficients (> 10^5 cm^{-1} in the visible spectrum) of cubic or orthorhombic phases of SnS were found to be around one order of magnitude with that of GaAs. This shows α-phase of SnS to be promising for photovoltaic applications.

Keywords: Tin sulfide; Band structure; Photovoltaics; Absorption coefficient

1. Introduction

The solar cell generates electric power when illuminated by sun or artificial light. Thus photovoltaic technology looks more elegant and benign than conventional methods of electricity generation. The most striking advantage is that sun light will remain the world's major renewable energy resource [1,2]. Nowadays solar energy conversion represents one of the most dynamically growing branches of the high-technological industry. A lot of materials are used for production of thin-films based solar cells, such as $Cu(In,Ga)Se_2$, CdTe, GaAs/GaInP/Ge and others. The use of the rare and toxic elements in these materials increases the cost of the final product and leads to environmental contamination. Tin sulfide, SnS, being one of semiconducting materials in the $A^{IV}B^{VI}$ family, does not have these disadvantages. It consists of elements (Sn and S), which are abundant in nature. Moreover, SnS growing process is non-polluting. Thus, SnS is being intensively experimentally studied for use in solar cells built from low-cost non-toxic materials. Strangely, only one theoretical simulation of orthorhombic SnS has been published. It was reported that both room and high-temperature phases were indirect-gap semiconductors [3]. Experimentally it was observed that SnS might exhibit p- or n-type conductivity depending on the concentration of components and preparation conditions. Different energy gaps in the range from 1.0 to 2.3 eV have been obtained [4-8]. Thin films of SnS may be synthesized in different phases: cubic, orthorhombic, hexagonal [4-8]. Moreover, a few phases were reported to be used in n–p homo- and heterojunctions [8]. However, until now, some discrepancies exist in structural, electronic and optical properties of this semiconductor. Hence, we have performed their theoretical simulation which would give experimentalists more information about different phases of SnS.

2. Methods of Calculation

We considered several phases of SnS_x: cubic (space group *F*-43*m*), found in thin films; orthorhombic low-temperature α-SnS (formed at T < 880 K) (space group *Pbnm*); high-temperature β-SnS (formed at T > 880 K) (space group *Cmcm*); orthorhombic Sn_2S_3 (space group *Pnma*); hexagonal (space group $P6_3/mmc$) SnS_2 [4]. The full structural optimization has been performed by the projector augmented wave (PAW) method [9] with generalized gradient approximation (GGA) of Perdew-Burke-Ernzerhof (PBE) [10] realized in VASP computer code [11,12]. The band structures and optical spectra were calculated using the FLAPW method (WIEN2K computer code) [13]. In order to obtain realistic energy gaps the modified Becke-Johnson (mBJ) potential [14] has been applied to the WIEN2K calculations. The latter potential allows improving the accuracy of the energy gap values to bring them closer to experiments. For example, the band gaps calculated using mBJ potentials for Si and GaAs (1.19 and 1.3 eV, respectively) are much closer to experimental values (1.12 and 1.42 eV at 300 K, 1.15 and 1.52 eV if extrapolate to 0 K) than PBE ones (0.6 and 0.35 eV). As the crystal structures of most of tin sulfide phases contains small number of atoms, the GW_0 approximation realized in VASP package has been also applied.

3. Results and Discussion

The analysis of the total energy per formula unit (Table 1) shows that, among monosulfide phases, α-SnS is the most energetically favorable while the cubic phase is the least.

© Cognizure. All rights reserved.

Table 1. The equilibrium lattice constants (Å), the total energy (eV) and unit cell volume ($Å^3$) per formula unit (f.u.) for SnS_x compounds.

Phase	Theory					Experiment			Ref.
	a	*b*	*c*	E_{tot}/f.u.	*V*/f.u.	*a*	*b*	*c*	
Cubic SnS	6.513	–	–	-33.401	276.283	5.850	–	–	[15]
α-SnS	11.416	4.026	4.413	-35.672	202.808	11.200	3.990	4.340	[16, 17]
β-SnS	4.109	11.765	4.110	-35.555	198.675	4.148	11.480	4.177	[18]
SnS_2 $P6_3/mmc$	3.700	–	13.833	-13.305	82.015	3.647	–	11.811	[19]
Sn_2S_3 *Pnma*	9.236	3.804	14.305	-88.779	502.557	8.869	3.748	14.021	[20]

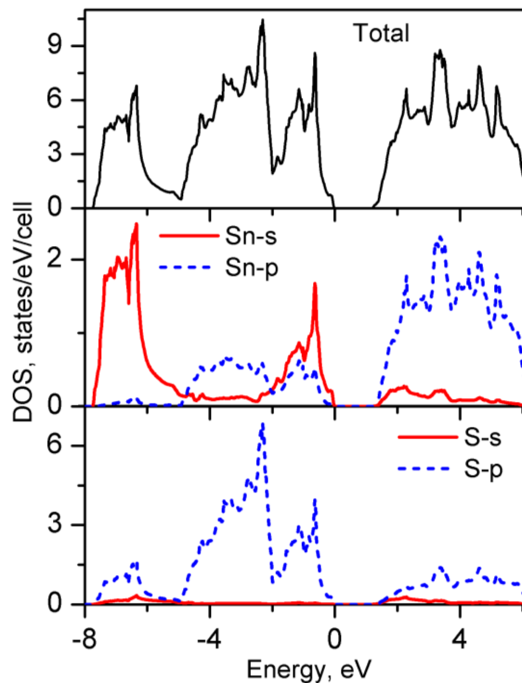

Figure 1. The total and projected DOS of α-SnS calculated by mBJ functional. Zero at the energy scale corresponds to the Fermi energy.

From the information about structural parameters one can conclude that β-SnS phase has the smallest unit cell volume while the cubic SnS has the largest one. Cubic SnS phase also shows maximum Sn-S interatomic distances while for SnS_2 and Sn_2S_3 this value is minimal.

The total and projected densities of states (DOS) of α-SnS are presented in Figure 1. The valence band near the Fermi level (-2...0 eV) is characterized mainly by 3*p*-electrons of sulfur which are hybridized with 5*s*- and 5*p*-electrons of Sn. The second wide area (-5...-2 eV) consists of S-3*p* and Sn-5*p*. The low-lying valence states (-8...-5 eV) are composed mainly by 5*s*-electrons of Sn with small admixture of S-3*p*. The conduction bands near the Fermi level are defined mainly by 5*p*-electrons of Sn.

The energy spectra of SnS_x compounds along the high-symmetry directions of the corresponding Brillouin zones calculated by mBJ functional are presented in Figure 2, while the band gap values obtained by PBE, mBJ and GW_0 techniques in comparison with experimental data are gathered in Table 2 [5-7, 20-25]. All phases of tin sulfide appeared to be indirect-gap semiconductors. The distinctive feature of electronic structure is that the valence band minimum is not located at the Γ point as it usually happens in semiconductors

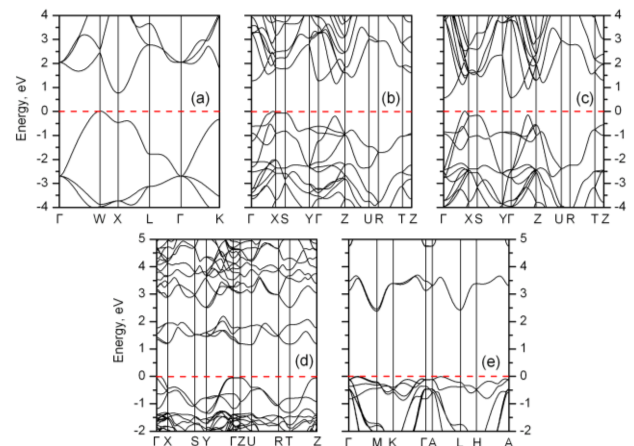

Figure 2. The band structures of cubic SnS (a), α-SnS (b), β-SnS (c), Sn_2S_3 (d) and SnS_2 (e) calculated by mBJ functional. Zero at the energy scale corresponds to the Fermi energy.

(like Si or GaAs). This can be explained by rather complex crystal structures with non-ideal atomic positions.

The band spectrum of cubic SnS has well-pronounced indirect gap where the valence band maximum (VBM) is located at the W point while the conduction band minimum (CBM) is located at the X point of face-centered Brillouin zone. For comparison, band spectra for α- and β-SnS phases were plotted for the same high-symmetry directions of the simple orthorhombic Brillouin zone. Resulting band structures have much in common. This can be explained by the fact that the crystal structure of α-SnS is a distorted β-SnS with shifted atomic positions of Sn atoms. Thus, in both phases the VBM is located not in the high-symmetry point in the Γ–X direction. There are others similar features like flat valence bands in X–S direction and local VBM in the Γ–Z direction. However, the CBM for β-SnS is located at the Γ point while for α-SnS it lies in the Γ–Z direction.

The band structure of Sn_2S_3 is characterized by VBM in Γ–X directions while upper valence bands in Γ–Z direction are practically flat and lie only 60 meV lower than VBM. There are also several points in conduction band having close minimal values: U at 1.16 eV, T at 1.17 eV and X at 1.2 eV. Moreover, these few bands are separated from the other conduction bands by the small gap of about 0.3 eV.

Hexagonal SnS_2 has two VBMs in the Γ–M and A–L directions and two CBMs at the M (2.38 eV) and L (2.42 eV) k-points. A few localized bands consisted of S-*p* states hybridized with *s*- and *p*-Sn states are separated from the other conduction bands by a gap of 1.0 eV.

© Cognizure. All rights reserved.

Table 2. Theoretical band gap values estimated within PBE, mBJ and GW_0 techniques together with experimental data for SnS_x compounds.

Phase	Cubic SnS	α-SnS	β-SnS	SnS_2 *P6₃/mmc*	Sn_2S_3 *Pnma*
PBE	0.20	0.90	0.32	1.50	0.74
mBJ	0.76	1.20	0.57	2.38	1.16
GW_0	0.60	1.58	0.67	2.90	–
Exp.	1.1-1.8 [15, 21]	1.0-1.4 [5-7, 21]	–	1.6-2.9 [22-24]	0.85-1.16 [20, 25]

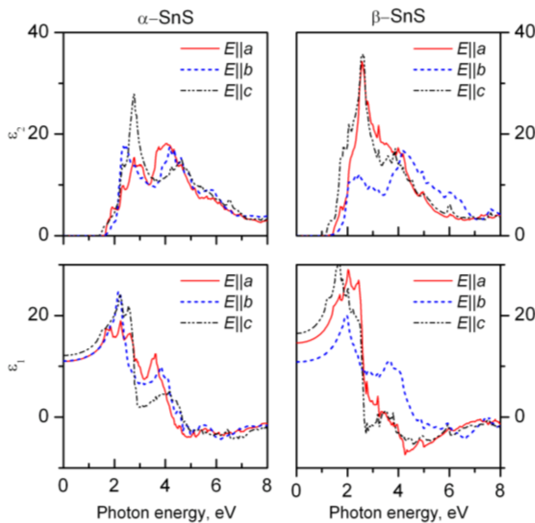

Figure 3. Imaginary (ε_2) and real (ε_1) parts of dielectric function of α-SnS and β-SnS along different directions of light polarization calculated by mBJ functional.

Our PBE band gaps and DOS of α- and β-phases of SnS are in good agreement with those obtained in another theoretical work [3]. It is well-known that band gaps calculated within local density approximation are underestimated as compared to experiment. That was observed in our results. Band gaps calculated with mBJ or GW_0 functionals are larger than those estimated by PBE and look closer to experimental data. One needs also to remember that most of optical measurements were done on SnS_x thin films of mixed compositions containing different phases, defects and inclusions, while our calculations assume ideal crystal structure and stoichiometry.

The imaginary parts (ε_2) of complex dielectric function for room- and high-temperature phases of SnS are shown in Figure 3. The optical spectra have strong anisotropy of the dielectric functions for both α- and β-phases of SnS between light polarizations along *a* (or *c*) directions and the one along *b* direction. The static dielectric function $\varepsilon_1(0)$ varies from 5 for SnS_2 to about 15 for α- and β-phases of SnS. As it was confirmed by band structure calculations, both phases of tin sulfide are indirect-gap semiconductors, thus the start of ε_2 corresponds to transitions between the more far-lying bands. In fact, for α-SnS phase the ε_2 curve (E||*c*) begins to rise at 1.4 eV, while the band gap was estimated to be 1.2 eV. For β-SnS phase the ε_2 curve (E||*c*) starts at 1.15 eV, while the band gap in this phase is 0.57 eV only. Moreover, looking at the band structures of all SnS_x phases considered, it is hard to distinguish the locations of the direct gap.

In order to be used in solar cells any material should have not only the energy gap of about 1.5 eV but also a high

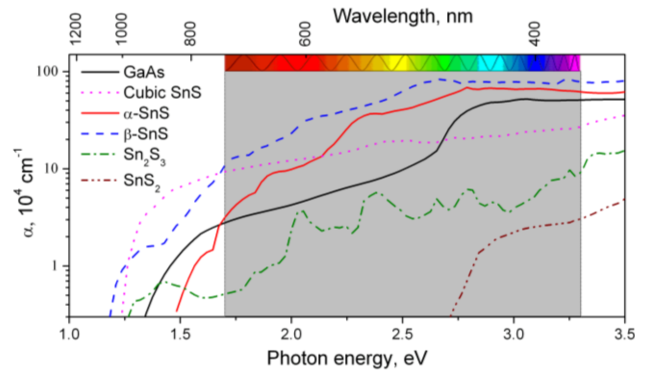

Figure 4. The averaged absorption coefficients of tin sulfide as compared with that of GaAs.

absorption coefficient ($>10^4$ cm^{-1}). Thus, we have estimated this parameter as well and plotted it in Figure 4. In spite of the indirect nature of the band gap, the averaged absorption coefficients of cubic or orthorhombic phases of SnS were found to be one order of magnitude as compared to that of GaAs, which is widely used for photovoltaics. The absorption coefficient is greater than 10^5 cm^{-1} in the visible spectrum range. In contrary, SnS_2 has a too large band gap and together with Sn_2S_3 can absorb a narrow part of the visible spectrum. Thus, one can conclude that thin films of tin sulfide may be suitable for efficient solar cells.

4. Conclusions

Theoretically estimated electronic properties of different SnS_x ($1 \le x \le 2$) phases show them to be indirect-gap semiconductors. The room-temperature simple orthorhombic α-phase of SnS is characterized by a gap of about 1.2–1.6 eV, while the high-temperature C-centered orthorhombic β-SnS has a smaller gap of about 0.6 eV. The cubic phases which were experimentally observed in thin films possess the gap of about 0.7 eV, while the largest band gap of 2.4-2.9 eV was found for hexagonal SnS_2. The optical properties analysis shows a strong anisotropy of the dielectric functions for both α- and β-phases of SnS between light polarizations along *a* (or *c*) directions and the one along *b* direction. The averaged absorption coefficients (greater than 10^5 cm^{-1} in the visible spectrum range) of cubic or orthorhombic phases of SnS were found to be one order of magnitude with that of GaAs. In spite of indirect nature of the band gap, SnS compounds are concluded to be suitable for photovoltaic applications, in particular taking into account the fact that they consist of non-rare, non-toxic and rather cheap elements and may be easily fabricated.

© Cognizure. All rights reserved.

Acknowledgments

This work was financially supported by Belarusian Republican Foundation for Fundamental Research within BRFFR-CNRS grant № F11F-011 and by programs "Functional Materials" and "Electronics" of the Ministry of Education of Belarus.

References

1. A. Luque, J. Appl. Phys. 110 (2011) 031301.
2. V. Petrova-Koch, R. Hezel, A. Goetzberger, High-Efficient Low-Cost Photovoltaics: Recent Developments, Springer-Verlag (2008).
3. A.R.H.F. Ettema, R.A. de Groot, C. Haas, T.S. Turner, Phys. Rev. B 46 (1992) 7363.
4. O. Madelung, U. Rössler, M. Schulz, (ed.), Landolt-Börnstein New Series, Group III: Condensed Matter, Ternary Compounds, Organic Semiconductors, Springer-Verlag, vol. 41E (2000).
5. M.M. El-Nahass, H.M. Zeyada, M.S. Aziz, N.A. El-Ghamaz, Opt. Mater. 20 (2002) 159.
6. F. Jiang, H. Shen, C. Gao, B. Liu, L. Lin, Z. Shen, Appl. Surf. Sci. 257 (2011) 4901.
7. Sh. Cheng, G. Conibeer, Thin Solid Films 520 (2011) 837.
8. M. Ristov, Gj. Sinadinovski, I. Grozdanov, M.M. Mitreski, Thin Solid Films 173 (1989) 53.
9. G. Kresse, J. Joubert, Phys. Rev. B 59 (1999) 1758.
10. J.P. Perdew, K. Burke, M. Ernzerhof, Phys. Rev. Lett. 77 (1996) 3865.
11. G. Kresse, J. Hafner, Phys. Rev. B 49 (1994) 14251.
12. G. Kresse, J. Furthmüller, Phys. Rev. B 54 (1996) 11169.
13. P. Blaha, K. Schwarz, G.K.H. Madsen, D. Kvasnicka, J. Luitz, WIEN2k, An Augmented Plane Wave + Local Orbitals Program for Calculating Crystal Properties, Karlheinz Schwarz, Techn. Universität Wien, Austria (2001).
14. F. Tran, P. Blaha, Phys. Rev. Lett. 102 (2009) 226401.
15. D. Avellaneda, M.T.S. Nair, P.K. Nair, J. Electrochem. Soc. 155 (2008) D517.
16. R.W.G. Wyckoff, Crystal Structures (2nd edn), Wiley & Sons, Vol. 1 (1963).
17. R.C. Sharma, Y.A. Chang, Bull. Alloy Phase Diagrams 7 (1986) 269.
18. H.G. von Schnering, H. Wiedemeier, Z. Kristallogr. 156 (1981) 143.
19. B. Palosz, E. Salje, J. Appl. Cryst. 22 (1989) 622.
20. M. Cruz, J. Morales, J.P. Espinos, J. Sanz, J. Solid State Chem. 175 (2003) 359.
21. Ch. Gao, H. Shen, L. Sun, Appl. Surf. Sci. 257 (2011) 6750.
22. C. Khèlia, K. Boubaker, T. Ben Nasrallah, M. Amlouk, S. Belgacem, J. Alloys Compd. 477 (2009) 461.
23. N.G. Deshpande, A.A. Sagade, Y.G. Gudage, C.D. Lokhande, R. Sharma, J. Alloys Compd. 436 (2007) 421.
24. G. Domingo, R.S. Itoga, C.R. Kannewurf, Phys. Rev. 143 (1966) 536.
25. S. Lopez, S. Granados, A. Ortiz, Semicond. Sci. Technol. 11 (1996) 433.

Cite this article as:

V. L. Shaposhnikov *et al.*: **Structure, electronic and optical properties of tin sulfide.** ScienceJet 2012, **1**: 16

© Cognizure. All rights reserved.

Influence of the CF_4+O_2 plasma treatment of ZnO:Al on a-Si p-i-n solar cell performance

J. D. Santos[a,*], S. Fernández[a], A. Casado[a], J. L. Baldonedo[b], O. De Abril[c], C. Maffiotte[a], J. Cárabe[a], J. J. Gandía[a]

[a] *CIEMAT, Av. Complutense, 22, 28040, Madrid, Spain*
[b] *Centro de Microscopía Electrónica "Luis Bru". Ciudad Universitaria, 28040 Madrid, Spain*
[c] *ICMM-CSIC, Cantoblanco. 28049 Madrid, Spain*

[*] *Authors for correspondence: J. D. Santos, email: josedomingo.santos@ciemat.es*
Received 4 Feb 2012; Accepted 21 May 2012; Available Online 21 May 2012

Abstract

The transparent conductive oxide (TCO) is commonly used as front electrode in p-i-n solar cells. Its surface state has an important impact on the amorphous silicon (a-Si:H) nucleation, and hence on the device efficiency. Specifically, the TCO surface morphology should be controlled to assure the growth of a dense enough a-Si:H structure. Otherwise, ohmic current paths might develop in the solar cell, causing an electrical loss increase. The application of a plasma treatment allows the elimination of possible imperfections on the TCO surface. Thus, the final device shows a higher shunt resistance, and consequently a better performance. This work addresses the problem of the shunting behaviour observed in our a-Si:H p-i-n devices deposited onto sputtered ZnO:Al (AZO). As a solution, a CF_4+O_2 plasma treatment was used to smoothen the AZO surface. For exposure times around five minutes, the elimination of surface defects led to a more compact a-Si:H structure, and a notable fill factor improvement was observed. Nevertheless, for long enough exposures, this dry-etching process caused an important deterioration of the AZO electrical characteristics. The effect of the CF_4+O_2 plasma treatment on the AZO bulk and surface properties was also studied.

Keywords: a-Si:H; AZO; Solar cell; CF_4+O_2; Dry-etching; Shunt resistance

1. Introduction

The transparent conductive oxide (TCO) is usually used as the front electrode in amorphous silicon (a-Si:H) solar cells. This layer should present a high optical transmittance in order to minimize optical losses and ensure that photons are mostly captured in the device absorber. At the same time, a high electrical conductivity of TCO is necessary to correctly collect the photogenerated current in the solar cell [1]. However, beyond the TCO bulk properties, its surface properties (morphology, chemical composition, etc.) also have a huge impact on the device performance [2,3].

Specifically, the TCO surface morphology directly influences the a-Si:H nucleation process. Too abrupt a TCO texture, or very step local trenches and extremely sharp peaks onto relatively flat surfaces, can cause shadowing effects during silicon growth, which lead to a lower density p-i-n structure [4-7]. In this case, the a-Si:H usually presents void-rich regions that, after the back contact deposition, become ohmic current paths through the device. As a consequence, the electrical characteristic of the final solar cell exhibits a poor fill factor and efficiency [8,9].

One of the simplest solutions to this inconvenience is based on the use of a plasma treatment that modifies the TCO surface morphology [6,10]. This kind of dry-etching, which is easily performed in a PECVD reactor, can eliminate the TCO surface imperfections, and hence favour the growth of a p-i-n structure with a greater compactness. Nevertheless, the plasma treatment could additionally change the TCO bulk properties. In this sense, it is important to emphasize that a dry-etching process will only be useful if TCO optoelectronic characteristics are not deteriorated.

The present work addresses the problem of the low shunt resistance observed in our p-i-n solar cells deposited onto sputtered ZnO:Al (AZO). Assuming that local defects on AZO surface cause less dense regions in the a-Si:H structure [6,7], a CF_4+O_2 plasma treatment is proposed as a solution. The first part of this research focuses on the dry-etching effect on the AZO bulk and surface properties. Based on these results, an upper limit for the plasma exposure time is obtained, which maximizes the sand down process of the surface, keeping the AZO optoelectronic characteristics. In the second part, the influence of this plasma treatment on the illumination and darkness J-V curve of the device is studied in detail. The improvement observed in the solar cell characteristic parameters is then correlated with long-term structural stability of the deposited a-Si:H.

2. Experimental Details

2.1. Substrate preparation and characterisation

ZnO:Al (AZO) films with thickness of around 400 nm were deposited at 250ºC by RF magnetron sputtering onto Corning glass (details about AZO properties and preparation conditions have previously been described [11]). In order to avoid the shunting behaviour of the solar cells fabricated onto the as-deposited AZO, some of these substrates were exposed to a dry-etching process performed in a plasma enhanced chemical vapour deposition (PECVD) reactor at 13.56 MHz. Plasma conditions corresponded to a temperature of 25 ºC, RF power of 75 W, gas pressure of 200 mTorr and gas flow of 10 sccm. The exposure time, $t_{ETCHING}$, was varied from 0 to 16 min in order to analyse its effect on the AZO bulk properties.

© Cognizure. All rights reserved.

Particularly, the sheet resistance (R_{SHEET}) was determined by the four-point-probe method, while the optical transmittance was obtained by using a PerkinElmer Lamba 1050 spectrophotometer. Thus, the $t_{ETCHING}$ dependence of the AZO bulk characteristics could be studied. The surface morphology variations were observed by using an AFM model Veeco Nanoscope IIIa in the contact mode. Finally, possible changes in chemical composition of the treated surface were analysed by means of a Perkin-Elmer PHI 5400 XPS spectrometer equipped with a Mg Kα excitation source (hν = 1253.6 eV). These last results were combined with ellipsometry measurements in the range 1.5-6.5 eV by using a phase-modulated ellipsometer UVISEL-Horiba Jobin Yvon.

Additionally to the mentioned substrates, a thin AZO layer (less than 100 nm thick) was prepared onto commercial Asahi-U-type glass/SnO_2:F. In this last case, the thin AZO coating reproduced the Asahi-U texture, which is specially optimized for a-Si:H solar cell development [12]. As will be shown, devices deposited onto this AZO/Asahi-U did not present signals of shunting behaviour that allowed the corroboration of the initial hypothesis about the effect of surface local defects for much thicker AZO-layers.

2.2. Solar-cell preparation and characterisation

Amorphous-silicon p-i-n devices were prepared at 250ºC onto said substrates (as-deposited AZO, plasma treated AZO, AZO-coated Asahi-U). To do this, a PECVD multi-chamber reactor operating at 13.56-MHz radio frequency was used. The structure of the deposited a-Si:H corresponded to a 7.5 nm p-type layer, a 5 nm carbon graded buffer layer, a 400 nm intrinsic layer and a 30 nm n-type layer.

Solar cells with a big area (of the order of 1 cm^2) were obtained by evaporating aluminium back contacts in each case. The density of current vs. voltage (*J-V*) characteristics of the resulting devices were measured under 100 mW/cm^2 AM 1.5G illumination conditions and in darkness at 25ºC. In this last case, experimental J-V curves were fitted to the one exponential model by using an in-house developed software [13]. The minimisation of the area between the experimental and theoretical curve, normalised to the area under the experimental curve, has been the fitting criterion of the algorithm [14]. Thus, the dark diode saturation current (J_0), ideality factor (n) and shunt resistance (R_{SH}) were calculated. The substrate dependence of solar cell parameters under light and dark conditions allowed the determination of the quality of the a-Si:H structure growth onto each substrate, and hence the effectiveness of the CF_4+O_2 plasma treatment.

These results were additionally complemented with information about the compactness of the a-Si:H deposit and its structural stability to long term. To do this, the surface of the p-i-n structure, grown onto the as-deposited and plasma treated AZO, was explored to find signals of the existence of lower density regions. The previously mentioned AFM and an optical microscope Nikon Eclipse ME600 were used for this purpose.

Finally, cross-sectional samples were prepared from solar cells fabricated onto as-deposited AZO. TEM analysis of these samples was carried out in order to obtain evidence of the development of ohmic current paths through the device. A JEOL model JEM2100 transmission electron microscope with 200 kV acceleration voltage was used.

3. Results and Discussion

3.1. Effect of the CF_4+O_2 plasma treatment on the AZO/Corning substrate

Influence on the AZO surface morphology

The AFM images of the as-deposited AZO revealed a “virtually flat” surface (see Figure 1). The obtained roughness root mean square (RMS) was very low, around 6.4 nm. Nevertheless, previous studies have found that local surface defects, such as sharp peaks, could be distributed in larger areas than those typically scanned with an AFM microscope [6]. As a consequence, a simple exploration could hardly give an evidence of these surface irregularities, which later caused the shunting behaviour of the solar cell (see section 3.2).

After the CF_4+O_2 plasma treatment, the AZO surface showed essentially the same aspect, though a slight roughness variation was detected. Specifically, the RMS was reduced to 5.7 nm for a $t_{ETCHING}$=5 minutes. However, since dry-etching processes take place essentially in a vertical direction, it was expected that potential surface protuberances would be etched with more intensity. This hypothesis was subsequently corroborated by means of the comparison of the JV curves obtained with both substrates (see section 3.2).

Referring to the surface of AZO-coated Asahi-U, AFM showed a morphology similar to the native texture of the commercial SnO_2:F (see Figure 1) (details about the characteristics of similar AZO-coatings have previously been described [3]). In this case, the obtained RMS was around 40 nm. Despite this, the AZO-coating was thin enough to assume that its surface defects should not influence the a-Si:H nucleation.

Influence on the AZO bulk properties

The dry-etching had to sand down those imperfections on the AZO surface that could lead to a lower density in the p-i-n structure. Nevertheless, during this process, some plasma atoms could be incorporated into the AZO structure, modifying its optoelectronic properties. In order to determine if the CF_4+O_2 plasma affected the AZO bulk characteristics, the evolution of the sheet resistance (R_{SHEET}) and the average

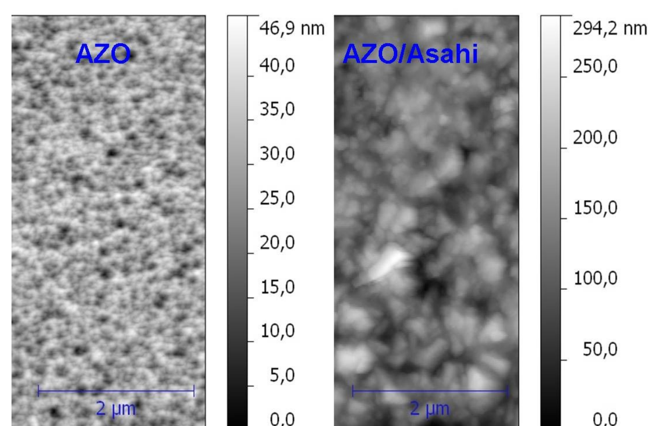

Figure 1. AFM image obtained from the as-deposited AZO/Corning substrate. The surface was virtually flat. The same aspect was obtained after the CF_4+O_2 plasma treatment. Referring to the surface of the AZO-coated Asahi-U, the AFM showed a pyramidal morphology similar to the native texture of the commercial SnO_2:F.

© Cognizure. All rights reserved.

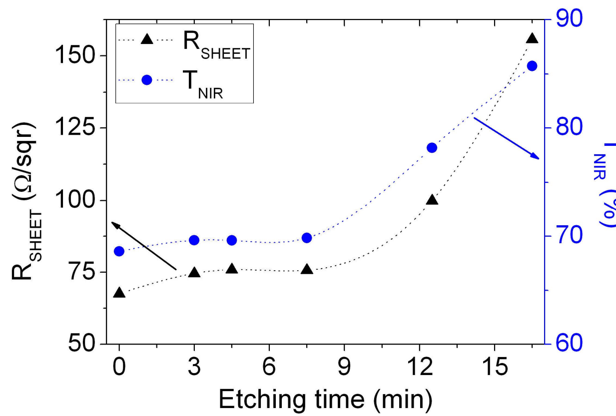

Figure 2. Etching time dependence of the AZO bulk properties. For $t_{ETCHING}$>10 min, the plasma treatment clearly deteriorated R_{SHEET}, while causing an important increase of the NIR optical transmittance. This phenomenon suggested a decrease of the free electron concentration in the AZO layer.

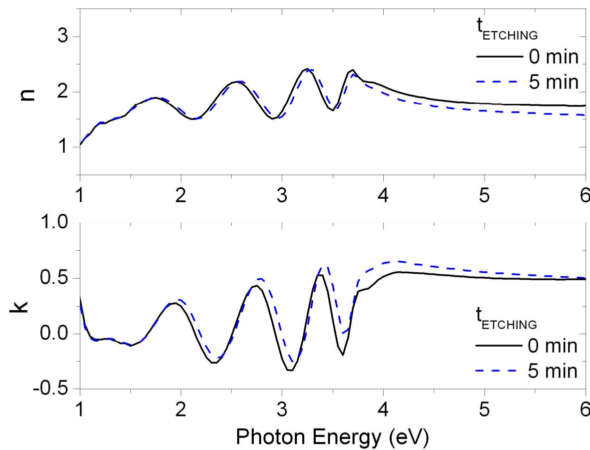

Figure 3. Real and imaginary parts of the refraction index for the as-deposited and plasma treated AZO layer. The observed energy shift seemed to be related to physicochemical changes on the AZO surface.

NIR transmittance (wavelengths from 1300 to 2500 nm) (T_{NIR}) were studied with different treatment times.

An important R_{SHEET} deterioration was observed for $t_{ETCHING}$ values greater than 10 minutes (see Figure 2). A priori, this behaviour could be caused by a notable decrease of the AZO layer thickness. However, VIS transmittance spectra did not show changes that supported this hypothesis. The explanation for this degradation of the ZnO:Al electrical properties could be extracted from the T_{NIR} analysis.

Indeed, the $t_{ETCHING}$ dependence of R_{SHEET} presented a clear correlation with the T_{NIR} evolution (see Figure 2). For long exposure times, the NIR transmittance spectra increased just for λ≥1300 nm, which corresponds to the plasma frequency for the conduction electrons in AZO [15]. Thus, a higher T_{NIR} value indicated a lower concentration of free electrons in the ZnO:Al layer. This phenomenon suggested that CF_4+O_2 plasma led to the aluminium oxidation, which would transit to an Al_2O_3 state [16], causing the R_{SHEET} deterioration. These results established a $t_{ETCHING}$ upper limit of 10 minutes.

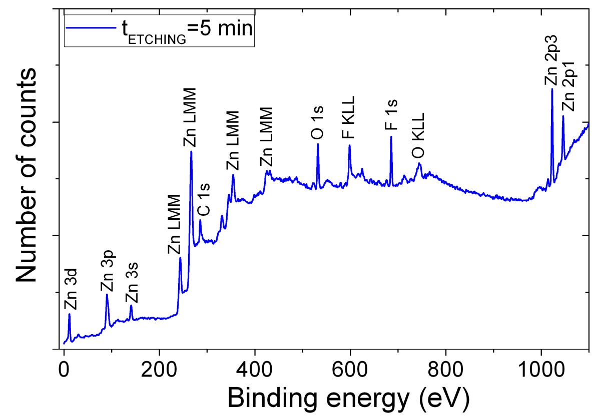

Figure 4. XPS spectra obtained for ZnO:Al after a CF_4+O_2 plasma treatment of 5 minutes. The results clearly showed the existence of fluorine in the surface chemical composition. The C 1s, F 1s, Zn $2p_{3/2}$ and O 1s peaks were used to extract the corresponding atomic concentration. Aluminium could not be detected.

Table 1. Etching time dependence of the AZO surface chemical composition obtained by means of XPS. The different X-atom/zinc concentration ratios are presented, *[X]/[Zn]*. The surface chemical composition clearly varied with the exposure-time to the CF_4+O_2 plasma. Especially interesting was the fluorine/zinc concentration ratio increase with $t_{ETCHING}$.

Etching time (min)	*[F]/[Zn]*	*[C]/[Zn]*	*[O]/[Zn]*
0	0	1.08	1.79
5	1.82	2.02	2.00
10	2.68	0.79	0.73

Influence on the AZO surface chemical composition

For exposure times lower than 10 minutes, the AZO electrical properties did not seem to be modified. However, dry-etching could additionally cause changes in the chemical composition of AZO surface. This phenomenon could have some effect on the nucleation process of a-Si:H [17]. Furthermore, it would be decisive on the AZO/p-a-Si:H interface quality, and hence on the device performance [3]. In this sense, the study of the chemical properties of the AZO surface after the CF_4+O_2 plasma became relevant.

Specifically, the AZO-film analysis by using ellipsometry confirmed this fact. Even for a short exposure, $t_{ETCHING}$=5 minutes, real and imaginary parts of the refraction index ($n^*=n+ik$) clearly varied after the dry-etching process (see Figure 3). These experimental data were fitted to a Drude model combined with a double Lorentzian oscillator [18]. The results obtained suggested that the physicochemical properties of the most external AZO layers differed from the bulk. Unfortunately, the fit was not satisfactory enough to extract additional information about this external layer.

With reference to the XPS analysis, important variations in the chemical composition were found after the CF_4+O_2 plasma treatment. Especially interesting was the existence of fluorine on the AZO surface after the dry-etching (see Figure 4). Since fluorine is an element with high electronegativity, this could somehow influence the properties of the final device. Furthermore, the fluorine/zinc concentration ratio, *[F]/[Zn]*, clearly increased with $t_{ETCHING}$ (see Table 1). A detailed analysis of the XPS spectra revealed that this fluorine could be found bonded to zinc or carbon.

© Cognizure. All rights reserved.

Table 2. Substrate dependence of the solar cell parameters extracted from the J-V curves under illumination and darkness conditions. In this last case, experimental data were fitted to the one exponential model by means of an in-house developed software. Devices deposited onto the non-treated AZO/Corning presented poor efficiency caused by their low shunt resistance (R_{SHUNT}). For the AZO/Asahi-U and the etched Corning/AZO substrates, the R_{SHUNT} notably increased due to the control of AZO surface morphology. This phenomenon led to an important open circuit voltage (V_{OC}) improvement. A better ideality factor (n) and fill factor (FF) was obtained for devices deposited onto the CF_4+O_2 treated substrate. This result suggested that the effect of the changes in chemical composition of the AZO surface should be studied in detail.

Substrate		*Illumination*				*Darkness*		
	$t_{ETCHING}$ (min)	J_{SC} (mA/cm^2)	V_{OC} (mV)	FF (%)	η (%)	R_{SHUNT} (KΩ·cm^2)	J_0 (mA·cm^2)	n
AZO/Corning	0	12.5	565	40.0	2.86	0.2	--	--
AZO/Asahi-U	0	14.4	828	47.4	5.63	1050.0	1.19×10^{-7}	1.90
AZO/Corning	5	13.1	822	57.2	6.17	291	4.5×10^{-8}	1.75

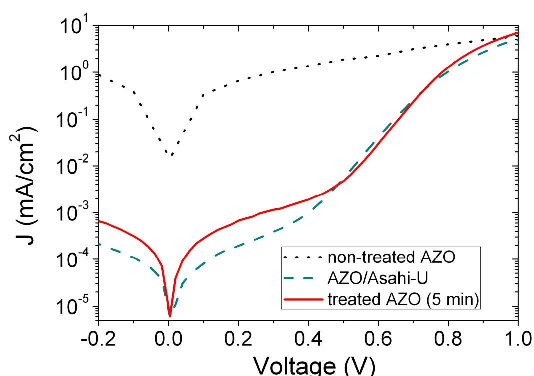

Figure 5. Comparation of the darkness J-V curves measured for devices deposited onto as-deposited AZO/Corning, AZO-coated Asahi-U, and plasma treated AZO/Corning. The surface morphology control allowed the notable improvement of the shunt resistance onto AZO/Asahi-U and etched AZO.

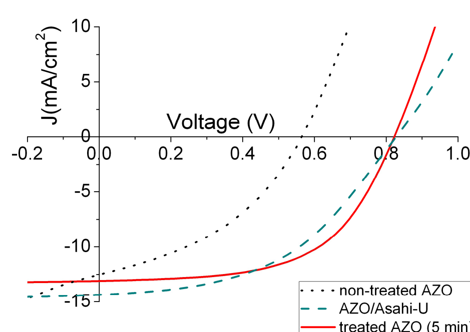

Figure 6. Comparation of the illumination J-V curves measured for devices deposited onto as-deposited AZO/Corning, AZO-coated Asahi-U, and plasma treated AZO/Corning. An important increase in the open circuit voltage was obtained attributed to the R_{SHUNT} improvement. Solar cells fabricated onto the treated AZO showed a better performance in comparison with the AZO/Asahi-U case, even though a lower short circuit current was obtained in the first case.

Precisely the carbon/zinc concentration ratio, *[C]/[Zn],* also showed an exposure time dependence. Since carbon usually behaves as a contaminant, its evolution after the dry-etching could be relevant for the device performance. In particular, for the $t_{ETCHING}$ upper limit, carbon concentration decreased, probably due to the O_2 cleaning effect. This result suggested that different plasma conditions should be found in order to reduce the carbon content for shorter exposures.

Obviously, the XPS analysis also detected oxygen in the chemical composition of the ZnO:Al surface. Curiously, the oxygen/zinc concentration ratio, *[O]/[Zn],* decreased notably just at the $t_{ETCHING}$ upper limit. In this case, it was more difficult to find a meaning for this behaviour, and hence a deeper study should be carried out.

In any case, as mentioned above, all these surface modifications could imply noticeable changes in the a-Si:H deposit and in the front junction quality of the device. A more extensive and specific study is necessary in order to determine their possible consequences. Since this is not the aim of the present work, we only emphasize the existence of this phenomenon on the AZO surface. Its implications and possible effects will be described in future works.

3.2. Effect of the CF_4+O_2 plasma treatment on the a-Si:H p-i-n solar cell

Influence on the shunt resistance and device performance

The substrate used had a very important effect on the darkness J-V curve. Most of the devices fabricated onto non-treated AZO did not show signals of rectification. Occasionally, some of these solar cells were not completely shunted, but their R_{SHUNT} values were too low, around 200 Ω·cm^2 (see Figure 5 and Table 2). In these cases, the ohmic current paths through the device notably distorted the darkness J-V characteristic, which could hardly be fitted to the one exponential model.

On the contrary, if the same p-i-n structure was grown onto the AZO-coated Asahi-U substrate, the shunt resistance of the device increased in four orders of magnitude (see Figure 5 and Table 2). This result seemed to confirm that a precise control of the surface morphology could eliminate the void-rich regions in the a-Si:H deposit, even though a greater RMS was measured for this type of substrate.

In the same way, the application of the CF_4+O_2 treatment to the AZO/Corning led to an important improvement in the device behaviour under darkness conditions. Specifically, for a $t_{ETCHING}$ =5 min, the R_{SHUNT} was around 300×10^3 Ω·cm^2. Although this value was not as good as that obtained for AZO/Asahi-U, it allowed the corroboration of the effectiveness of the dry-etching to sand down the AZO surface.

Surprisingly, the ideality factor and diode saturation current obtained onto the treated ZnO:Al improved clearly the values for solar cells deposited onto AZO/Asahi-U (see Table 2). This result suggested that, as mentioned previously, changes in the chemical composition of the AZO surface could somehow benefit the quality of the device structure.

© Cognizure. All rights reserved.

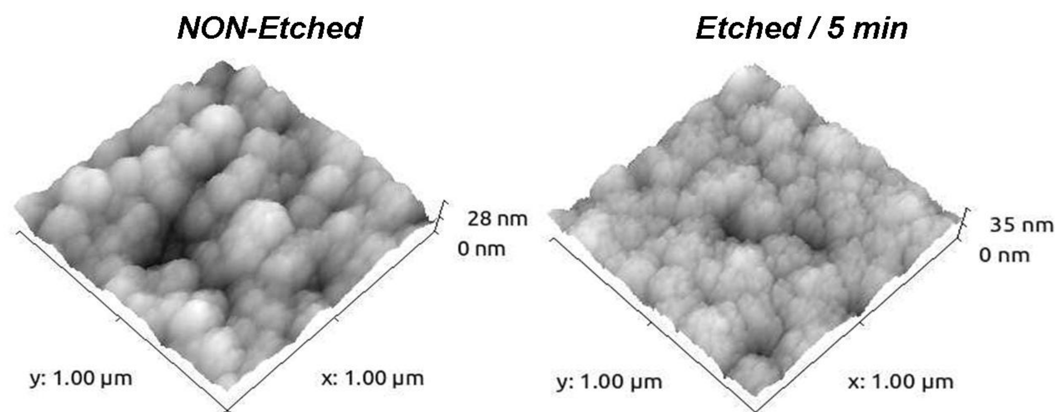

Figure 7. AFM images of the p-i-n structure surface (before back-contact evaporation) deposited onto non-treated and plasma etched AZO/Corning substrates. While a more compact structure was observed for the plasma treated case, a greater void space between the a-Si:H grains was found on the non-etched AZO.

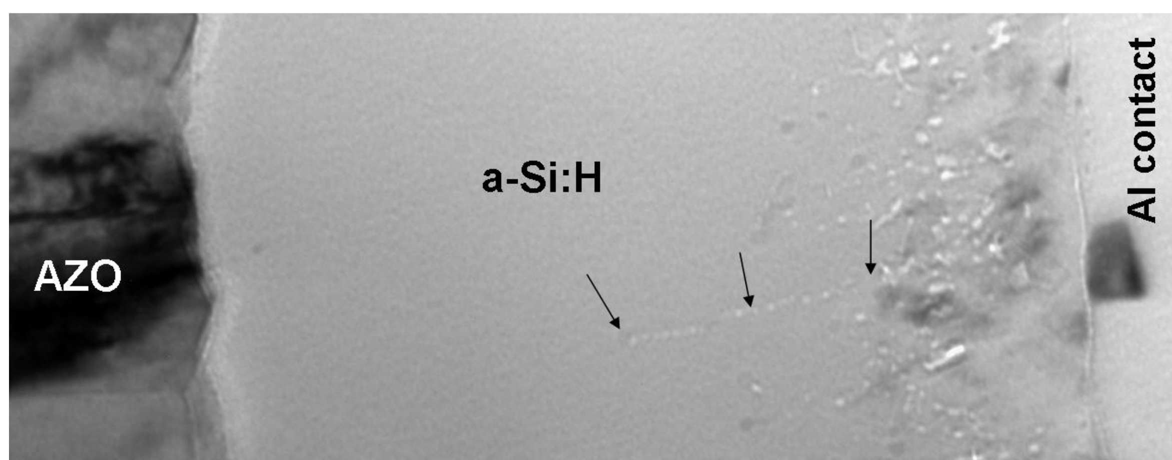

Figure 8. Cross sectional TEM image of a solar cell fabricated on non-treated AZO. It was possible to distinguish some kind of cracks where aluminium seemed to penetrate the p-i-n structure. The high number of shunting paths expected in a 1 cm^2 solar cell could explain the drastic efficiency loss.

All these observations were also reflected on the illumination J-V curves of the different solar cells. For example, the shunting behaviour observed for the non-treated AZO led to a clear deterioration of the short circuit resistance, and hence to a low open circuit voltage (V_{OC}), around 565 mV (see Figure 6 and Table 2).

The R_{SHUNT} improvement obtained for the AZO/Asahi-U and the treated AZO/Corning caused a V_{OC} increase greater than 250 mV. This result again suggested an important increase of the a-Si:H structure density, which meant a clear decrease of the electrical losses in the solar cell, and hence a better performance.

Devices fabricated on the AZO-coated Asahi-U presented the best short circuit current (J_{SC}) owing to the optimized texture of the commercial SnO_2:F, which caused a decrease of the optical losses. Despite this, solar cells deposited onto the treated AZO/Corning showed a better efficiency (η) (see Table 2). This interesting result was associated with a noticeable improvement of the fill factor (*FF*) in comparison with devices fabricated onto AZO/Asahi-U. This better *FF,* in turn, was in agreement with the improvement of the ideality factor and the dark saturation current observed in the plasma treated AZO. Again, the comparison between devices grown onto these two substrates suggested that a deeper study of the effect of the changes in the chemical composition of the AZO surface would be necessary. As mentioned before, this issue will be addressed in future works.

Influence on the a-Si:H structure compactness

The J-V curve analysis supported the initial hypothesis that an a-Si:H structure with a higher compactness could be obtained after the CF_4+O_2 plasma treatment of the AZO/Corning substrate. A closer study of this p-i-n deposit allowed the finding of additional evidence of this phenomenon.

Specifically, its surface analysis by means of AFM (before back-contact evaporation) revealed changes in how amorphous silicon nucleation took place. Effectively, while a denser structure was observed in the etched AZO, a greater void space between the a-Si:H grains was found for the non-treated case (see Figure 7).

Furthermore, this compactness variation seemed to affect the long term stability of the p-i-n structure. The exploration of the as-deposited a-Si:H surface by using an optical microscope showed a high homogeneity for both substrates. After one year, this uniformity remain unchanged in the samples deposited onto etched AZO. On the contrary, if the same p-i-n structure was fabricated on non-treated ZnO:Al, large holes developed (with diameters of around five

© Cognizure. All rights reserved.

micrometers) after a long period of time in ambient conditions. This observation could be a proof of the time evolution of the void-rich regions previously mentioned.

In fact, for the non-treated AZO case, cross-sectional TEM (X-TEM) images of finished devices revealed the existence of some kind of cracks, where aluminium seemed to penetrate the p-i-n structure (see Figure 8). These cracks could be the origin of the large holes found by using the optical microscope after one year. Considering that the X-TEM image only explored a length of the section of the device measuring hundreds of nanometers, the high number of shunting paths expected in a 1 cm^2 solar cell could explain the drastic efficiency loss observed in the as-deposited AZO.

4. Conclusions

This work addresses the problem of the low shunt resistance observed in our p-i-n solar cells fabricated on sputtered ZnO:Al (AZO). Based on the hypothesis that defects on the AZO surface favoured the growth of a more porous a-Si:H structure, a CF_4+O_2 plasma treatment was proposed as a solution. This dry-etching should sand down possible imperfections on the AZO surface, without modifying its bulk properties. For long exposure times ($t_{ETCHING}>10$ *min*), the plasma treatment deteriorated the AZO electrical characteristics. This phenomenon, associated with aluminium oxidation, imposed an upper limit for $t_{ETCHING}$. For shorter exposure times, it was possible to detect notable changes in the physicochemical properties of the AZO surface, which could somehow influence the behaviour of the final device. The effectiveness of the CF_4+O_2 plasma treatment was verified by developing solar cells on etched AZO. Even for a $t_{ETCHING}=5$ *min*, its benefits on a-Si:H nucleation process caused a shunt resistance increase of three orders of magnitude. Furthermore, all the characteristic parameters extracted from the illumination J-V curve notably improved. Specifically, the open circuit voltage increased more than 250 mV. These effects seemed to be related to a more compact p-i-n structure that could be inferred from AFM analysis and cross-sectional TEM images. Furthermore, deposition of a-Si:H structure onto treated AZO clearly improved long term stability under ambient conditions.

Acknowledgements

The authors wish to thank to M. Losurdo and G. Bruno, IMIP, Consiglio Nazionale delle Ricerche, Bari, Italy, for the support in the ellipsometry measurements. Partial financial support for this work has been provided by the Spanish Ministry of Science and Innovation under the projects AMIC (ENE2010-21384-C04-01) and INNDISOL (IPT-420000-2010-6).

References

1. R. E. I. Schropp, M. Zeman, Amorphous and Microcrystalline Silicon Solar Cells, Kluwer Academic Publishers, Dordrecht (1998).
2. J. Muller, B. Rech, J. Springer, M. Vanecek, Sol. Energy 77 (2004) 917.
3. J. D. Santos, S. Fernandez, J. Cárabe, J. J. Gandía, Effect of AZO-coating thickness on a-Si:H solar-cell performance 3AV. 2. 52, 26th EUPVSEC, Hamburg, Germany (September 2011).
4. H. Sakai, T. Yoshida, S. Fujikake, Y. Ichikawa, A. Ueda, O. Ishiwata, M. Nagano, J. Non-Cryst. Solids 115 (1989) 198.
5. M. Python, O. Madami, D. Dominé, F. Meillaud, E. Vallat-Sauvain, C. Ballif, Sol. Energy Mater. Sol. Cells 93 (2009) 1714.
6. J. J. Gandía, J. Cárabe, M. T. Gutierrez, J. Mater. Process. Technol. 143 (2003) 358.
7. J. Löffler, Transparent Conductive Oxides for Thin-Film silicon Solar Cells, PhD Thesis, Utrecht University, Netherlands (2005).
8. M. Python, E. Vallat-Sauvain, J. Bailat, D. Dominé, L. Fesquet, A. Shah, C. Ballif, J. Non-Cryst. Solids 354 (2008) 2258.
9. S. Dongaonkar, J. D. Servaites, G. M. Ford, S. Loser, J. Moore, R. M. Gelfand, H. Mohseni, H. W. Hillhouse, R. Agrawall, M. A. Ratner, T. J. Marks, M. S. Lundstrom, M. A. Alam, J. Appl. Phys. 108 (2010) 124509.
10. J. Bailat, D. Dominé, r. Schlüchter, J. Steinhauser, S. Fäy, f. Freitas, C. Bücher, L. Faitknecht, X. Niquille, T. Tcharner, A. Shah, C. Ballif, Proceedings of IEEE 4th World Conference on Photovoltaic energy conversión, Vol. 1 (2006) p. 1533.
11. S. Fernández, O. de Abril, F. B. Naranjo, J. J. Gandía, Sol. Energy Mater. Sol. Cells 95 (2011) 2281.
12. K. Sato, Y. Gotoh, Y. Hayashi, K. Adachi, H. Nichimura, Reports Res. Lab. Asahi Glass Co. Ltd., 40 (1990) 129.
13. JJ. Gandía, Células solares basadas en aleaciones de silicio amorfo y microcristalino, PhD Thesis, Universidad Complutense Madrid (2007).
14. D. S. H. Chan, J. R. Phillips, J. C. H. Phang, Solid-State Electron. 29 (1986) 329.
15. RG. Gordon, MRS Bull. 25 (2000) 52.
16. GB. Murdoch, S. Hinds, EH. Sargent, SW. Tsang, L. Mordoukhovski, ZH. Lu, Appl. Phys. Lett. 94 (2009) 213301.
17. E. Vallat-Sauvain, J. Bailat, j. Meier, X. Niquille, U. Kroll, A. Shah., Thin Solid Films 485 (2005) 77.
18. M. Losurdo, M. Giangregorio, P. Capezzuto, G. Bruno, R. De Rosa, F. Roca, C. Summonte, J. Plá, R. Rizzoli, J. Vac. Sci. Technol. A. 20 (2002) 37.

Cite this article as:

J. D. Santos *et al.*: **Influence of the CF_4+O_2 plasma treatment of ZnO:Al on a-Si p-i-n solar cell performance.**
ScienceJet 2012, **1**: 21

© Cognizure. All rights reserved.